U. PORTO

FEUP **FACULDADE DE ENGENHARIA**
UNIVERSIDADE DO PORTO

Master's Thesis in Mechanical Engineering

DEVELOPMENT OF METAL FFF FOR MECHANICAL APPLICATIONS: MECHANICAL PROPERTIES AND CORROSION CHARACTERIZATION

Author:

José Maria Bessa von Hafe Pérez

Supervisors:

Prof. Dr. Abílio de Jesus (FEUP)

Prof. Dr. Gianluca Cicala (UniCT - DICAR)

Prof. Dr. Claudio Tosto (UniCT - DICAR)

Master's Degree in Mechanical Engineering

Porto, 2023

ACKNOWLEDGEMENTS

ABSTRACT

Unlike traditional subtractive manufacturing methods, metal additive manufacturing (AM), often referred to as 3D printing, leverages computer-aided design (CAD) to systematically construct components layer by layer. These cutting-edge technologies have gained substantial traction in both academic and industrial circles. However, the conventional metal AM approaches are frequently hindered by their high costs. To address this challenge, the Metal Fused Filament Fabrication (MFFF) technique has emerged as a solution. This innovative process harnesses metal powder/polymer composite filaments, enabling the creation of metal parts by integrating the traditional Fused Filament Fabrication (FFF) methodology with subsequent debinding and sintering procedures.

This research aims to ascertain the feasibility of MFFF for mechanical applications, with a primary focus on evaluating tensile properties and corrosion resistance of MFFF samples. To achieve this, a comprehensive literature review was conducted about the intricacies of the MFFF technology, encompassing filament composition, post-printing processes, characteristics of produced parts and other relevant aspects, in order to provide context and insights. The primary objectives of this study are twofold: first, to assess the mechanical properties and corrosion resistance of 3D printed specimens fabricated using optimized printing parameters and the 17-4 PH *Ultrafuse* filament; and second, to benchmark the obtained results against existing literature, thus establishing a reference point for future investigations in this field.

The research involved a series of tests, including tensile testing, post-sintering shrinkage measurements, density assessments, thermal conductivity evaluations, and corrosion potentiodynamic polarization tests. The results revealed that the printed samples achieved 95% relative density, demonstrating the room for improvement in the methodology adopted. Notably, the orientation of the specimens during printing emerged as a critical factor influencing material performance. Samples printed in a flat position exhibited superior corrosion resistance and more isotropic shrinkage when compared to their counterparts.

However, it is noteworthy that the thermal properties of the printed material fell below the expected values for 17-4 PH. Furthermore, the mechanical properties, as determined through tensile testing, did not reach the literature benchmarks set by MFFF and other well-established metal AM technologies.

This thesis not only contributes with valuable insights into the potential of MFFF for mechanical applications but also highlights the importance of processing parameters in achieving desired material properties, also providing a foundation for future research endeavours in the landscape of this AM technique.

RESUMO

Ao contrário dos métodos tradicionais de fabrico subtrativo, o fabrico aditivo de metais (AM), frequentemente referido como impressão 3D, utiliza o design assistido por computador (CAD) para construir sistematicamente componentes, camada por camada. Estas tecnologias de ponta têm ganho reconhecimento tanto em círculos académicos como industriais. No entanto, as abordagens convencionais de AM em metais são frequentemente prejudicadas pelos seus elevados custos. Para enfrentar este desafio, a técnica de *Metal Fused Filament Fabrication* (MFFF) surgiu como uma solução. Este processo inovador utiliza filamentos compostos de metal em pó/polímero, permitindo a criação de peças de metal através da integração da metodologia tradicional de *Fused Filament Fabrication* (FFF) com procedimentos subsequentes de remoção de polímeros ligantes e sinterização.

A pesquisa tem como objetivo avaliar a viabilidade do MFFF para aplicações mecânicas, com foco principal na avaliação das suas propriedades de tração e resistência à corrosão. Para alcançar este objetivo, foi realizada uma revisão bibliográfica abrangente sobre as complexidades da tecnologia MFFF, incluindo a composição do filamento, os processos de pós-impressão, as características das peças produzidas e outros aspetos relevantes, para fornecer perceção e contexto. Os principais objetivos deste estudo avaliar as propriedades mecânicas e resistência à corrosão de amostras impressas em 3D fabricadas com parâmetros de impressão otimizados e utilizando o filamento *Ultrafuse* 17-4 PH; em segundo, comparar os resultados obtidos com a literatura existente, estabelecendo assim um ponto de referência para investigações futuras neste campo em crescimento.

A pesquisa envolveu uma série de testes, incluindo ensaios de tração, medições de contração pós-sinterização, avaliações de densidade, avaliações de condutividade térmica e testes de polarização potenciodinâmica de corrosão. Os resultados revelaram que as amostras impressas atingiram uma densidade relativa de 95%, demonstrando margem para melhorias na metodologia adotada. É de salientar que a orientação das amostras durante a impressão emergiu como um fator crítico que influencia o desempenho do material. Amostras impressas numa posição plana exibiram uma resistência superior à corrosão e uma contração mais isotrópica quando comparadas com as suas contrapartes.

No entanto, é importante notar que as propriedades térmicas do material impresso ficaram abaixo dos valores esperados para o 17-4 PH. Além disso, as propriedades mecânicas, conforme determinadas através de ensaios de tração, não atingiram os padrões da literatura estabelecidos pelo MFFF e outras tecnologias de AM em metais bem estabelecidas.

Esta tese não só contribui com informações valiosas sobre o potencial do MFFF para aplicações mecânicas, mas também destaca a importância dos parâmetros de processamento na obtenção das propriedades desejadas do material, fornecendo uma base para futuras pesquisas no âmbito desta técnica de AM.

TABLE OF CONTENTS

LIST OF FIGURES

LIST OF TABLES

NOMENCLATURE AND ABBREVIATIONS

3DEP – 3D Extrusion Printing
AM – Additive Manufacturing
BJ – Binder Jetting
BMD – Bound Metal Deposition
CAD – Computer-aided Design
CE – Counter Electrode
DDM – Direct Digital Manufacturing
DED – Directed Energy Deposition
EBM – Electron Beam Melting
FDM – Fused Deposition Modelling
FFF – Fused Filament Fabrication
J-C – Johnson-Cook
LPBF – Laser Powder Bed Fusion
MFFF – Metal Fused Filament Fabrication
MIM – Metal Injection Moulding
OCP – Open Corrosion Potential
OFS – Oversizing Factor
PBF – Powder Bed Fusion
PME – Powder Material Extrusion
POM – Polyoxymethylene
PH – Precipitation Hardening
RE – Reference Electrode
SCE – Saturated Calomel Electrode
SEM – Scanning Electron Microscopy
SLM – Selective Laser Melting
SDS – Shaping, Debinding and Sintering
SHE – Standard Hydrogen Electrode
SA – Stearic Acid
STL – Stereolithography
TGA – Thermogravimetrical Analysis
TPE – Thermoplastic Elastomer
WE – Work Electrode

$Icorr$ – Corrosion current density
$Ecorr$ – Corrosion potential
CR – Corrosion rate
ρ_a – Density of air
ρ – Density of the sample
ρ_l – Density of water
F – Faraday's constant
Lg – Green part dimension
M – Molar mass
n – number of electrons exchanged
s – Sample thickness
Sh – Shrinkage
Cp – Specific heat
Ls – Sintered part dimension
$\dot{\varepsilon}$ – Strain rate
m – Strain rate sensitivity
σ – Tensile strength
$t_{0.5}$ – Time required to achieve a temperature increase of 50%
k – Thermal conductivity
α – Thermal diffusivity
w_{air} – Weight of the sample in air
w_{liq} – Weight of the sample in water

1. INTRODUCTION

In the following sections of this introductory chapter, we will present the motivations, core objectives, research methodology, and the structural framework associated with the present thesis.

1.1. BACKGROUND AND MOTIVATION

In the past two decades, the prevalence of digital design and manufacturing tools has generated significant interest in manufacturing technologies that streamline the transition from design to the final product. Various approaches have been developed for metal-based AM, such as Powder Bed Fusion (PBF) and Direct Energy Deposition (DED). These methods involve adding layers of powder and fusing them together using high-energy laser or electron beams. Another method, known as Binder Jetting (BJ), temporarily binds powders with a polymer binder and then sinter them. Not only are these methods slower than mass manufacturing techniques, but PBF and DED methods require expensive equipment for purchase and operation. Additionally, the complicated thermal history during fabrication can lead to macroscopic defects and undesired microstructures, negatively impacting the mechanical properties of the parts. Rapid material changes are also challenging with these methods. Thus, there is a need for affordable and scalable direct manifacturing methods that can be applied to mass manufacturing, if necessary [1].

Apart from AM techniques, there's also the well-established Metal Injection Molding (MIM) process, which is also commonly employed in mass manufacturing of identical powder metallurgical parts. In this process, a metal powder is bound within a polymer matrix, resulting in a component known as feedstock. The MIM process combines the geometric flexibility of polymer injection molding with the desirable properties associated with metals, including higher mechanical, thermal, electrical conductivity and magnetic properties. However, this technology also has a high initial investment associated with it and part geometry is limited to the shape of the mold [1].

Among the processes suitable for shaping MIM-like feedstock is Metal Fused Filament Fabrication (MFFF), a recently developed additive manufacturing method that shapes 3D metal objects by extruding small strands of feedstock material. This is a version of the Fused Filament Fabrication (FFF) process, which was initially introduced and patented as Fused Deposition Modelling (FDM) by Crump in 1988, who later founded *Stratasys Corporation* in 1989 and was patented as a free-form fabrication method for three-dimensional solid polymeric objects [2].

Nowadays, FFF is the most popular process in terms of machine count worldwide. As the original FDM patent has expired, numerous low-cost and improved FDM/FFF printers have become available from various manufacturers, leading to increased attention and demand for high-quality and high-performance FDM/FFF parts. This increased attention extends to the fabrication of metal parts, which has seen a surge of investigation and development over the last few years [2, 3].

With its tremendous local control over material shape and chemistry, MFFF allows for cost and waste reduction as well as the use of a wide variety of materials. Binder-based technologies, in contrast to the more popular beam-based methods, use particle bonding

during sintering via diffusion rather than melting and solidification as the bonding process. This makes it possible to treat materials in a solid state, which is desirable for AM of materials containing volatile components and produces more isotropic microstructures. Beam-based techniques also come with a high initial investment cost, a high powder need and a risk to the operator's health from the open powder. Extrusion-based methods provide an alternate processing path that uses less expensive equipment, has the ability to preserve materials, and reduces the danger associated with handling open powder [3].

Considering the benefits that stem from employing this innovative manufacturing technique, it becomes essential to comprehensively examine the properties and distinct characteristics inherent to components produced through MFFF. Moreover, it becomes increasingly vital to scrutinize the feasibility of this emerging method when faced against well-established manufacturing processes.

1.2. OBJECTIVES

The primary objectives of this thesis were as follows:

- Tensile behaviour characterization: Investigate and characterize the tensile behaviour of 17-4 PH stainless steel produced using the MFFF method. Additionally, analyse how various strain rates influence this behaviour.
- Fracture surface analysis: Analyse the fracture surface of the tensile specimens.
- Shrinkage analysis: Examine the impact of shrinkage on MFFF samples and investigate how the orientation of the build affects this phenomenon.
- Thermal conductivity calculation: Calculate the thermal conductivity of components manufactured using the MFFF technology.
- Corrosion performance assessment: Evaluate the corrosion resistance of specimens printed in both flat and upright positions, paralleling the shrinkage assessment.
- Technology viability assessment: Assess the feasibility of the MFFF technology and the associated process parameters by comparing the obtained results with those from diverse technologies reviewed in the literature, mostly focusing on other AM processes.

1.3. RESEARCH METHODOLOGY

To fulfil the outlined objectives, the following research methodology was implemented:

- Comprehensive literature review: An extensive literature review to explore the current state of MFFF processes for manufacturing stainless steel components was conducted.
- Sample fabrication: Samples with varying geometries to serve as the initial green parts were printed.
- Post-processing: Outsourced the green samples for subsequent post-printing procedures, specifically catalytic debinding and sintering, resulting in white parts.

Dynamic tensile testing: Conducted dynamic tensile tests at two distinct strain rates to assess mechanical properties.

- SEM imaging: Scanning Electron Microscopy (SEM) images were taken in order to examine the fracture surfaces of specimens following tensile failure.
- Dimensional analysis: The dimensions of both sets of samples were measured to calculate shrinkage and Oversizing Factor (OFS).
- Density measurement: The densities of the specimens and their thermal diffusivity were determined to compute thermal conductivity.
- Corrosion evaluation: Potentiodynamic polarization curves for both sets of specimens to evaluate their corrosion resistance were generated by partners at the University of Modena e Reggio Emilia.
- Results discussion and analysis: The obtained results were analysed and discussed, drawing comparisons with existing literature.

This comprehensive methodology was employed to systematically investigate the mechanical properties and corrosion performance of 3D-printed stainless steel parts using the MFFF process. Apart from the instances that the samples were outsourced, all the experimental procedures were performed in the Polymers and Composites Lab of the *Dipartimento di Ingegneria Civile e Architettura* (DICAR) of University of Catania, under the Erasmus + Traineeship program.

1.4. THESIS OUTLINE

This thesis is structured into five main sections. The introductory part provides an overview of the thesis' background, motivation, key objectives, and the primary methods employed to achieve them. Chapter 2 presents an extensive literature review, with a focus on MFFF 3D printing technology. It includes discussions on post-printing processes, the impact of printing parameters on part characteristics, and the tensile and corrosion properties of parts produced using this technology, among other relevant topics. Chapter 3 details the experimental procedures, materials, and equipment utilized throughout the research. It also outlines the geometry and manufacturing specifications of the 3D printed specimens used in testing, along with descriptions of the testing setup. Chapter 4 provides a comprehensive overview of the study's primary findings, accompanied by a detailed discussion and analysis of these results. Finally, Chapter 5 summarizes the key conclusions drawn from the study and offers suggestions for future research directions within the field of MFFF related to mechanical and corrosion performance.

2. LITERATURE REVIEW ON METAL FUSED FILAMENT FABRICATION

In this chapter we're delving into a comprehensive analysis of existing research and developments in the field of MFFF. This chapter serves as a foundation, exploring relevant studies, advancements, and techniques related to MFFF for mechanical applications. By delving into these key areas, an understanding of the current state of the art in this metal-based additive manufacturing process is provided. The forthcoming subchapters will explore the complexities of this technology, encompassing process parameters, feedstock filaments, material properties, and other essential aspects. Through this exploration, this section aims to establish a solid foundation for the subsequent investigations in this subject area.

2.1. PROCESS CHARACTERIZATION AND PRINCIPLES

Despite its simple fundamental nature, FDM/FFF is capable of manufacturing complex geometries. Firstly, metal powder is mixed with thermoplastic binder polymers and additives to form the feedstock. In the MFFF process, a continuous filament is used most of the times, but pellets with the same composition may also be utilized in some versions of the process, although in this case it would be more appropriate to give the process the name of 3D Extrusion Printing (3DEP) [4]. In the case a filament is used, they are extruded from the feedstock, and can then be used for 3D printing on commercial FFF machines [5].

During the printing process, the filament is fed from a large coil by the use of small gears controlled by an electric motor and it is then melted by a heated liquefier at a temperature around the binder's melting point. This is what makes it possible to shape the material filled with metal particles without having to melt the metal itself. The melted material is then forced through a nozzle typically with a diameter between 0.4 and 1.0 mm [1], which deposits it on the heated platform and the part is printed layer-by-layer in 3D following a CAD model. Step motors are used to move the liquefier/print head assembly over a platform in an XY plane allowing the printing of a single layer. This setup is depicted in Figure 2.1. Following the completion of deposition at the cross-section, the platform or print head travels exactly one layer thickness in the Z direction. As a result, a layer-by-layer procedure is used to form the three-dimensional structure. Until the part is constructed, this procedure is continued. The speed of the extruder head may also be controlled, to stop and start deposition and form an interrupted plane without stringing or dribbling between sections [2, 5, 4].
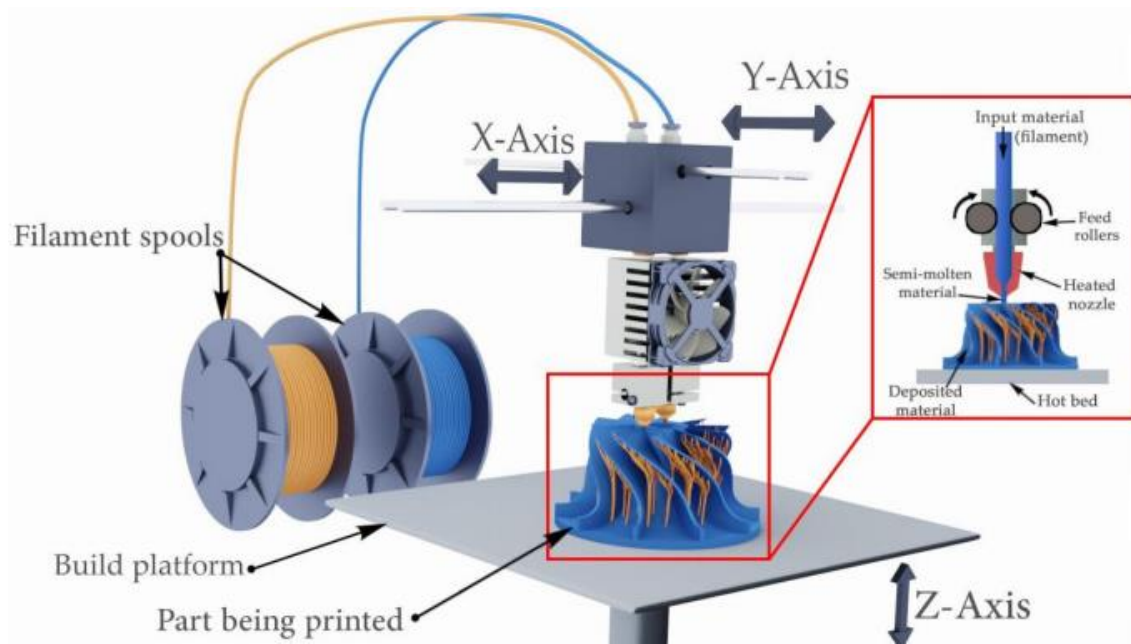
Figure 2.1 - The scheme of the FFF printing setup [6].

Achieving satisfactory quality of metal parts produced by FFF involves optimizing the feedstock composition through the development of appropriate binder systems and adjusting powder properties such as particle size. Feedstocks can be processed similarly to regular polymers, albeit with higher viscosity. Ultimately, the viscosity limits the achievable fill grade to a maximum of 55-65 vol.%. Any more than this, and the filament cannot be processed by the FFF hardware. The post-shaping processing is crucial for the quality of the printed parts. It usually consists of a solvent or acid treatment to remove most of the polymeric binder (solvent/catalytic debinding) followed by a thermal cycle to remove the rest of the polymeric backbone (thermal debinding) and to sinter the parts (sintering). This is commonly referred to as the Shaping, Debinding and Sintering (SDS) process. The quality of the parts is also highly influenced by the printing parameters, which must be optimised and different than those used for polymeric filaments. In the next sections, these steps will be explained in greater detail [4, 1]. The full SDS for the MFFF process is schematically summarized in Figure 2.2.
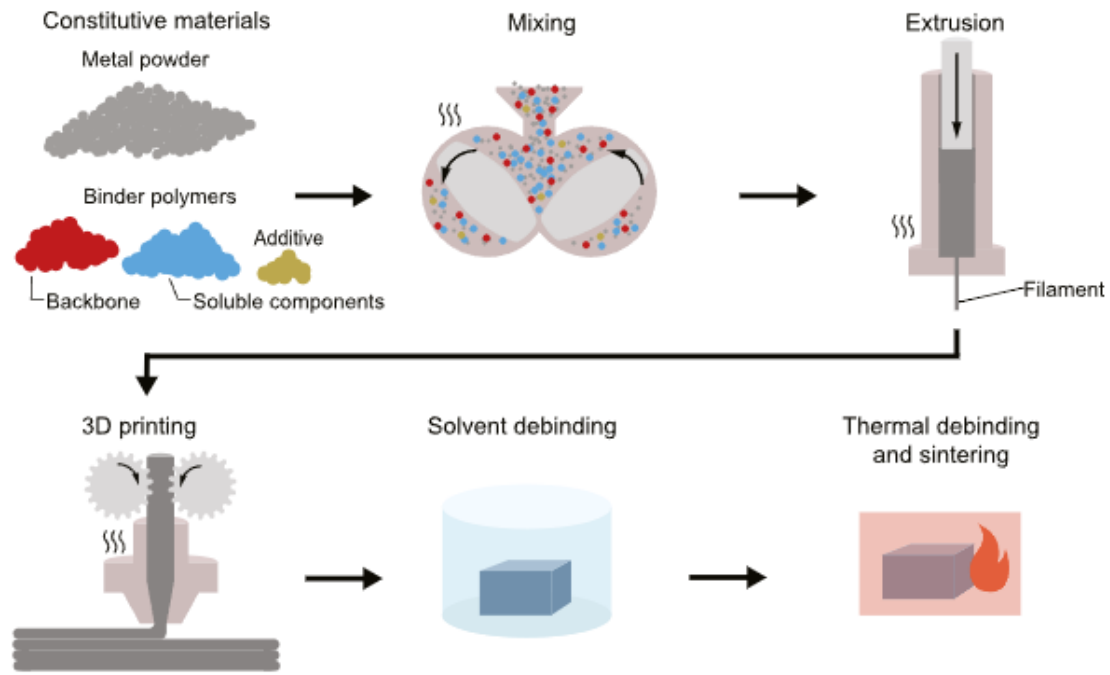
Figure 2.2 - Schematic of the full SDS associated with the MFFF process [3].

It is important to note that parts are scaled up 15%-30% from the final part dimensions to account for repeatable/predictable shrinkage during sintering process. Newly printed parts are called "green" parts. The following image shows the visible difference in size between a green part and a sintered (or white/silver) one [5, 7].
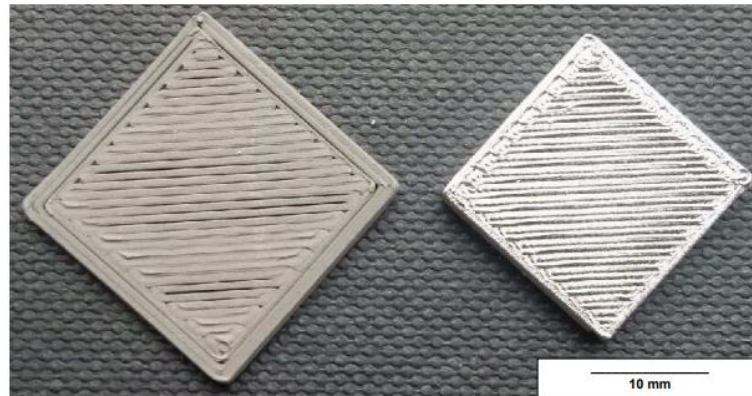
Figure 2.3 - Printed green specimen (left) and sintered white part (right) [5].

The printed green body is then put through a debinding process. Debinding eliminates most of the binder material in the green part. This process is infuenced by two factors: the kind of debinding (solvent, thermal, catalytic, or combination of these), and the thermal cycle of the debinding process. Compared to solvent and catalytic debinding, thermal debinding is relatively slow and easy to regulate. The solvent debinding provides a transport channel for removing reminded binder during thermal debinding. Temperature is a critical component in the debinding stage and must be precisely regulated [8, 9].

Depending on the binder system, a single thermal debinding step may be used, or thermal debinding may be combined with a previous main binder removal. In a two-step, the binder system is made to have a main component and a backbone, which ensures structural integrity during solvent debinding [1]. The former is removed via dissolution using an organic solvent, such as cyclohexane [3, 5, 1] or acetone [10] (or even water in the case a water-soluble polymer is used) or by catalytic depolymerization [9]. The latter is thermally decomposed inside a furnace. A network of open pores is introduced once the first binder is removed. Through these pores, the backbone's gaseous thermal breakdown species can subsequently escape, preventing any defects [3, 5].

Thermal debinding and sintering are carried out in a furnace with heating components and a debinding retort (small chamber or enclosure with a controlled atmosphere), for example, in a hydrogen atmosphere. The green components are placed on sintering supports and the backbone polymer is removed by gradually raising the furnace's temperature from ambient temperature to the point at which the backbone polymer begins to thermally degrade. The steel specimens are then sintered by being heated to even higher temperatures, around 70% to 90% of the metal's melting point [7], and held for a predetermined period. Due to multiple diffusion processes, powder particles fuse together at these high temperatures during sintering, decreasing the total surface area and volume of the part and producing dense metallic structures. Subsequently, furnace cooling is applied at a rate significantly faster than the heating process. To obtain high sintering densities, powder loadings of at least 50 to 60 vol.% are often necessary, which is allowed by the limit filament viscosity. The finished white parts can have relative densities between 95% and 99.5% if factors like filament solid loading, printing and sintering align to make a high-quality part [3, 4, 7]. The thermal cycle is represented in Figure 2.4.
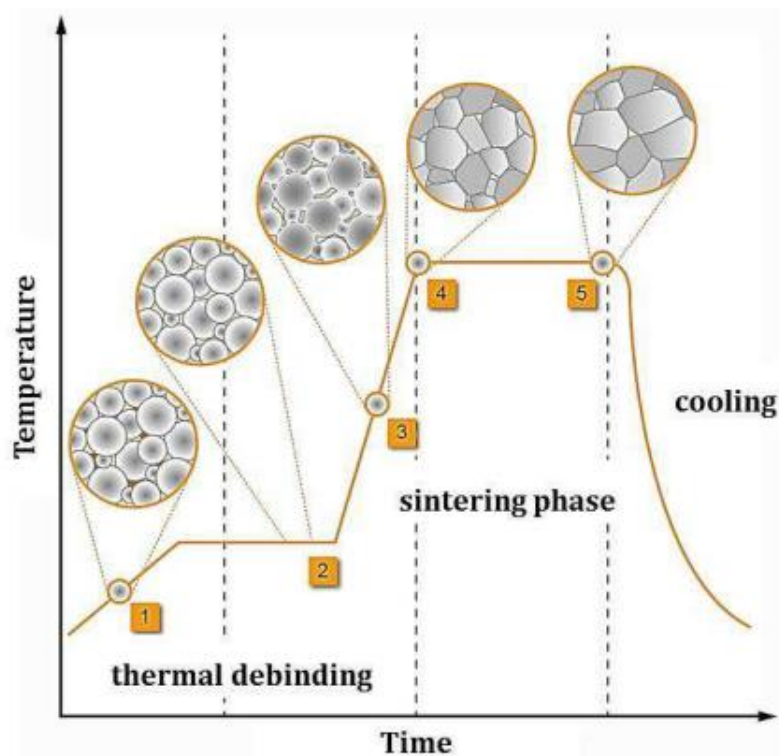
Figure 2.4 - Thermal debinding and sintering cycle [5].

2.1.1. DIRECT EXTRUSION AND BOWDEN EXTRUSION PRINTERS

Not all FFF 3D printers are the same. Depending on the extrusion system they have, they can be categorized as a direct extrusion or a Bowden type printer. An extruder is one of the most important parts of any 3D printer with FDM technology. It is the mechanism that is responsible for pushing the filament from the spool to the hot nozzle tip to be melted. In general, there is some degree of ignorance on this subject. It is convenient to have some basic notions about certain important features of the printer, as they will affect the choice of the machine itself and the material to be handled. Thus, we will make a brief distinction between the two extrusion modes that a 3D printer can have [11].

A Direct Extruder is the most common in 3D printers, although in recent years this trend is being reversed. Its main feature is that the extruder, with all its components, is mounted all in one piece. Direct extrusion consists of placing the motor that pushes the filament directly on the nozzle end. That is, in this drive system, both the extruder and the nozzle would be joined in the moving head of the 3D printer without being separated by a tube. It is the ideal system for extruding flexible filaments, since its advantage is that it pushes the filament close to the hot tip and it is easier to be calibrated. In this way, a good control of the material retraction is achieved to obtain a better finish in the parts [11]. In Figure 2.5 a direct extruder is depicted.
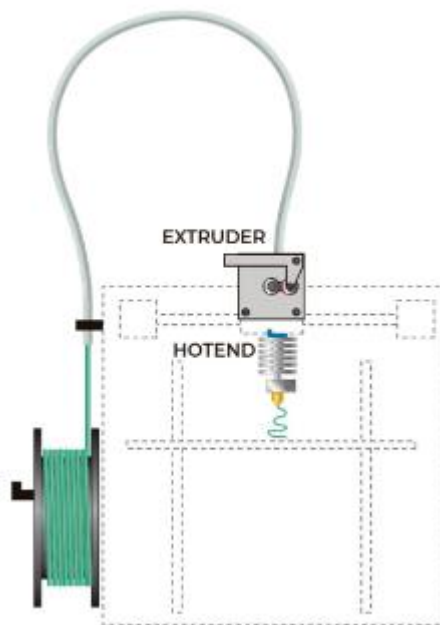
Figure 2.5 - Direct Extruder Printer scheme [11].

On the other hand, the indirect extrusion or Bowden type extrusion consists of removing the filament pusher motor from the moving parts and placing it in the structure of the printer in a way that the filament does not pass directly from the motor to the nozzle, as in direct extrusion, but with this technique the filament is guided to the hot nozzle through a tube. This tube is usually made of PTFE (polytetrafluoroethylene, better known

as Teflon) and usually has an internal diameter slightly larger than that of the filament to compensate for manufacturing tolerances that the filament may have [11].

Bowden extrusion, displayed in Figure 2.6 has the advantage of reducing the weight of the moving filament, which results in the ability to print at higher speeds. Given the complexity of pushing a flexible filament through a tube, from the extruder to the nozzle, it is very difficult to print with flexible filaments. So, it has the disadvantage of being a system susceptible to jamming and buckling of the filament. This may happen specially if the tube and filament diameters are not in concordance, as shown in Figure 2.7. The greater the flexibility of the material, the greater the probability of jamming in the tube [11]. In Table 2.1 some advantages and disadvantages of each type of extruder are displayed.
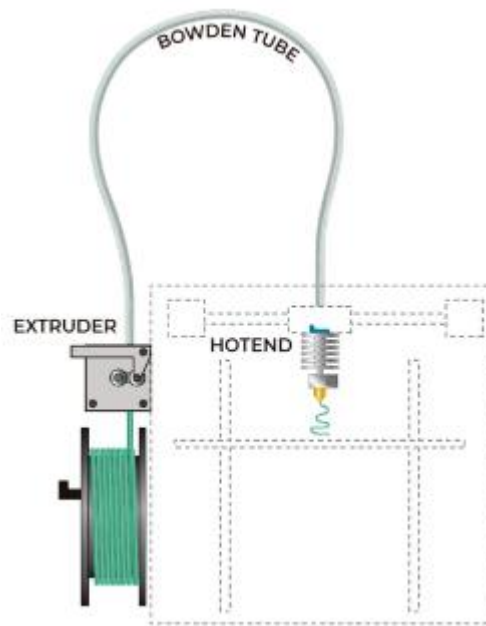
Figure 2.6 - Bowden Extruder Printer scheme [11].
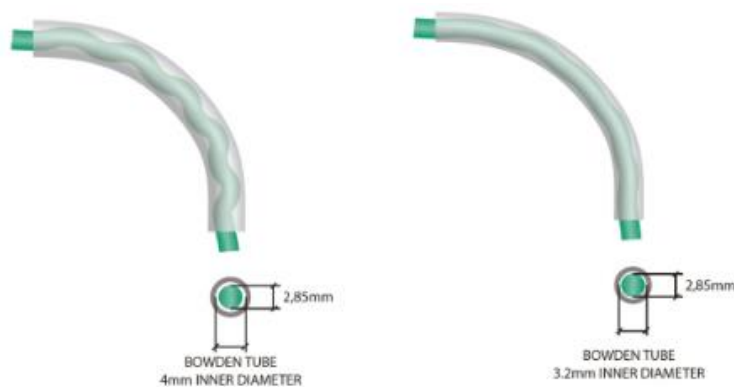
Figure 2.7 - Filament buckling and jamming due to the large gap between the Bowden tube and the filament diameters [11].

Table 2.1 - Advantages and disadvantages of each extrusion type [11].

Extrusion type	Advantages	Disadvantages
Direct	- Allows printing with flexible filaments. - Possibility of printing with all types of materials. - Compact and completely removable extruder. - Easy access and manipulation to check malfunctions or clogging. - Allows better control of shrinkage. - Reduction of calibration problems.	Difficulty of mobility in the X and Y axes due to the weight it adds (increased inertia).
Bowden	- Less weight on the X and Y axes. The inertia is reduced, so printing head can move easily and the printing speed can be higher improving the printing quality. - Greater pulling power of the filament from the spool to the nozzle.	- Limits the range of ideal materials to print. - Problems to print with thin and/or flexible filaments due to existence of the tube. - Higher probability to suffer failures.

2.1.2. PRINTING PARAMETERS AND PART CHARACTERISTICS

The MFFF process has an endless amount of process parameters, and they have a significant impact on production efficiency and part characteristics. The pore distribution in a MFFF produced part is strongly linked to the build orientation and printing strategy. Inadequate printer settings may leave gaps between printed lines and subsequently in sintered parts. These parameters can be classified as operation-oriented, machine-oriented, material-oriented and geometry-oriented [2, 7, 12]. Some of the most important printing parameters are described below:

- Air gap: The gap between two adjacent rasters on a deposited layer (Figure 2.10). The air gap is called negative when two adjacent layers are overlapped [12].
- Build orientation: Build orientation is defined as the way to orient the part in a build platform with respect to X, Y, and Z axes. In some papers, build orientation represented a quantitative parameter, but in others, it was considered a categorical parameter. It is common to consider a part at a 0° orientation as being in a "flat" position and a part at 90° as being in an "upright" position. These orientations are shown in Figure 2.8 [12].
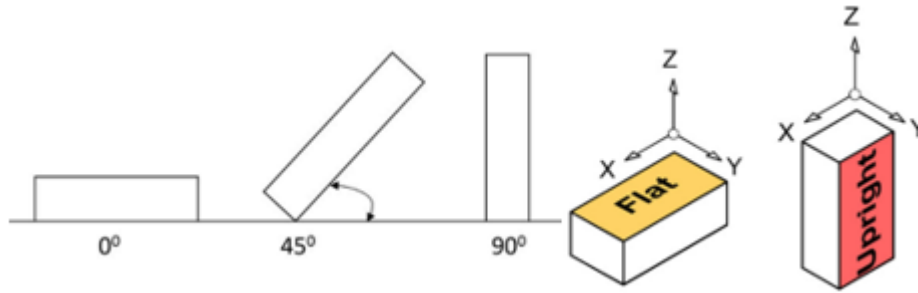
Figure 2.8 - Build orientation: numerical (left) and categorical (right) [13, 12].

- Extrusion temperature: Also known as nozzle temperature, it is the temperature at which the filament of a material is heated during the process. Extrusion temperature depends on various aspects, for example, the type of material or print speed. Extrusion temperature should be above melting temperature of the filament binder to increase flowability of the filament allowing it to be extruded. At lower than required extrusion temperature viscosity of filament will be too high for continuous extrusion, if higher than required temperature is selected then material will not solidify instantly after deposition and will likely cause defects [7, 12].
- Infill density: The outer layers of a 3D printer object are solid. However, the internal structure, commonly known as the infill, is an invisible inner part covered by the outer layer(s), and it can have different shapes, sizes, and patterns. Infill density is the percentage of infill volume with filament material. The strength and mass of MFFF build parts strongly depend on the infill density. It can and it should even be slightly superior to 100%, making the printing lines slightly overlap and avoiding positive air gaps [12].
- Infill pattern: Different infill patterns are used in parts to produce a strong and durable internal structure. Infill patterns can be arranged in lines, triangles, in a grid or many other patterns. These examples are shown in Figure 2.9 [12].
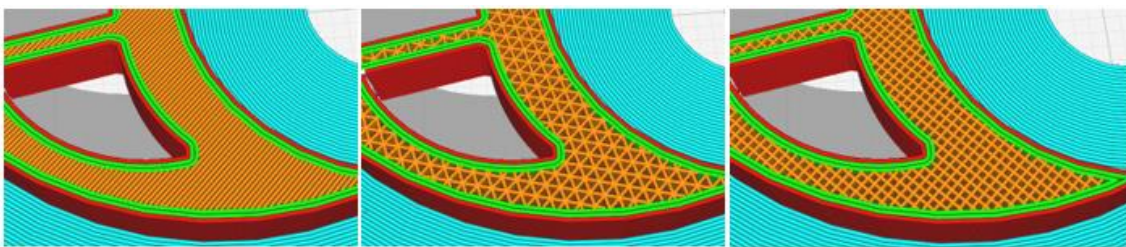
Figure 2.9 - Different infilll patterns: lines (left), triangles (center) and grid (right) [images taken directly from the Ultimater Cura slicer software]

- Layer thickness: This is the height of the deposited layers along the Z axis, which is generally the vertical axis of an FFF machine. Generally, it is less than the diameter of the extruder nozzle and depends on the diameter of the nozzle. It is advisable that layer height should not be more than 80% of nozzle diameter [7, 12].
- Print speed: This is the distance travelled by the extruder along the XY plane per unit of time while extruding. Printing time depends on print speed, and the print speed is measured in mm/s [12].

- Flow rate: The width and thickness of the line, as well as the head (hot end) speed (print speed), are employed conjugatively to control the flow rate of the material extruded from the nozzle. It is also advisable to set this value at around 105-110% as slight over extrusion will fill up the gaps between extruded lines and will result in high density of green body [14, 7].
- Raster width: Raster width is defined as the width of the deposition beads (Figure 2.10). It depends on the extrusion nozzle diameter [12].
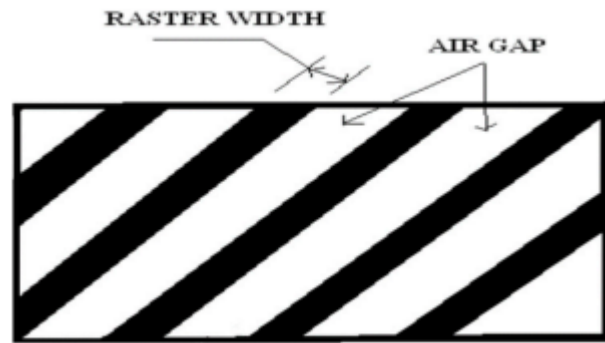
Figure 2.10 - Raster width and air gap [12].

- Raster orientation: This is the direction of the deposition bead with respect to the X-axis of the build platform of the FFF machine (Figure 2.11) [12].
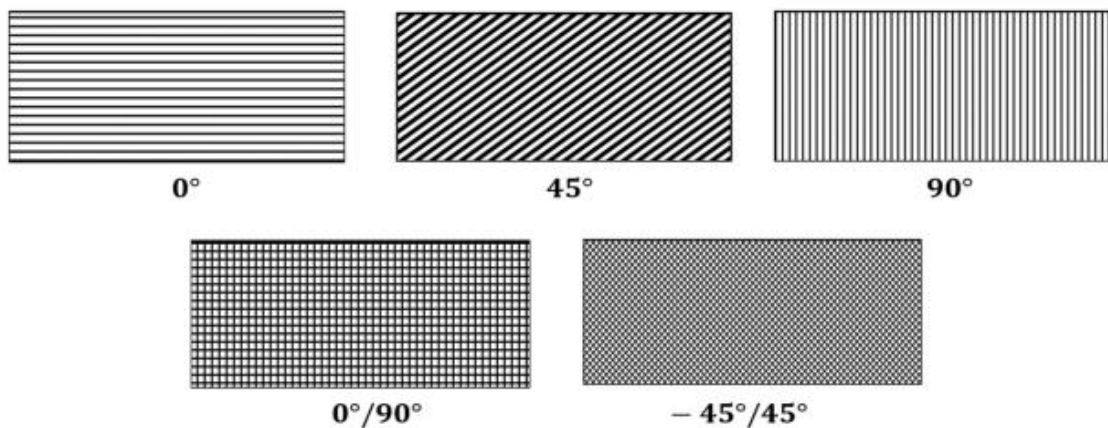
Figure 2.11 - Raster orientation [12].

- Fan speed: It is also advisable to optimize the cooling fan speed as very high speed will reduce the temperature of deposited material and can result in the lack of bonding between adjacent layers and, consequently, strength of the part can get affected. Very high cooling rate can also reduce the temperature of nozzle resulting in clogging. It was also reported that low fan speeds result in insufficient cooling of deposited material which causes them to easily deform. Below (Figure 2.12), we can see the effects of a decrease in cooling fan speed paired with an increase in the nozzle

temperature in an open box structure, which is a difficult situation in terms of cooling airflow [1, 7].

increasing nozzle temperature, lower fan speed

a)   b)   c)   7 mm
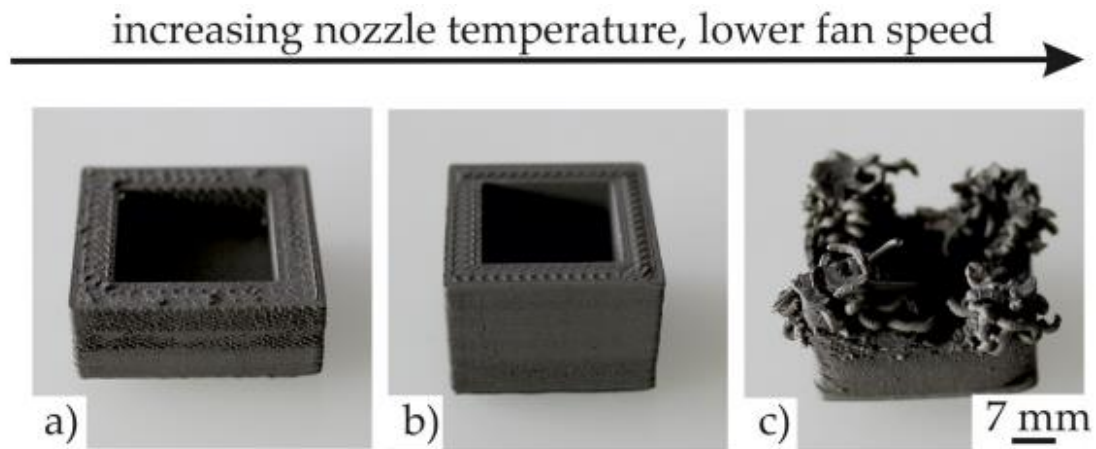
Figure 2.12 – Effect of low fan speed coupled with higher nozzle temperature in a MFFF printed open box structure. From a) to c), the result of cooling speed reduction is shown [1].

The influence of printing parameters on the characteristics of MFFF parts is not straightforward and involves a complex interplay of factors. The described parameters collectively impact the final properties of the printed metal parts. The relationship between these parameters is highly interdependent and there's not much information about how many of them relate to each other, making the optimization of specimen properties a challenging task. For instance, adjusting the layer height might affect the print speed and material flow rate, which in turn could impact the cooling rate and bonding between layers. As a result, finding the right balance between various printing parameters to achieve desired properties in the printed specimens requires careful experimentation and empirical testing. Presented below is a fishbone diagram illustrating the impacts that different parameters have on various part characteristics. Following the diagram, a written summary is provided to explain how these parameters interact and influence some of the final part characteristics.
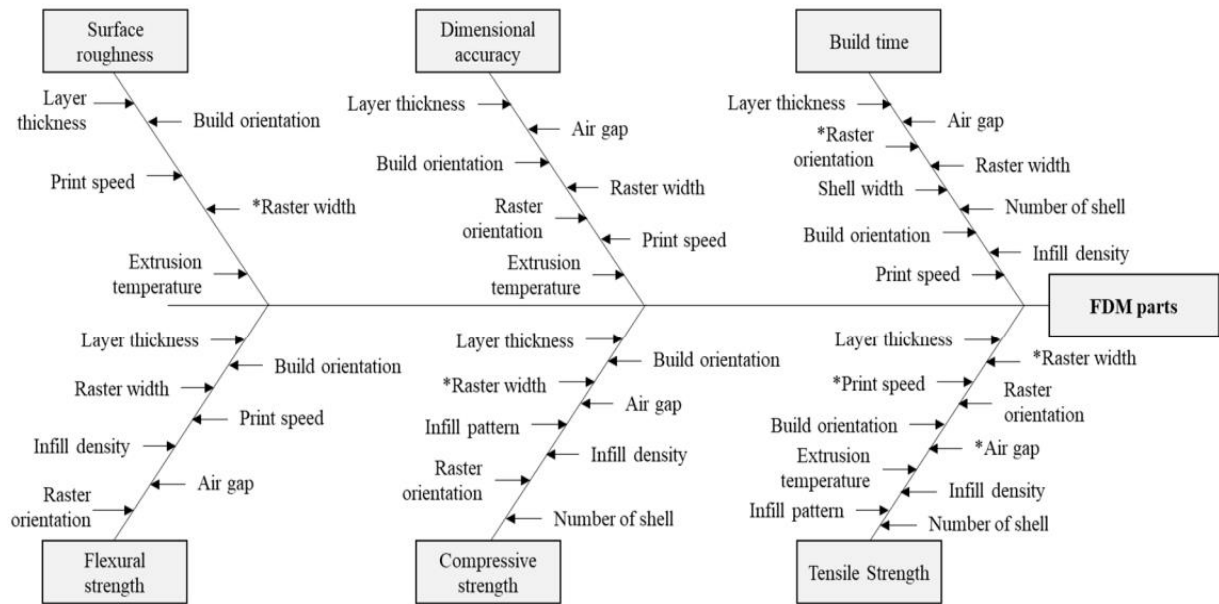
Figure 2.13 - A fishbone diagram to illustrate the impacts of process parameters on part characteristics [12].

- Dimensional Accuracy: While the most significant alteration in part dimensions occurs post-sintering, it is important to acknowledge that a similar issue also arises during the pre-sintering phase in the SDS process. Notably, the parts' dimensions and geometry after printing do not precisely match the initial design modelled in the software. Hence, it becomes imperative to grasp the impact of printing parameters on this disparity. Enhancing dimensional accuracy after printing directly correlates with achieving greater precision in dimensions following the sintering process. The layer thickness is one of the most analysed and influential factors for dimension accuracy. Most of the researchers concluded that, in general, high dimensional accuracy is obtained by setting a low layer thickness, extrusion temperature and number of shells. It is important to know the influence of those parameters and how they influence each other to produce a part with high dimensional accuracy. It is observed that shrinkage (relative to the computer-aided design (CAD)-defined thickness) occurs along X and Y directions of build platforms and expansion is experienced along the Z direction of the build platform. Besides, there may be a slight change in layer thickness and, consequently, on the dimensional accuracy in the Z direction, depending on the print speed and nozzle temperature (Figure 2.14). From this, we can conclude that build orientation is also an important parameter of dimensional accuracy. Most of the existing research about parameter optimization considered only two or three levels of parameters. There is a need to analyse more than three levels of parameters to make a more accurate decision, and to study the impact of the least known parameters on dimensional accuracy (such as infill pattern, or nozzle diameter) [12].
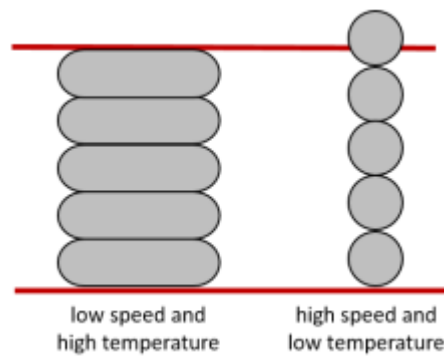
Figure 2.14 - Effect of printing temperature and printing speed on the dimensional accuracy in the Z direction [6].

- Surface Roughness: A better surface finishing can be achieved by selecting a low layer thickness because it helps reduce the staircase effect on the printed parts, especially on curved surfaces. Other than layer thickness, low extrusion temperature and print speed are preferable to achieve a higher print precision. A high extrusion temperature increases the fluidity of filament materials and further results in high dimensional deviation and surface roughness. Most studies indicate that the surface finish of a top printed surface is better than the side surface for any setting of process parameters. Therefore, printing the shortest side of a part in the Z direction is recommended for the FFF process to reduce the overall surface roughness [7, 12].
- Build Time: Build time was found to be minimum at a high layer thickness (as number of total layers to make the component decreases), low infill density and print speed. Minimum build time means that it is faster to print a part. The impact of raster orientation and raster angle on build time is still unknown. Thus, further analyses are still needed to draw a more valid conclusion. On a separate note, build time may also be significantly affected by the hardware itself. A good FFF machine typically can produce a relatively good-quality part faster than a lower quality FFF machine. One further research direction is to study the influence of the infill pattern and extrusion temperature on build time [7, 12].
- Tensile Strength: Compared to any other part characteristics, tensile properties, especially tensile strength, are the most analysed part characteristics in MFFF printed parts. From existing research, the build orientation was found to be one of the most significant parameters, and tensile strength was maximum at 0° (or flat/on-edge) build orientation. At this build orientation, the direction of filament fibre extrusion is parallel to the direction of the applied load. Higher layer thickness is recommended for tensile properties. The interlayer contacts can be the weakest points in green printed specimens due to incomplete polymer chain diffusion, void introduction, which produces a reduced cross-section area, and stress concentrations. Consequently, reducing layer count (increasing layer thickness) yields green specimens with superior tensile properties. This enhancement extends to the final white parts. It is safe to conclude from current research, as well as general knowledge, that tensile strength is maximum at high infill density and a high number of shells. At higher density, interlayer bonds become stronger and voids/porosities are decreased. Relatively higher extrusion temperatures are preferable for tensile strength. This is because, at a high temperature, the fluidity of the filament increases, and interlayer bonds become stronger. Moreover, lower extrusion temperatures interfere with material deposition, resulting in more air gaps and reduced cross-

sectional area, contributing to decreased properties. The optimum raster orientation for tensile strength is still contradictory, but it may be concluded that a 0°/90° or −45°/45° raster orientation is optimum. Additionally, an increase in flow rate is proven to be a critical element to significantly increase all mechanical properties and sample density, as it makes porosity and average grain size decrease. A higher multiplier pushes more material through the nozzle, enhancing the cohesion of deposited lines and promoting overlap. This effectively reduces the gaps between strands and strengthens interlayer connections [14, 12, 15].

- Part Geometry: The characteristics of an FFF part tend to deteriorate as the complexity of its geometry increases. For instance, flat-surfaced parts typically exhibit better surface quality and dimensional accuracy compared to cylindrical or pyramid-shaped parts. The staircase effect is a common issue in the FFF process. In many extrusion AM methods, it is necessary print the specimens alongside shaping supports. These supports help maintain the part's shape, position, and stability throughout the entire process, from printing to post-sintering, especially for surfaces with overhangs less than 45°. However, using proper support structures and managing their removal can be complex and requires careful attention. The removal of these support structures can sometimes lead to a reduction in part quality. Consequently, it is crucial to determine the optimal process parameters for various geometrical configurations to minimize printing errors and defects. Bridging the gap between complex part geometry and process parameters to enhance part characteristics represents an important area for research in optimizing FDM part quality [8, 12].

2.1.3. SOLVENT DEBINDING

For FFF-based AM of metal and ceramic parts solvent debinding is the most common process as wax or polymers are soluble in certain chemical solvents [7]. In this process, the green parts are submerged in the solvent at a temperature between 50-70℃ [3, 5, 4, 1, 10]. The ratio between soluble polymer and solvent should be kept low to avoid saturation effects in the solvent [3].

The removal of the polymer can be divided into two distinct stages (Figure 2.15). Previous studies have observed this two-stage pattern, with an initial rapid removal of the polymer followed by a significant slowdown. This could be justified by the mechanism controlling the rate of the process changes. Initially, the rate is determined by how quickly the polymer chains dissolve and extract the soluble components from the material. The removal of the dissolved polymer chains near the surface happens quickly due to the short distance they need to travel. However, as the solvent debinding progresses, the paths that the dissolved polymer chains must take to escape the material become longer. Consequently, this step becomes the limiting factor in the overall process. Experimental evidence has demonstrated that this effect does not occur due to the utilization of multiple polymeric binders. In this case, after 8h of solvent debinding the soluble portion was removed from the specimens and a porosity is induced [1, 8]. As mentioned, these pores function as a route for backbone polymer removal during thermal debinding and naturally also enable accelerated heating during subsequent steps. After solvent debinding, the specimens can be dried in air at ambient conditions [3, 1]. Figure 2.16 illustrates SEM images of a printed part before and after the solvent treatment.
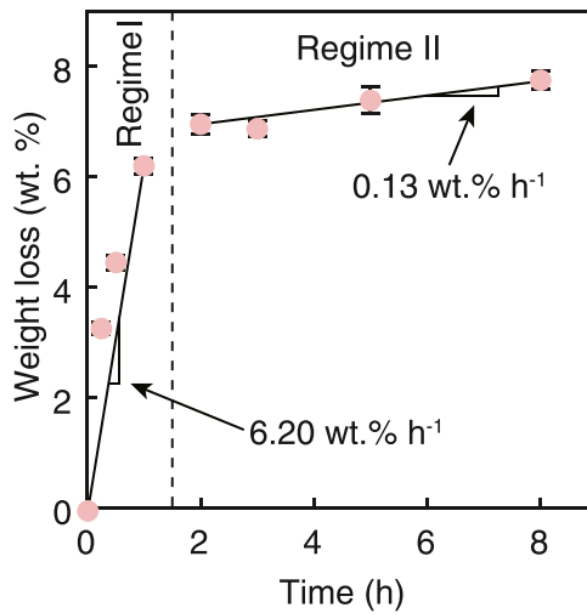
Figure 2.15 - Weight loss over time for solvent debinding of a certain filament [3].
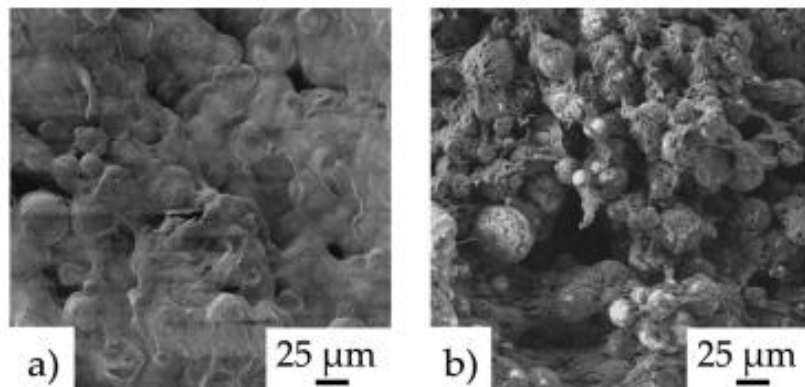
Figure 2.16 - (a) SEM image of a printed microstructure without solvent debinding and (b) a completely solvent debound structure [1].

The SEM image in Figure 2.16b further demonstrates how the backbone polymer guarantees the stability of the sample following solvent debinding: The backbone polymer is used to create a net of polymeric threads that surround and keep the powder particles in place. As a result, even after complete solvent debinding, the backbone polymer maintains the printed component's form and stability [1].

While the overall solvent debinding follows the generally observed kinetics trend, the precise time and amount of dissolved binder at which the rate changes is expected to be strongly influenced by the surface to volume ratio and size of the specimen. Besides, it is also influenced by some printing parameters, such as the wall thickness. In Figure 2.17 one can see the difference between the weight loss of a main binder component (also a TPE) in two parts with different wall thicknesses, specifically, 2 mm and 6 mm. The weight loss of the component was measured in regular intervals over the debinding time. As indicated in

Figure 2.17, total solvent debinding time, that is, the time at which 99% of the contained TPE was removed, was 57 h for a wall thickness of 6 mm, but for a wall thickness of 2 mm the time was considerably smaller, corresponding to around 24h of immersion time [1].
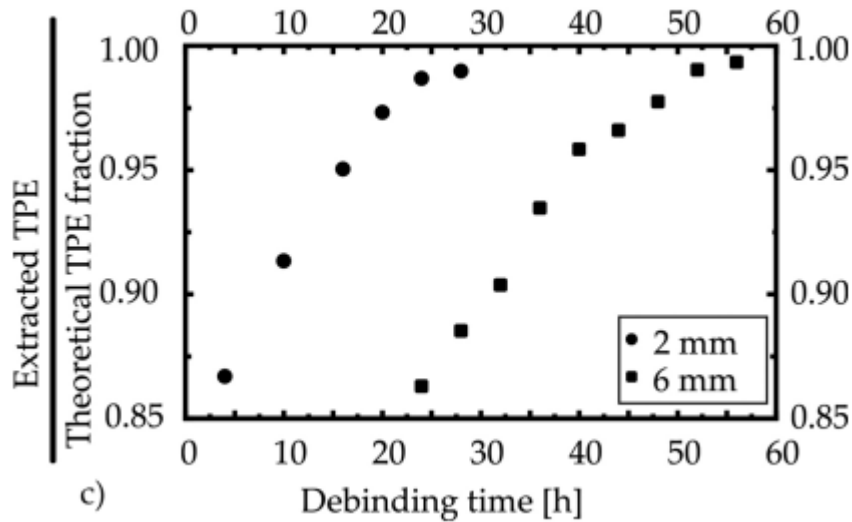
Figure 2.17 - Extracted TPE during solvent debinding for two wall thicknesses (2 and 6 mm) [1].

2.1.4. CATALYTIC DEBINDING

Catalytic debinding is another method used to remove the binder from metal powder-filled feedstock filaments. In this process, the main binder is attacked directly by a catalytic acid vapor. The binder is primarily converted into a vapor by the catalyst and then blown away. The key component for the success of catalytic debinding is the Polyoxymethylene (POM), commonly referred to as polyacetal, molecule present in the binder. When exposed to a suitable acid catalyst, the oxygen atoms in the polyacetal chain are prone to acid attack, leading to the conversion of POM macromolecules into formaldehyde [9].

Nitric acid gas, with a purity of more than 98%, is often used as the catalyst in this process. The catalytic debinding approach is generally faster than thermal and solvent debinding methods, producing a well-interconnected porosity in a relatively short time. However, to avoid excessive heating and potential part collapse, the debinding process must be carefully controlled for high-density parts [9].

The process involves using nitrogen gas as a carrier to exhaust oxygen before the degradation begins, as oxygen and formaldehyde together can cause an explosion. The catalyst is injected into the oven using a ceramic piston pump, and ovens used for catalytic debinding have corrosion-resistant internal surfaces against nitric acid [9].

Catalytic debinding is particularly effective for parts with high powder density, as the gas can easily penetrate the pores to reach the binder. Therefore, has been successfully applied to stainless steel parts with specific binders. When this debinding method is used, as already indicated, the binder system is always composed of POM, and it is also very frequently composed of Polypropylene (PP), Dibutyl phthalate (DBP), and Dioctyl Phthalate

(DOP). The last two components act as plasticizers to increase the filament's flexibility and workability. Moreover, the procedure is commonly done at temperatures close to 120°C. [16, 17, 18, 19].

However, the process has a limited application range compared to thermal and solvent debinding methods. Nevertheless, it offers a fast and efficient way to prepare parts for sintering, provided that the parameters are carefully controlled and the specific requirements are met [9]. This process is displayed in Figure 2.18.
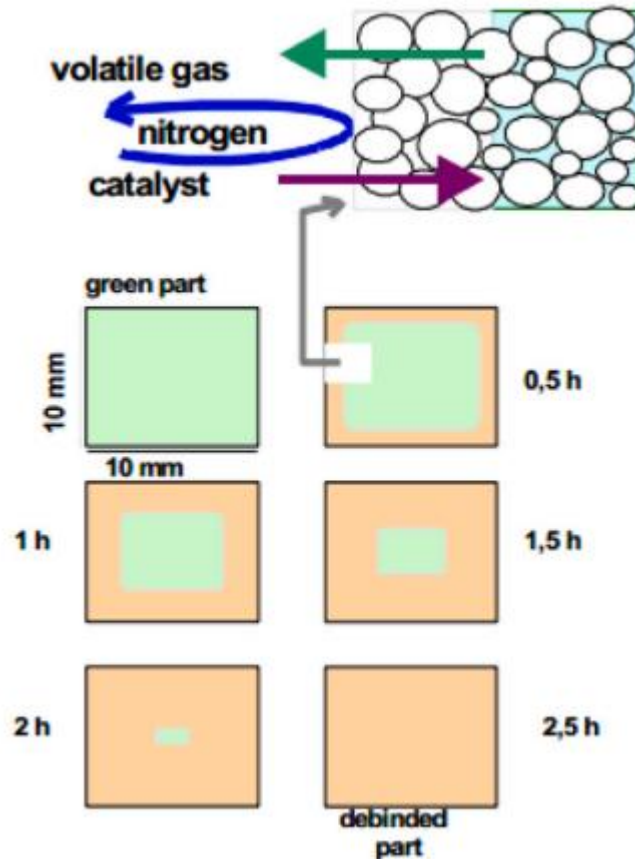
Figure 2.18 - Example of catalytic debinding progress as a function of time [9].

2.1.5. THERMAL DEBINDING AND SINTERING

The most common and straightforward method to remove the binder from parts is through thermal debinding, especially when the binder is a thermoplastic polymer. The process heavily depends on thermal degradation and Thermogravimetrical Analysis (TGA) is a widely used method to track thermal degradation progress. Although when applied by itself, thermal debinding makes the part more brittle and susceptible to cracking, examples of successful thermal debinding of parts made with Powder Material Extrusion (PME) are found in current literature, demonstrating that a range of ceramic and metal parts with different binders can be successfully prepared for sintering using simple and common equipment [9].

Thermal debinding and sintering are continuous operations that occur one after the other and usually in the same furnace. Three main parameters influence the outcomes: temperature, time, and furnace atmosphere. Utilizing a gradual and regulated temperature cycle is critical in sintering, as it is in the debinding of the backbone [8].

There are two basic methods for the polymer to be removed from the compact during thermal debinding. Liquid polymer is first pushed to flow from the interior to the outside surfaces because of rising internal pressure, where it then degrades and exits. Second, the internal liquid polymer further degrades into vapor and flows to the outer surfaces by convection and diffusion. The predominant mechanism is determined by the gas species' mean free path, which varies with pressure, molecular weight, and pore size. Diffusion will rule at low pressures and tiny pore sizes. Both methods leverage the pore channels created by solvent or catalytic debinding as a means of transport for the polymer. As a result, the heating rate must be adjusted to the flow velocity of the decomposition products. It was demonstrated experimentally that excessive heating rates resulted in the formation of large pores inside the bulk metal as well as the bloating/blistering or cracking of the components, notably on the surfaces (Figure 2.19b). Even greater heating rates, as seen in Figure 2.19a, leads to a complete loss of the brown body shape due to the excessively fast polymer decomposition. Slow heating enables thorough binder removal and defect-free debinding (Figure 2.19c). A thinner wall allows for a higher heating rate since the wall thickness, which mostly determines the escape rate, is reduced [1, 8].
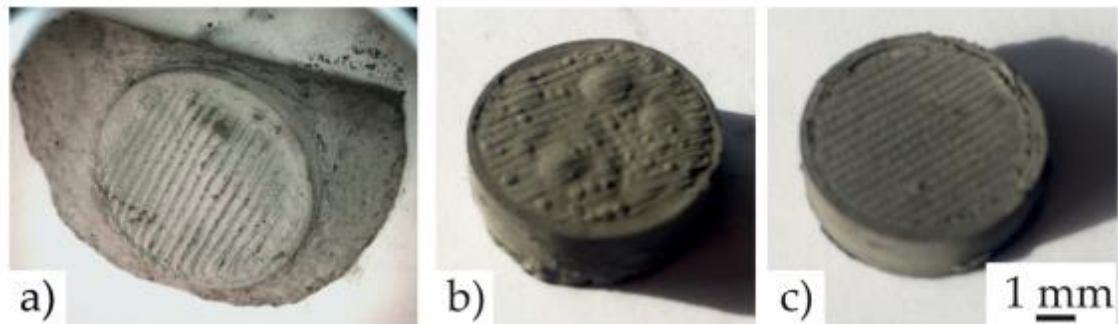
Figure 2.19 - Thermal debinding of a 6 mm thickness cylinder at different heating rates [1].

It is noteworthy that furnaces with a vacuum or inert gas environment should be used for sintering to avoid thermal oxidation of the powders and, as a result, the final component. Various atmospheres have different effects on microstructure. As depicted in Figure 2.20, a thick, elongated film forms at the grain boundaries during M2 high-speed steel samples' sintering at 1200°C in a vacuum, which indicates over-sintering. However, a homogenous structure was obtained when the samples were sintered in a N2–H2 atmosphere. The sintering environment can also affect the chemical composition of sintered samples [8].
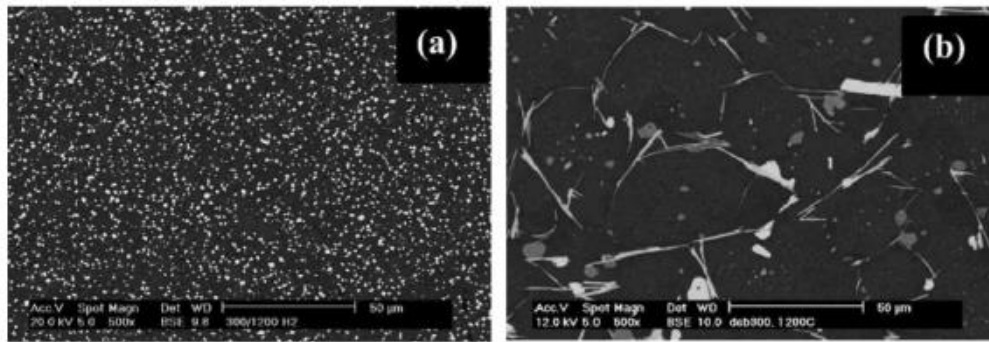
Figure 2.20 - SEM images of M2 high speed steel samples sintered at 1200 °C in: a) N2–H2 atmosphere and b) vacuum [1].

Mechanical stability of printed parts after complete thermal debinding is provided by sintering necks. In Figure 2.21, the necking process is schematized and we can see that necking between metal particles occurs as time and temperature rise. As sintering continues, the size of the neck rises, and the dimension of the pores decreases [1, 8].
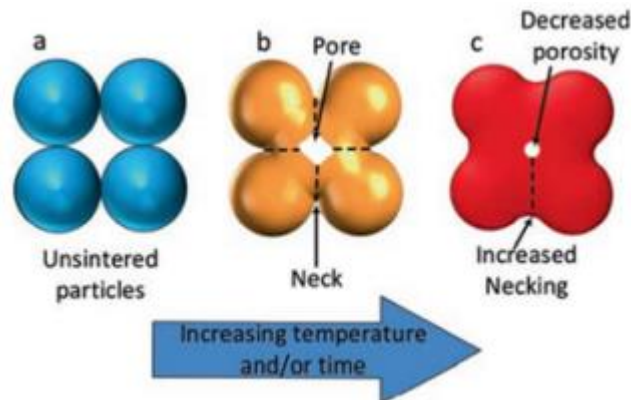
Figure 2.21 - Joining of base metal powder particles during sintering [8].

Below, in Figure 2.22a there's an example of a thermogravimetric analysis measurement (which reveals mass loss rate at a given temperature with a given heating rate) of 316L stainless steel parts and it indicates an onset of the degradation of the backbone polymer at around 375°C. At 500°C the polymer is completely degraded. In accordance with this measurement, thermal debinding was performed to completion around 500°C. We also have SEM images in Figure 2.22 of the microstructure after debinding at several different temperatures where it is possible to observe the development of neck growth between the steel particles. The images also confirm that the entire polymer content was removed at temperatures above 500°C. At this step, conditions for obtaining near-total density are achieved by continuing to raise the temperature, but always below the melting point of the metal, as already mentioned. At some point of the heating process, atomic diffusion between metal powder particles begin to happen. Although clearly discernible sintering necks did not emerge until a temperature of 850°C the mechanical stability of the samples was already obtained at debinding temperatures of 750°C, where we can observe a slight onset of necking. At this temperature, the SEM image in Figure 2.22c indicates a reorganization of powder particles during the debinding step. This is a result of the elevated temperatures

during debinding that lead to movements and rotations of the particles within the softened binder matrix [1, 8].
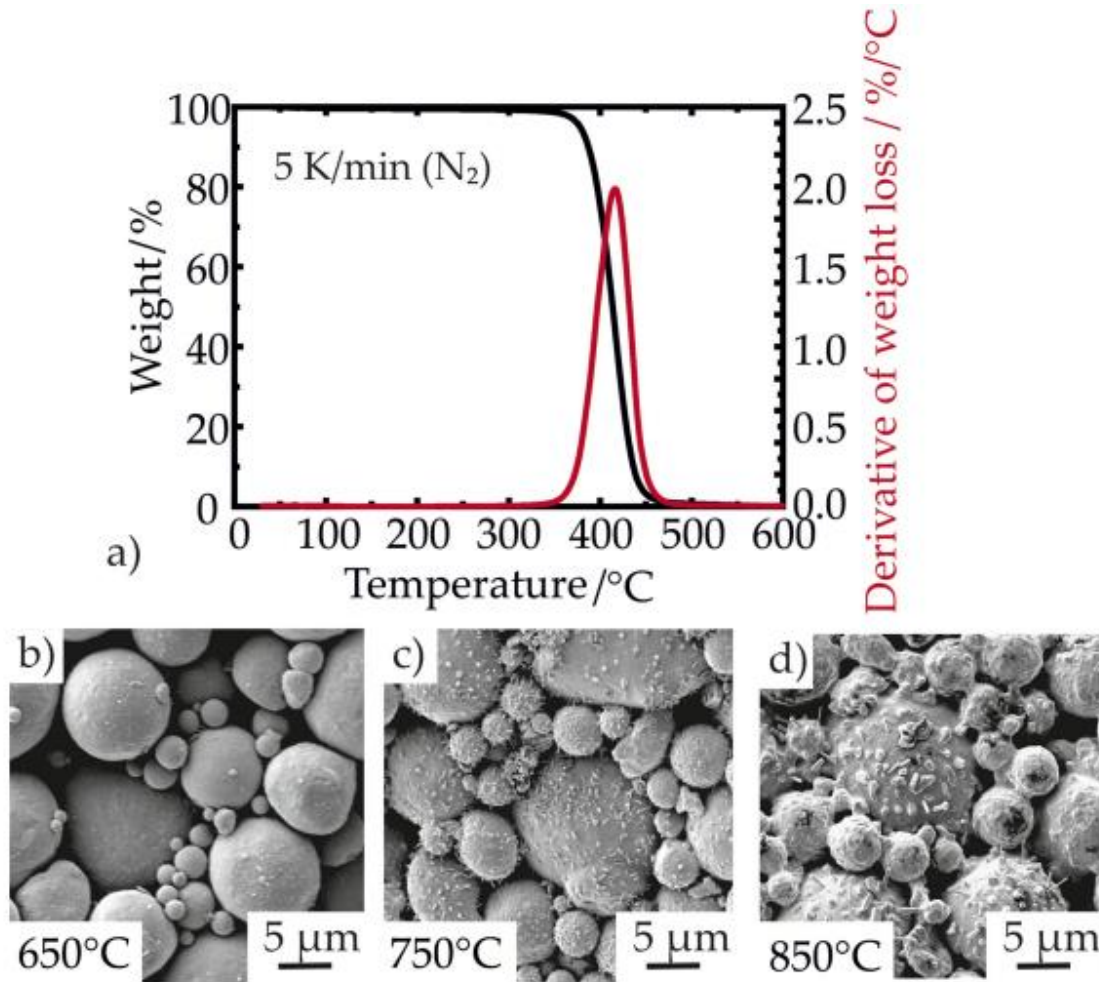
Figure 2.22 - (a) Thermogravimetric analysis of the backbone polymer and SEM images of the microstructure after thermal debinding at (b) 650 °C, (c) 750 °C and (d) 850 °C [1].

In the graph depicted in Figure 2.23a, the relation between different sintering temperatures and resulting porosity during thermal debinding for some specific parts made of 316L stainless steel is plotted. Measurements of the densities (by water immersion) for a specific sintering heating rate, which are represented by the black squares in Figure 2.23a, indicated that a higher sintering temperature leads to higher density of the samples. Consequently, a higher sintering temperature results in a lower amount of remaining porosity, which can also be observed in the SEM images in Figure 2.23b-e. Simultaneously, elevated temperatures results in increased grain growth, which adversely impacts the mechanical properties of the parts. In all the parts examined, the rate at which they were heated remained excessively high. Consequently, although the parts showed a reduction in defects, they still possessed internal ones that considerably impacted their density. These internal defects, induced by the internal pressures experienced during thermal debinding, are visible in the upper portion of Figure 2.23d. In the graph shown in Figure 2.23a, one can also see density/porosity measurements for parts sintered with a slightly lower heating rate, corresponding to the red values. But in this case, the sintering times were varied for each sample, while the sintering temperature was the same for all. Even though full density

is not attained due to the presence of tiny residual micro-porosities, it is possible to observe that densification was optimal after 120 min of sintering, which was the longest time evaluated in this test series. Longer sintering times lead to no further densification but higher grain sizes [1].
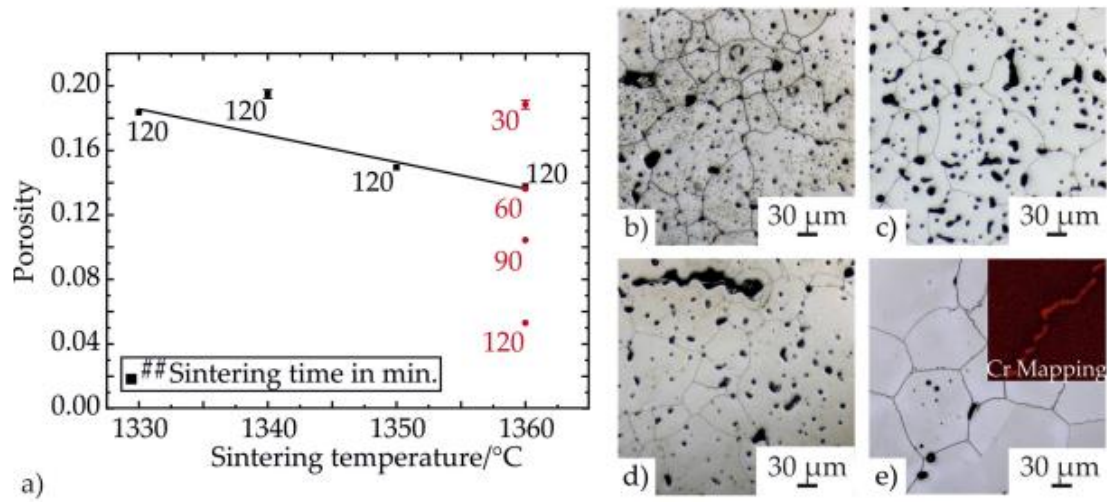
Figure 2.23 - a) Evaluation of porosity for different sintering temperatures and time. b)-e) Microstructures after sintering at different temperatures [1].

To conclude this subchapter, Table 2.2 summarizes the main advantages and disadvantages of the different debinding methods reviewed is presented:

Table 2.2 - Trade-off table for debinding methods [9].

Process	Advantages	Disadvantages
Thermal debinding	• Simple operation with common equipment. • No hazardous chemicals needed. • Low environmental impact beyond energy consumption. • Wide variety of environments possible. • Can be used in combination with other debinding processes as needed. • Minimal training required for use. • Only basic personal protective equipment (PPE) is required for users. • Works well for parts with high powder content.	• Slow process • Must have a clean and oxygen-free environment. • Less effective than solvent debinding for some binders. • May introduce stresses into the debinded parts due to thermal cycling. • Due to thermal stress on the parts, parts made by combining ceramic and metal powder are not possible;
Organic solvent debinding	• Relatively fast process. • Cleanliness and preparation of the parts is not as important as in thermal debinding; • Very flexible process and can process a wide variety of powders and binders. • Can process green parts that are made from both metal and ceramic powder. • No thermal cycling or stress introduction (in chemical phase).	• Very complex process that requires careful planning. • There is a risk of chemical reactions between the parts/binders and the solvent. • Extensive user training and PPE needed. • Some of the chemicals used are very hazardous to the user and environmentally hazardous. • Does not work well for high-powder green parts. • Usually requires a thermal degradation step before sintering due to residual binder. • Parts must be thoroughly and fully dried before sintering.
Catalytic debinding	• By far the fastest Debinding process used for PME. • Simpler to use than solvent debinding. • Can be used with parts made with a high powder density.	• The processing environment is sensitive to its setup. • The gasses used are potentially hazardous and environmentally dangerous. • Extensive training and PPE required. • Limited to only some materials and binders due to the oxidation and other chemical reaction risk of the material with the acid gas.

2.1.6. PART SHRINKAGE AND SCALING

During the sintering process, part shrinkage occurs as metal particles combine to form a solid mass. Anisotropic shrinkage is observed, with the Z axis generally experiencing slightly greater shrinkage than the X and Y axes due to the layer-by-layer printing approach and the effect of gravity. There may be other anisotropies due to heterogeneities in particle distribution and gaps between strands. To account for this, oversizing factors are applied to scale up parts during printing, ensuring they achieve the correct size after shrinkage [20].

The process of shrinkage is intricately influenced by several factors, including the composition and distribution of the binder and powder content. To ensure precise dimensions, it is imperative to calculate the appropriate shrinkage. This calculation demands empirical testing as real-world shrinkage values might differ from theoretical projections. Furthermore, the degree of shrinkage is significantly influenced by the effectiveness of both solvent/catalytic debinding, thermal debinding and sintering stages. Achieving a uniform mixture in the filament is crucial in attaining the most isotropic shrinkage possible and averting warping issues. It is noteworthy that, despite the considerable shrinkage that occurs, control of temperature and duration during the sintering process ensures the retention of the part's original geometrical features and overall shape [7].

By empirically obtaining shrinkage prediction values for a given material and set of conditions, it is also possible to obtain the values for the Oversizing Factor (OFS), which is the fraction by which the part needs to be scaled up in the computer slicer software to compensate for the shrinking effect [20, 14].

The shrinkage in each axis is calculated by the following equation:

$$Sh = 1 - \frac{Ls}{Lg}, \tag{1}$$

where Sh is the shrinkage fraction suffered by the specimen, Ls is the dimension of the sintered part and Lg the dimension of the green part. The value of the shrinkage relates to the OFS through the next equation:

$$OFS = \frac{1}{1 - Sh} = \frac{Lg}{Ls} \tag{2}$$

From this equation, one can also obtain Eq. (3), which directly provides the dimension that ought to be used in the CAD file to obtain a given nominal dimension in the final sintered part:

$$Lg = OFS \cdot Ls \tag{3}$$

However, it is important to note that inaccuracies may arise in the green part printing process due to slicing parameters and overall printer hardware performance. In such cases, adjusting the scaling values can help correct over and under-extruded green parts to achieve the desired size for the green parts [20].

2.2. FEEDSTOCK CHARACTERISTICS AND MATERIALS

The capacity of MFFF to process Fe, Cu, steel, Ti-Al-V, Ni-Ti, W-Cr, Mg-Al-Zn, and hard metals has been demonstrated in several investigations. Any material that can be sintered can generally be used with this process. This demonstrates the outstanding capability of MFFF to create a variety of structural and functional materials. The most often studied class of materials in MFFF is steel, especially stainless steels [3, 1].

Changes in powder composition affects the features of the green and finished products, as well as the shrinkage values. Two important aspects, particle size and powder production method, are extensively researched by scientists. The densification behaviour of printed components during sintering is significantly influenced by particle sizes. Because there are more surface areas in a given volume, the densification for the sample comprised of smaller particles can happen at a comparatively lower temperature, speeding up the sintering. Smaller particle size also reduces feed supply viscosity and solid volume content. An excellent method for producing high-quality, small, spherical particles is gas atomization. The qualities of the printed item are improved by using a powder with small particle size and a great spherical form, but the price of the powder is significantly raised as a result [8, 21].

However, the binder system is of equal or even greater importance when producing high powder content feedstocks. Designing binder systems for MFFF is a challenging task that requires careful consideration of the elements and their various fractions. The structure of pieces made of powder is formed and maintained by the binder, a multi-material component. A thorough understanding of how these elements affect these processes is required to optimize the binder composition, because the characteristics of the feedstock and the debinding processes directly impact the properties of the final components. It is crucial to balance trade-offs and take numerous factors into account. Additionally, it is important to comprehend the impact of each constituent substance and how they interact. The choice of constitutive polymers must satisfy criteria including rheology, melting temperature, and chemical compatibility [3, 8].

To satisfy all the demands put forward by the printing, solvent debinding, and heat debinding steps of MFFF, the binder system must be properly developed. The rheological characteristics of highly loaded filaments provide one of the main difficulties in the 3D printing process. The viscosity increases by orders of magnitude because of the large solid loading, and a yield stress behaviour may be seen. For the material to flow through the printer nozzle, high stresses must be applied. This may cause the filament to buckle under the heavy compressive pressure or abrade at the areas where it comes into contact with the extruder gears. The extruder gears' tensions cause the filament and the material to be sheared off to yield locally. The binder must provide the filaments enough strength and stiffness to prevent these printing errors. The filaments must also be flexible enough to allow handling and spooling without breaking. To guarantee low pressures on the filament during printing, the binder viscosity at the printing temperature should also be carefully regulated. The solvent and heat debinding processes are also influenced by the filament composition. When optimized, it facilitates the removal of the binder without the occurrence of defects like cracks, distortions, or blisters [3].

Studies (some included in Table 2.3) have demonstrated that binder systems using TPE components and polyolefins—either as the soluble binder or as the backbone—could be used successfully for MFFF of stainless steels, such as 17-4 PH. This is true even though

the precise feedstock composition and polymers used in a lot of the existing literature were kept secret. The most popular surfactant utilized in feedstocks for powder injection molding and AM based on binder extrusion is stearic acid (SA). Surfactants are chemical substances that reduce the surface tension or interfacial tension between two liquids, a liquid and a gas, or a liquid and a solid. The hydrophilic surface of metal particles makes it difficult for other organic binders to distribute evenly on the powder surface. Therefore, the surfactant is necessary to enhance the powder's capacity to wet. In general, it can act as: a lubricant to reduce friction forces between powder particles, thereby reducing feedstock viscosity and increasing solid loading; a plasticizer to enhance mixing capabilities between binder components; and a dispersant to facilitate easier powder particle dispersion in the binder and increase feedstock homogeneity. One essential quality is the homogeneity of powder dispersion in feedstock and filament. The mechanical characteristics and density of printed items are influenced by this attribute. The uniform distribution of powder in the feedstock has an impact on the rheological behaviour of the material and can help retain forms throughout posttreatment. More importantly, the surfactant has the ability to significantly increase the adhesion strength between the powder and the binder, hence increasing the strength of green components and providing a potential means of eradicating structural flaws. As a result, the surfactant has a significant impact on regulating the quality of finished goods. It has been demonstrated that the ideal SA percentage for the binder system is 5% [22, 3, 8].

When selecting the ideal proportion of a TPE in the binder, attention must be taken to strike a balance between stiffness and strength on one hand and flexibility on the other. A binder system consisting of a very high fraction of TPE results in very flexible filaments of low stiffness and strength. These filaments can display abrasive failure at the contact areas with the extruder gears and cannot be extruded. Buckling or abrasive failure is moved to higher loads by raising the strength and stiffness of filaments, that is, by reducing the quantity of the elastomer material in comparison to the other polymers in the binder, leading to greater attainable extrusion pressures and enhanced printability. The filament printability is defined as the ability of a filament to be extruded by the 3D printer without showing abrasive damage at the contact point between extruder gears and filament. Therefore, enhanced printability pushes back extrusion failure to bigger flow rates and smaller nozzle sizes. However, flexibility suffers as a result. The filaments become exceedingly brittle and impossible to handle or spool if the elastomer percentage is too low. For a low elastomer content, no continuous phase of flexible polymer exists through the binder matrix. So, the binder polymer with significantly lower flexibility has a dominating influence and the failure strain drops significantly [3].

The yield stress, which needs to be applied to break the interlocking particle network and induce flow to the material, decreases with decreasing elastomer content. With decreasing matrix viscosity, the stress transmitted by the matrix decreases. As a result, the particle network breaks at lower stresses. In MFFF the yield stress of the material plays an important role in three respects. First, during 3D printing the flow conditions are highly transient and the flow-initiating events, in which the yield stress needs to be overcome, are frequent. The filament is retracted at the end of print lines, or extrusion is paused between layers. Second, a yield stress prevents deformation of deposited material before solidification of the polymer matrix. Feedstocks with high solid loading exhibit high densities and thermal conductivity which makes the material more prone to deformation after deposition due to gravitational forces and remelting of the polymer matrix. And third, during thermal debinding a yield stress in the compound is imperative, such that the shape

is preserved. However, this yield stress is different since a part of the binder is already removed by solvent extraction [3].

Even though a backbone polymer is usually required, it is preferred to have as little of it as possible in the compound following debinding. On one hand, this helps with thermal debinding. As gaseous species of the thermal decomposition can escape through the network of open holes created during solvent debinding, the danger of scorching and deformation during thermal debinding is decreased. Additionally, backbone residue impurities can be reduced. On the other hand, as the polymer network supporting the stresses from swelling and gravity becomes smaller, low backbone fractions raise the likelihood of distortion or cracking defects during solvent debinding [3].

The information presented above leads to the conclusion that there is not a single set of optimum feedstock characteristics, but rather a range of viscosity, mechanical strength, stiffness, and flexibility combinations that permit successful handling, printing, and debinding. It is crucial to remember that these combinations rely on the type of material used, the 3D printer's extruder design, the size and morphology of the powder particles, wettability, and other factors. After having a binder system established, its melting and degradation temperature points are two critical parameters that influence printing and debinding circumstances [3, 8].

Some binder formulations for stainless steel filaments (namely for 316-L and 17-4 PH) available in the literature are shown below in Table 2.3. It is noteworthy that a lot of the studied filaments consisted of the same powder loading and similar binder system.

Table 2.3 - Examples of filament compositions used in material extrusion additive manufacturing for production of 17-4 PH and 316L SS parts.

Metal	Particle Size* (µm)	Solid Loading (vol%)	Binder System	Ref.
17-4 PH / 316L	D50 12.3 / D50 15.1	55	Thermoplastic elastomer / Grafted polyolefin	[23]
17-4 PH	D50 12.3	55	Thermoplastic elastomer / Grafted polyolefin	[24]
316L	D50 5.5	55	Thermoplastic elastomer / Grafted polyolefin	[25]
17-4 PH	D50 28	64	Polyolefin / Thermoplastic	[10]
17-4 PH	-	-	Thermoplastic elastomer / Grafted polyolefin / Stearic acid	[26]
316L	D50 6.05	55	Thermoplastic elastomer / Grafted polyolefin / Stearic acid	[27]
316L	D50 7	-	Nylon	[28]
316L	D50 6.05	55	Elastomer, Polyolefin and Dispersant	[29]
316L	Avg. 10	60	Polyoxymethylene and Paraffin Wax	[30]
316L	30-50	88 (wt.%)	Polyoxymethylene (POM), Polypropylene (PP), dioctyl phthalate (DOP), dibutyl phthalate (DBP), and zinc oxide (ZnO)	[31]

*D50, in particle size distribution measurements, is the mass-median-diameter, considered to be the average particle size by mass.

2.3. MORPHOLOGY AND PROPERTIES OF MFFF PRINTED PARTS

In Figure 2.24, we can observe the microstructure of a 316L part, showcasing the uniform grain size distribution typically seen in MFFF printed parts. A closer look at the microstructure in Figure 2.24 (on the right) reveals the presence of some larger pores. These pores are more prominent near the surface of the printed parts, primarily due to the lower forming pressure applied during the printing of the uppermost layer. In contrast, the lower layers experience compaction during the printing process, caused by the weight of subsequent layers [5].
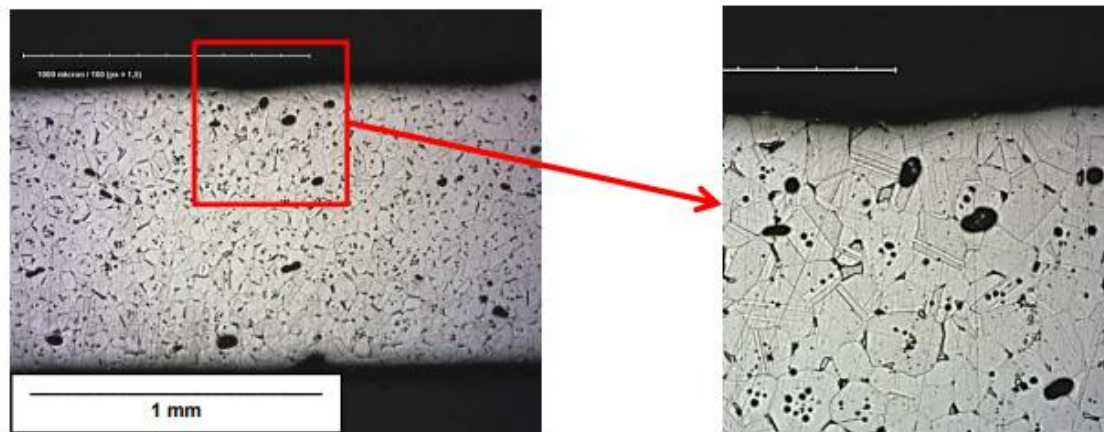
Figure 2.24 - Microstructure of MFFF printed 316L sintered part [5].

Another prevalent characteristic observed in parts produced through this process are the pronounced printing lines visible on the surface of the green parts, such as the lines presented in the specimens shown in Figure 2.3. These lines persist even after the sintering process, resulting in a high surface roughness with a consistent pattern. Figure 2.25 shows the images of a cross-section through the uppermost print layer of the sintered part to examine these lines further [5].
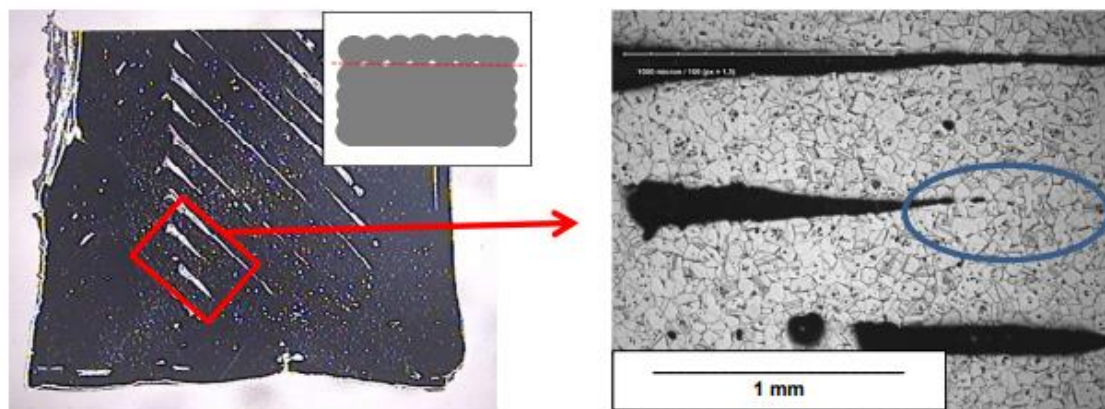
Figure 2.25 - Cross section through the upper layer of the 3D-printed and sintered part of 316L [5].

In certain regions, it is evident that the printing lines on the uppermost layer of the sample do not contact each other, leading to a well-structured open porosity. However, during the printing process of a multi-layered sample, these gaps are subsequently filled with material from the layer above, resulting in a low porosity structure at the core of the sample. Notably, in the contact areas of the printing lines (indicated by the blue circle in Figure 2.25 on the right), a pore-free and fine-grained microstructure can be achieved. Therefore, optimizing the printing parameters for the top layer, such as reducing the distance between the printing lines or inducing an overlap between them, is expected to mitigate this effect [5].

In a different study, the fractured surface of some 17-4 PH samples showed the presence of two types of defects, but this time in the mesostructure, that is, in the core of the part: the presence of inclusions (Figure 2.26 on the right) and, again, pores between the raster (Figure 2.26 on the left). The inclusions were observed on the raster's surface too (Figure 2.27). This is a prevalent occurrence in MFFF parts, primarily due to the challenging nature of completely removing all binder residues [32].
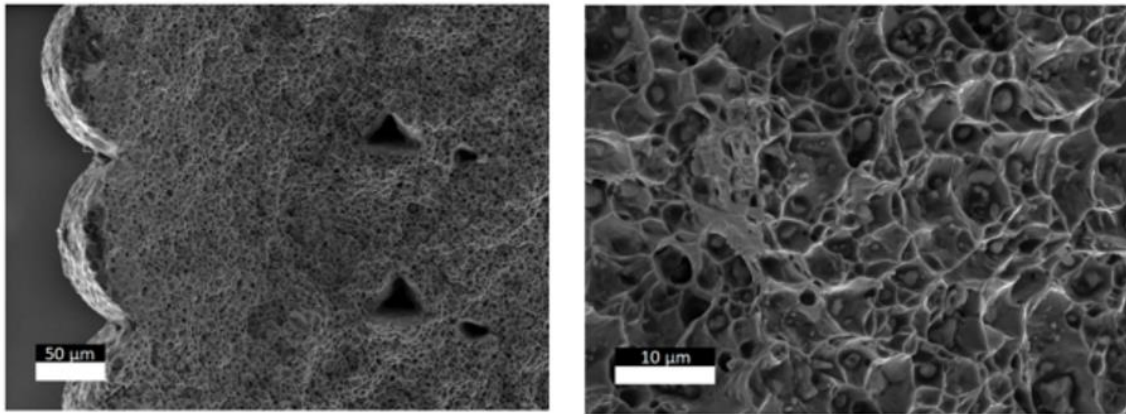
Figure 2.26 - Defects observed in the cross section of a sample of 17-4 PH: porosity between the raster (left) and details of particle inclusions (right) [32].

The existence of these defects significantly impacts the mechanical properties of the final product. Therefore, it becomes imperative to thoroughly optimize all the parameters involved in the printing, debinding, and sintering processes to minimize these defects successfully. Achieving such optimization will lead to enhanced mechanical performance and overall quality of the fabricated parts [32].
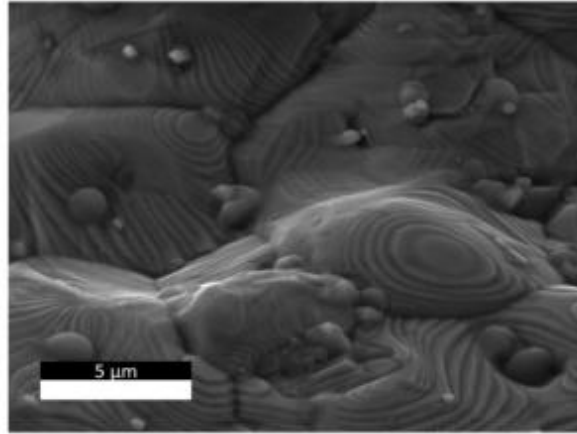
Figure 2.27 - Inclusions observed on the raster's surface of a sample printed with 17-4 PH [32].

2.3.1. MECHANICAL PROPERTIES

MFFF has emerged as an accessible and cost-effective alternative to traditional AM techniques for fabricating metal samples. While its ease and safety are advantageous, ensuring robust mechanical performance is equally critical to compete with other established processes. In Table 2.4, we present an overview of mechanical properties obtained from various studies on 17-4 PH processed through MFFF and standard metal AM techniques, without any thermal post-processing applied. For comparison purposes, mechanical properties achieved using MIM are also included, because parts made by this technique also go through the debinding and sintering processes.

Table 2.4 - Mechanical properties for 316L and 17-4 PH processed by different technologies, including MFFF.

Technique	Yield Strength (MPa)	Tensile Strength (MPa)	Elastic Modulus (GPa)	Strain at Break (%)	Reference
MFFF (upright)	839.47	942.56	204.66	-	[32]
MFFF (flat)	900	1161	160	5.9	[10]
MFFF (flat)	688	1068	138	5.0	[33]
MFFF (flat)	590	795	130	3.0	[34]
MFFF (upright)	647	701	134	0.8	
MFFF (flat)	747	1034	176	4.9	[35]
MFFF (upright)	668	745	156	0.8	
MFFF (flat)*	680	760	-	4.0	[51]
DMLS (flat)	860	886		19.9	[37]
DMLS (upright)	861	924	-	20.1	
EBM (flat)	850	1020	180	16.6	[38]
EBM (upright)	835	975	178	15.2	
SLM	634-666	1104-1106	-	20.5-21.3	[39]
SLM	472	958	-	26.0	[40]
SLM	535	1029	-	18.0	[41]
MIM	730	896	190	6.0	[42]
MIM	740	900	190	6.0	[43]
MIM	650 – 750	800 – 950	-	>6.0	[44]

*These values were taken from a technical datasheet provided by *BASF*, which is the manufacturer of the material used in this investigation. This datasheet is included in Appendix A: Ultrafuse 17-4 PH Technical Datasheet.
SLM: Selective Laser Melting
EBM: Electron Beam Melting
DMLS: Direct Metal Laser Melting

Through this brief review, one can gain some insight into the comparative performance of MFFF in relation to other manufacturing methods, revealing its potential as a promising approach for producing high-quality metal parts. Evidently, among the studies considered, MFFF demonstrated superior tensile properties, even though the strain at failure was comparatively lower than in other processes. Despite its status as a relatively recent and developing technology, and the inherent challenges it may pose, MFFF has shown the capability to yield parts with acceptable mechanical properties.

Additionally, it is important to note that, as one might expect, MFFF-printed samples in an upright position tend to exhibit lower tensile properties. This is because the loading direction is perpendicular to the layer plane, often resulting in fractures primarily caused by delamination. This behaviour is commonly observed in layered media, as seen in fibre-reinforced composites and FFF plastic components.

2.4. BENEFITS OF MFFF AND COMPARISON WITH PBF PROCESSES

Several factors, including the cost of raw materials and equipment, safety issues, sustainability, material handling and performance, among others, determine which AM technique is best for a given application (whether it be for prototyping or for end-use). Each AM approach has benefits and drawbacks. PBF is the most popular additive manufacturing method for metals, as seen in Figure 2.28. So, it becomes vital to contrast MFFF with PBF

techniques in order to comprehend its advantages. These processes, such as Selective Laser Melting (SLM) or Electron Beam Melting (EBM) use a spreading mechanism to spread the layer of metal powder on top of each other and focused laser or electron beam is used as an energy source to melt and fuse the material powder together; thus, subsequent layers are fused and a 3D object is created [10, 7].
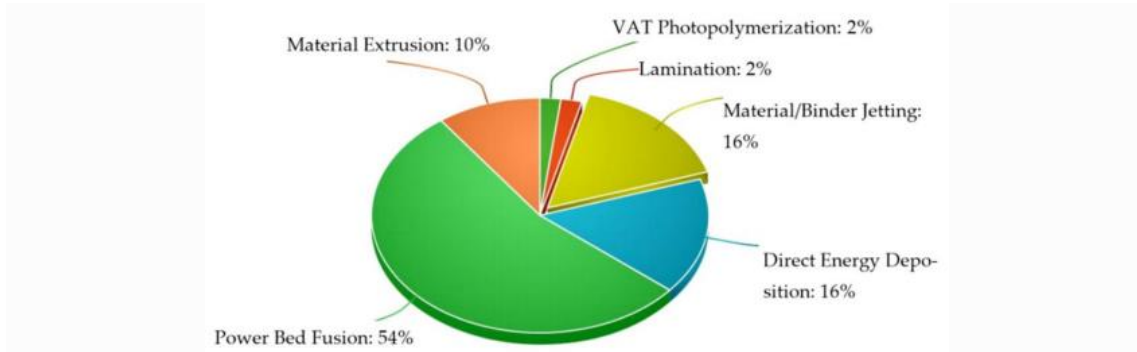
Figure 2.28 - Metal AM Market in 2020 [8].

In terms of capital cost of PBF machines, the TruPrint 1000 LMF by Trumpf, an entry level industrial 3D printer based on laser metal fusion technology (compatible with SLM), costs between $170,000 and $300,000 with build chambers of 100 mm × 100 mm × 100 mm. The M100, an entry level Direct Metal Laser Sintering (DMLS) machine by EOS with the build volume of 100 × 95 mm comes at a price of $350,000 without any add-ons. Due to the additional costs associated with post-processing equipment like shot penning setups, furnaces, etc., the cost of a 3D printer is only a small portion of the entire cost needed for a working setup. The necessary post-processing depends on the techniques utilized and the desired output. To attain dimensional accuracy, CNC machining is desirable in particular circumstances. The cost of powder itself can range from $80 to $120 per kilogram for AlSi10Mg or stainless steel 316L and from $300 to $600 for Ti–6Al–4V [7].

Desktop Metal and *Markforged* offer commercially available setups based on the MFFF process. The Desktop Metal Studio System costs approximately $120,000 and *Markforged Metal X System* comes at $99,500. Both these companies offer a complete setup including printer, debinding setup, sintering furnace and controlling software. The prices, which include the hardware for the post-printing processes, are more affordable compared to the cost of commercially available PBF machines. Besides, various manufacturers (such as *BASF*, *The Virtual Foundry*, *Zetamix by Nanoe*) provide filaments consisting of metal powder and binders, which can be used with any FFF 3D printer, even a small non-industrial desktop printer. These printers can be as cheap as $1000 [10]. For debinding and sintering, cycle details are provided by manufacturers and any suitable furnace can be used. Cost of metal filled filament for MFFF is between $120 and $220 for AlSi10Mg and also for 316L and 17-4 PH stainless steels. *The Virtual Foundry & Nanoe* also sell the compatible furnace separately while *BASF* provides sintering service through their partnered distributors. A further advantage of the process is that the green parts can easily be polished directly after printing, which can reduce postprocessing costs and make the process overall even more simple. Taking all this into consideration, MFFF appears as a cost-effective solution for metal AM, compared to PBF processes [10, 7].

One of the limitations with PBF is the reusability of powder. Since it is required to completely fill the build volume with layers of metal powder, it will require much more

capacity of powder than the part volume. After building a part, there's still unused metal powder remaining on the bed; some particles out of this remaining metal powder have contact with the laser and are no longer good for use. These particles are known as splatters and need to be removed by sieving. Unused powder suffers partial sintering with each AM build due to latent heat from the melt-pool; as a result, there is subsequent change in powder size distribution. This leads to creation of non-spherical particles resulting in porosity and rough surfaces in the part manufactured. So, recycled powder should not be reused as it affects the quality of parts produced, whereas in hybrid FFF there is no such wastage of metal powder as we are using it in filament form. Also, in PBF processes usually the operator must deal with metal powder typically microscopic in size (< 100 µm), which is generally toxic and can cause serious health issues due to inhalation or ingestion. Also, there are several other challenges associated with small particle powder handling. As particle size decreases, interparticle friction and electrostatic forces increase. These can result in a situation where powder loses its flowability. When the surface area to volume ratio of a particle increases, its surface energy increases and becomes more reactive. For certain materials, this means that the powder becomes explosive in the presence of oxygen; or it will burn if there is a spark. Besides, when handled, small particles tend to become airborne and float as a cloud of particles. In PBF machines, airborne particles will settle on surrounding surfaces, which may cloud optics, reduce the sensitivity of sensors, deflect laser beams, and damage moving parts [45, 8, 7].

In the MFFF process, if the user is directly purchasing the composite filament, all these problems and risks can be managed, provided that filaments were manufactured in a controlled environment. Not only that, but a much easier change in material in between each operation is made possible. In addition, PBF processes involve hazardous and expensive energy sources such as lasers and electron beam. Thus, MFFF can be considered as a relatively sustainable option [5, 7].

Summing up, although SLM is currently well-established for industrial applications, it comes at a significant expense in terms of equipment. MFFF and even other extrusion-based variants present an alternative that can be relatively low cost and straightforward to operate, with the capacity to manufacture complicated geometrical components [8].

It is, however, essential to point out that the manufacture of parts with acceptable characteristics can still be a significant challenge in this emerging technique. Even when all the parameters are optimized, it is not possible to obtain fully dense parts (parts with 100% relative density). Given the inherent characteristics of the process, it is inevitable that a certain degree of porosities will arise, which will affect the properties of the parts and, consequently, their performance. Overall, MFFF still produces parts with low geometrical precision and poor surface quality compared to other AM techniques such as SLM. Moreover, the geometry of the objects can vary and may even include small overhangs or internal cavities. Figure 2.29 shows a part fabricated by MFFF after parameter optimization. In this part, there are still visible minor printing artefacts such as layer lines and filament stringing, that remain on the part even after sintering. However, they could be eliminated by using a professional grade FFF printer with better motion control [5, 1, 46].
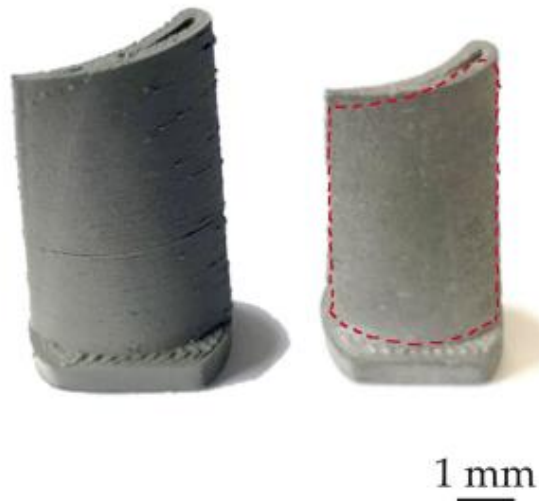
Figure 2.29 - 316L SS speciment before and after sintering showing layer lines and stringing [1].

2.5. CORROSION AND CORROSION TESTING PRINCIPLES

In the realm of mechanical engineering, corrosion may be occasionally overlooked, leading to a potential lack of understanding about this crucial facet of metallurgical science. Consequently, this section aims to provide a concise introduction to the basics of corrosion and corrosion testing. By exploring these aspects, it is possible to strengthen our understanding of this material degradation process to better comprehend the contents of following sections of this investigation.

2.5.1. CORROSION PRINCIPLES

Corrosion is the deterioration of materials caused by their surrounding environment. All types of materials, including metals, polymers, and wood, can be affected by corrosion. The most desirable materials are those that have a low corrosion rate, providing many years of reliable service before succumbing to corrosion-related failures. Metal corrosion is a complex process involving chemical reactions that transform metal atoms into metal ions and the transfer of valence electrons to electrochemically active ions and molecules in the environment. This electrochemical corrosion process is responsible for metal degradation. The rate of corrosion is influenced by thermodynamics, which determines if a metal will corrode in a specific environment, and kinetics, which determines how quickly the corrosion will occur. For instance, gold corrodes but at such a slow rate that gold leaf on structures can last a long time. On the other hand, low-carbon steel corrodes rapidly in hydrochloric acid, making it unsuitable for long-term use in such environments. Therefore, the corrosion rate significantly impacts the service lifetime of metals [47].

Metallic corrosion arises when metal atoms undergo oxidation and exit the metal lattice in the form of ions. The oxidation process of the metal is known as the anodic half reaction, and the regions on the metal surface where this occurs are referred to as anodes. On the other hand, the reduction of electrochemically active species in the electrolyte is termed the cathodic half reaction, and the areas where reduction happens are called

cathodes. Anodes and cathodes can exist at distinct locations, if negative and positive ions move in the electrolyte toward the anodes and cathodes, respectively, to preserve the electrical charge balance of the metal and electrolyte. Both anodic and cathodic reactions are essential to initiate and maintain metallic corrosion. For example, the corrosion of iron – the main component of steel – is represented by the anodic electrochemical equation [47]:

$$Fe^0 \rightarrow Fe^{2+} + 2e^- \tag{4}$$

This is referred to as an anodic half reaction because free electrons are produced. A cathodic half reaction must also be written to account for the reduction of electrochemically active species with the electrons generated in the anodic half reaction. An example of a cathodic half reaction is the reduction of hydrogen ions:

$$2H^+ + 2e^- \rightarrow H_2 \tag{5}$$
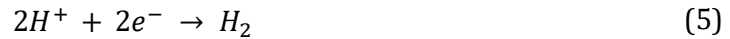
The overall corrosion reaction is a combination of the anodic and cathodic half reactions:

$$Fe^0 + 2H^+ \rightarrow Fe^{2+} + H_2 \tag{6}$$

Eq. (6) shows that iron atoms are oxidized to iron ions, producing electrons that reduce hydrogen ions in the metal's environment (that is, the electrolyte) at the metal surface, forming hydrogen molecules [47].

There is a long list of electrochemically active species that cause steel and a plethora of other materials to corrode. Oxygen dissolved in water and water itself are among these and are some of the most corrosive agents for parts and objects in our daily lives [47].

A way of knowing if a certain metal will suffer corrosion in its environment (usually considered the electrolyte) is by measuring the electrical potential between a test electrode of that metal and a reference electrode (hydrogen reference electrode) or a pseudo-reference electrode made from a metal that is corrosion resistant to the electrolyte. This potential difference between both electrodes is measured with an external electrometer, as shown in Figure 2.30. Electrode potential measured in the absence of applied potential is referred to as either Open Circuit Potential (OCP) or simply Corrosion Potential ($Ecorr$). OCP is essentially the voltage or electrical potential that develops spontaneously on the metal surface due to the electrochemical reactions taking place between the metal and the surrounding corrosive medium [47].
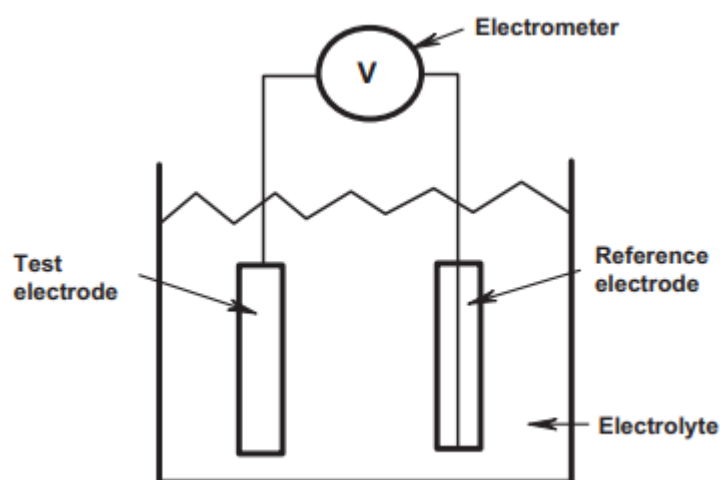
Figure 2.30 - Schematic for measuring electrode potential (differences) [47].

The OCP value indicates the tendency of the metal to corrode in the given environment. If the OCP is more positive (higher voltage), it suggests a higher corrosion resistance, as the metal is less likely to corrode. On the other hand, if the OCP is more negative (lower voltage), it indicates a lower corrosion resistance, and the metal is more prone to corrosion. More specifically, if an OCP value is negative, spontaneous corrosion is expected. For example, iron is expected to spontaneously corrode in acids because its OCP is negative However, a different electrolyte could produce a positive OCP for iron and thus spontaneous corrosion would not be expected [47].

It is important to emphasize that OCP magnitudes are determined by the chemical composition of the considered metal and the environment surrounding it. In other words, OCP magnitudes are not intrinsic properties of a metal and they change when the electrolyte's composition changes. The OCP magnitude is determined by:

- the type of metal.
- the surface condition of the metal.
- the type of reference electrode used to measure the potential.
- the chemical composition of the environment [47].

In corrosion testing, measuring the OCP is an essential step to understand the corrosion behaviour of a material or metal surface in a specific environment and to predict its susceptibility to corrosion. However, the metal OCP for a given environment does not tell us how fast the corrosion will proceed when spontaneous corrosion is predicted [47].

Corrosion kinetics determine the lifetime of structures fabricated from metals and metal alloys. Electron transfer from the metal to electrochemically active species in the environment enables the estimation of corrosion rates using precise electronic devices [47].

Corrosion rate is directly related to corrosion current density. By applying a potential from an external power supply, it is possible to establish a connection between electrical current and these alterations in metal potential through the Butler-Volmer equation. While we won't delve into the equation and its components here, it produces a curve similar to the one shown below in Figure 2.31 [47].
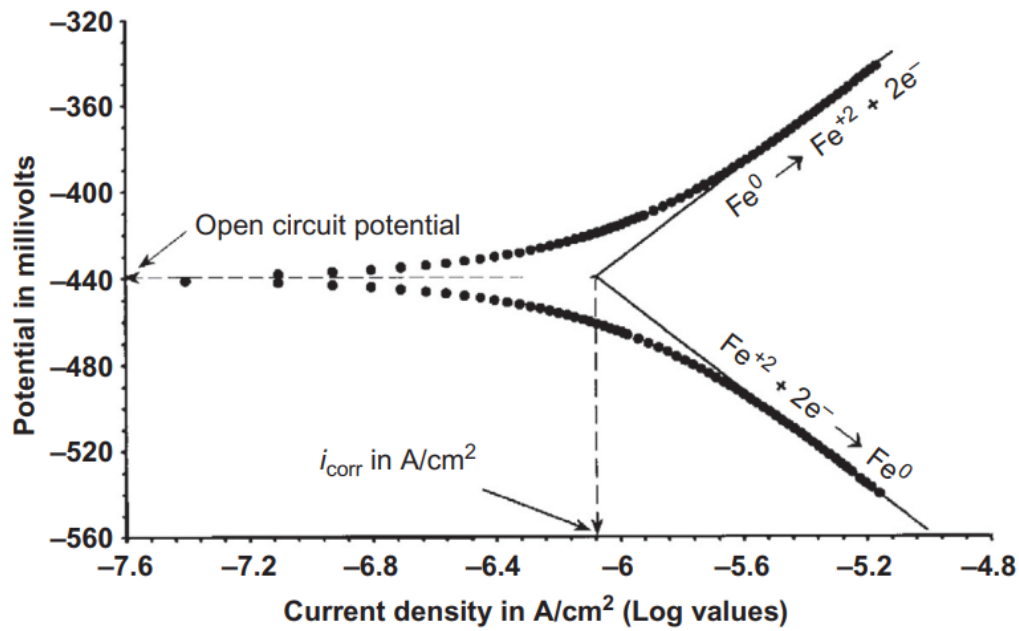
Figure 2.31 - A Butler Volmer current potential curve [47].

This curve can also be obtained empirically, as we will see in the next supchapter, by applying a positive or negative voltage to a test electrode in an electrochemical corrosion test cell, which makes an external current arise, as predicted by the Butler-Volmer equation. As illustrated in Figure 2.31, the potential current curve for iron generated by the mentioned equation exemplifies this behaviour with distinct anodic and cathodic branches. In the anodic branch, iron undergoes oxidation, while in the cathodic branch, it undergoes reduction [47].

It should be noted that the point of inflection on the PDS curves corresponds to the OCP and it represents the potential where no external current flows to or from the electrode, that is, there is no net current on the electrode. By extrapolating linear segments of the anodic and cathodic branches to the OCP, as depicted by the solid lines, the corrosion current density (*Icorr*) can be estimated. These straight lines, characterized by their slopes (mV/decade, in most cases), are called Tafel plots and are extremely useful for analysing PDS curves. The diagram that depicts only these extrapolated lines is known as Evans diagram, after U. R. Evans, who first proposed this simplification. By overlapping these extrapolated lines from different electrochemical active species, we can simulate steady-state corrosion reactions between such species, such as the one involving iron in an acidic environment. In Figure 2.32, the Evans diagrams for both hydrogen and iron are overlaid, representing the overall corrosion reaction for iron in acid (Eq. (6)). The corrosion current densities for hydrogen and iron are indicated on the current axis, and the respective electrochemical half reactions are placed along each branch [47].
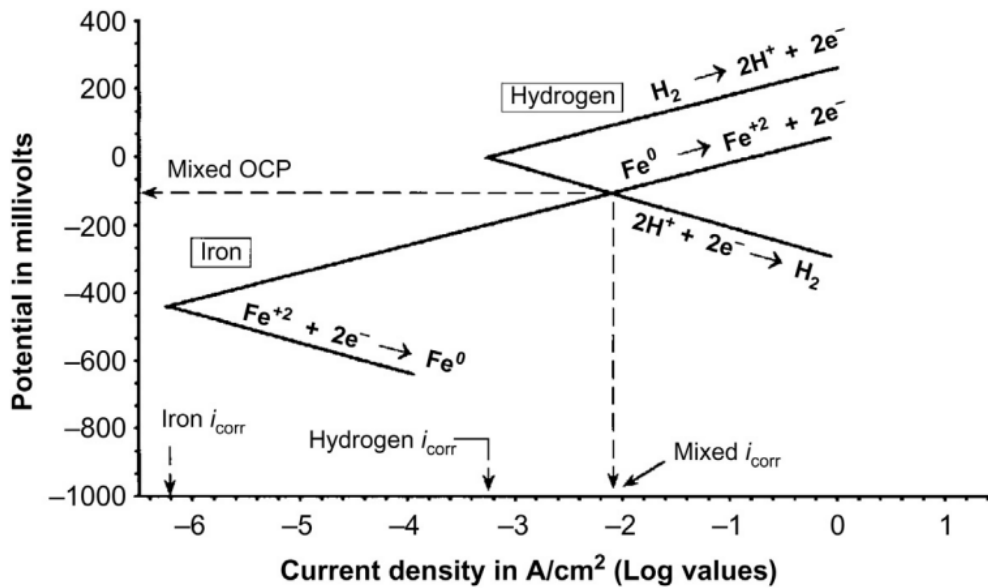
Figure 2.32 - Evans diagram for corrosion of iron in an acid electrolyte [47].

Furthermore, it is worth noting that the corrosion current resulting from the combined reaction is higher compared to the individual reactions. In other words, the presence of hydrogen ions accelerates the corrosion of iron, leading to a higher corrosion rate (higher *Icorr*) compared to the case without hydrogen ions [47].

2.5.2. CORROSION TESTING

The corrosion rate of a metal or metal alloy is influenced by three main factors: the metal's composition, the surface treatment it undergoes (such as grit blasting or polymer coating), and the chemical composition of the surrounding environment. There are several common electrochemical corrosion measurement techniques used to estimate metal and metal alloy corrosion rates and overall corrosion performance. Each approach has its own strengths and weaknesses, and the most appropriate method may vary depending on the specific application. In some cases, a combination of different methods may be necessary to address particular situations effectively. For the purposes of this work, subsequently, we are briefly reviewing a method called Potentiodynamic Polarization (or Anodic Polarization, depending on the authors) [47].

Figure 2.33 contains an example of a potentiodynamic scanning (PDS) curve, or potentiodynamic polarization curve, which are the type of curves obtained with the referred testing method. A PDS curve has several additional quantities in its anodic branch, compared to the current-potential curve previously displayed:

1. The primary passivation potential, Epp, is the potential after which current either decreases or becomes essentially constant over a finite potential range (this potential is also sometimes referred to as the anodic nose).
2. The breakdown potential, Eb, is the potential where current increases with increasing potential.
3. The passive region is the portion of the curve between Epp and Eb.

4. The portion of the PDS curve where potentials are less (more negative) than Epp is referred to as the active region of the curve.
5. The portion of the curve where potentials are greater (more positive) than Eb is referred to as the transpassive region of the curve [47].

Parameters such as Epp, Eb, and the width of the passive region serve as indicators for characterizing corrosion behaviour and assessing the protective effectiveness of a passive film on a metal against corrosion. The active region typically experiences general corrosion, and occasionally pitting corrosion, while the passive region usually shows minimal to no corrosion activity. The transpassive region represents the region where processes like pitting corrosion occur, due to the presence of localized damage to the passive film at discrete locations on the metal surface [47].
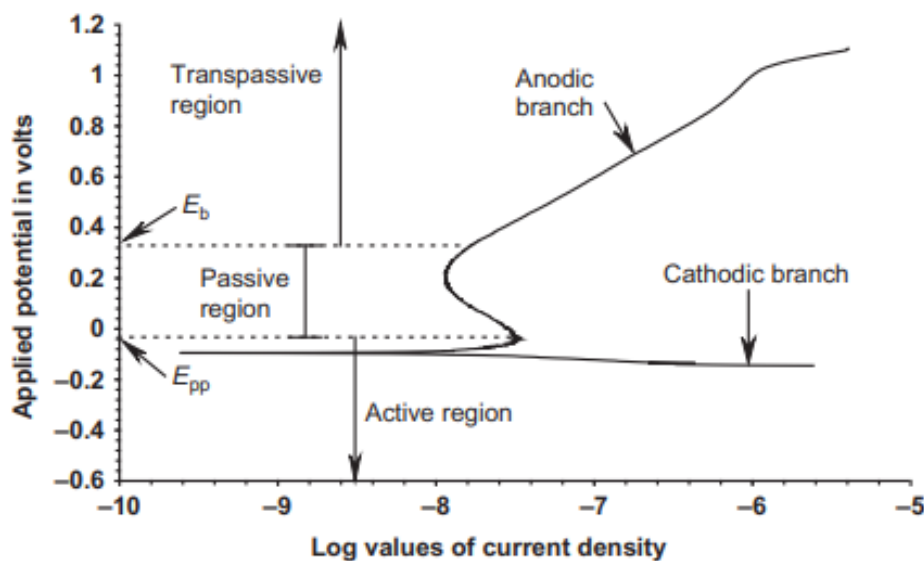
Figure 2.33 - PDS curve for passive corrosion behaviour [47].

Figure 2.34 illustrates a typical electrochemical corrosion test setup, normally used to obtain the PDS curves, comprising three electrodes within a test cell connected to a potentiostat. The potentiostat supplies electrical current to alter the test electrode potential from its OCP to a value dictated by the potentiostat current. This process is referred to as polarization, where the electrode potential deviates from its OCP. The resulting current is a consequence of the imposed overpotential on the test electrode and is withdrawn from the test electrode and supplied to the counter electrode, (and vice versa, depending on whether we're studying the anodic or cathodic branch) maintaining equipment and electrode electrical neutrality [47].
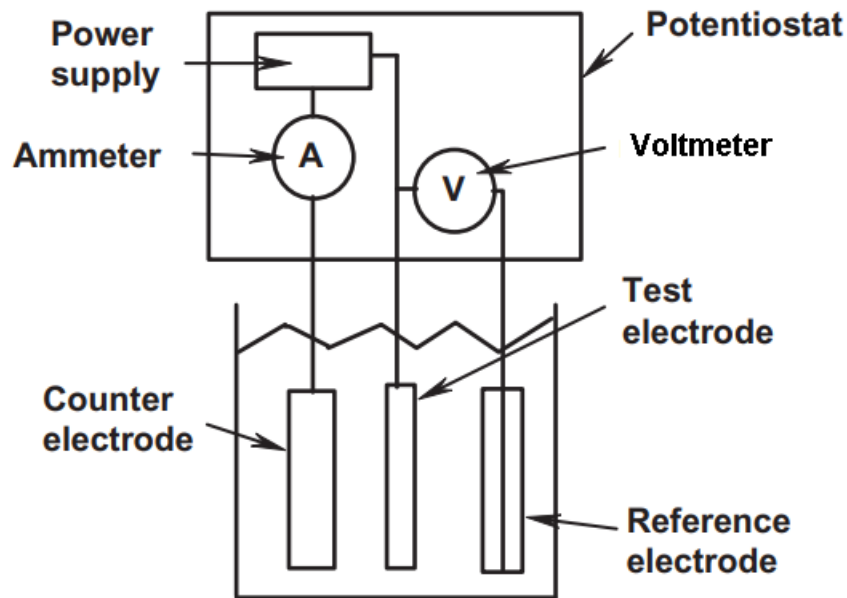
Figure 2.34 - Diagram for a three-electrode test cell [47].

The polarization of the test electrode is assessed by measuring the potential difference between the reference and test electrodes. The reference electrode remains at its OCP and serves as a reference point for corrosion measurements, as no electrical current flows between the potentiostat and the reference electrode. Moreover, the reference electrode provides feedback to the potentiostat, allowing monitoring and adjustment of the test electrode potential to a desired level. In electrochemical testing, a potentiostat applies a voltage or a range of voltages to create an imbalance between the number of anodic and cathodic sites, prompting electron flow in an effort to restore charge neutrality. The electrons flowing to or from the electrode are electronically quantified at each applied voltage level, resulting in a comprehensive dataset comprising various voltages and their corresponding electrical currents [47].

2.5.3. CORROSION PERFORMANCE OF 17-4 PH PARTS

In this section, analogous to Section 2.3.1, where the tensile properties of 17-4 PH specimens manufactured for several conducted studies were presented, we will present various corrosion performance evaluation metrics gathered from existing literature. These will also function as points of reference to develop a general understanding of how corrosion metrics fluctuate with different manufacturing processes, as well as the solutions in which the corresponding specimens are subjected during testing.

Although there's still not many studies available in the literature regarding the corrosion resistance of MFFF produced/AM extruded 17-4 PH, we can still gather figures referring to other AM technologies, as well as for wrought 17-4 PH. The latter is typically the most widely employed benchmark across numerous studies to gauge and compare the corrosion performance of tested specimens. The values are displayed in Table 2.5.

Table 2.5 - Corrosion characterization values of 17-4 PH obtained in several studies.

Manufacturing Technology	Solution*	Ecorr (mV) vs. Ag/AgCl/satKCl	Icorr ($\mu A/cm^2$)	Eb (mV)	Ref.
BMD (0°)	NaCl 0.35 wt. %	-80	0.044	-	[48]
BMD (90°)		-93	0.146	-	
LPBF (1h OCP)	0.6 M NaCl	-8	0.241	-	[49]
LPBF (24h OCP)		27	0.0728	-	
SLM (superficial direction)	0.5 M NaCl+0.5 M H_2SO_4	-281	24	300	[50]
SLM (transversal direction)		-344	21	386	
Wrought (longitudinal direction)		-379	1440	297	
Wrought (transversal direction)		-379	740	304	
Wrought	NaCl 0.35 wt. %	-61	-	264	[48]
Wrought (1h OCP)	0.6 M NaCl	93	0.0230	-	[49]
Wrought (24h OCP)		309	0.0027	-	

*M = mol/L
BMD: Bound Metal Deposition
LPBF: Laser Powder Bed Fusion
SLM: Selective Laser Melting

All these figures were taken out of polarizing curves obtained by means of three electrode cells and then by Tafel extrapolation. An example of these curves is shown in Figure 2.35.
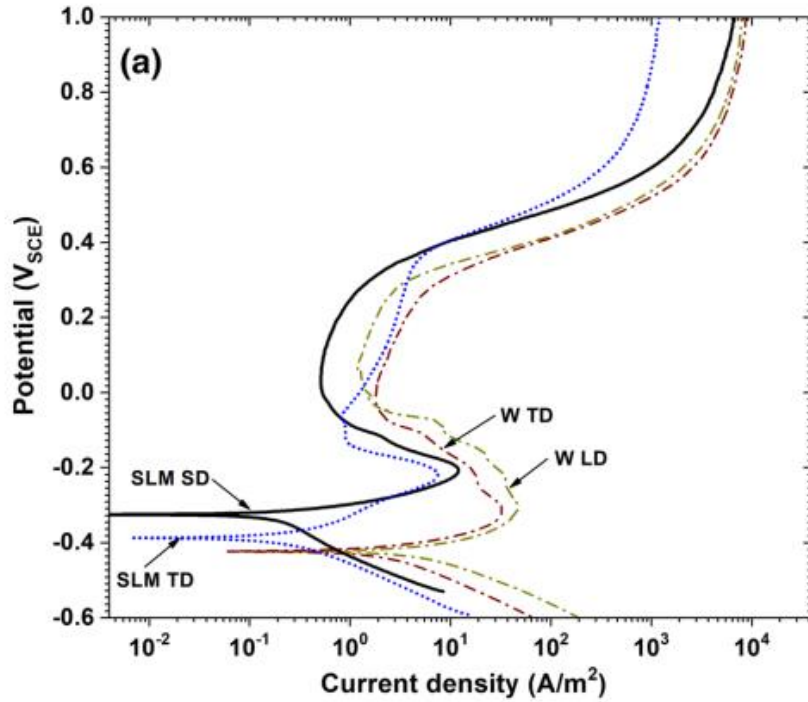
Figure 2.35 - Potentiodynamic polarization curves of SLM and Wrought samples [50].

The curves clearly show the active, passive and transpassive regions of the anodic polarization of the SLM fabricated samples (superficial and transversal directions) and of the wrought 17-4 PH specimens (both longitudinal and transversal directions), which is not always the case for real plotted curves.

It is important to note that Bound Metal Deposition (BMD) is a process quite similar, if not identical, to MFFF. Fortunately, the referenced research has also delved into the impact of build orientation on the corrosion resistance of the fabricated parts, which can provide a basis for potential comparisons in the future of this work. However, it is essential to highlight that most of these studies were conducted under varying conditions, namely, encompassing different solutions, different aeration conditions and slightly varying temperatures (not detailed in the table). Consequently, direct comparisons between results across studies become challenging, allowing only for intra-study comparisons. In addition, most of these studies were conducted in reference to a Saturated Calamel reference Electrode (SCE), which has a potential relative to the Standard Hydrogen Electrode (SHE) of +0.241V. For the purposes of this work, all the potentials were converted to reference the Ag/AgCl/saturatedKCl reference electrode, which is the one that is going to be utilized.

Nonetheless, some insights can be gleaned from these values. For instance, it is evident that specimens exposed to acidic solutions (containing H_2SO_4) exhibit lower corrosion potentials (*Ecorr*) and higher corrosion current densities (*Icorr*), indicating an increased susceptibility to corrosion.

Furthermore, it is notable that the corrosion metrics of the AM techniques closely align with those of the wrought specimens polarized under the same conditions, and in certain instances, even surpass them. This fact holds promise for the potential of AM processes in this field.

3. MATERIALS AND METHODS

I n this chapter, the materials used in this investigation, along with the descriptions of the experimental procedures conducted within the scope of this thesis are presented.

3.1. MATERIALS

The material used for this research was the *Ultrafuse* 17-4 PH filament, produced by *BASF*, which enables the production of stainless steel parts for applications that require high hardness and mechanical strength. 17-4 PH is a precipitation hardened stainless steel ideal for applications that need high strength and corrosion resistance. It can be fully heat treated to raise even further its levels of strength and hardness. It features good corrosion resistance and machinability and, being martensitic, it can be magnetized. It is therefore ideal for petrochemistry, aerospace, the automotive and the medical industry [2, 36].

The filament is a metal–polymer composite with a nonslip surface, allowing application in any Bowden or direct drive extruder. The next table presents the typical composition of the material after sintering, considering that the binder has been fully dissolved and degraded.

Table 3.1 - Typical composition (wt.%) of the material after sintering [51].

C%	Cr%	Ni%	Cu%	Nb%	Mn%	Si%	Fe%
≤ 0.07	15-17.5	3-5	3-5	0.15-0.45	≤ 1	≤ 1	Balance

Further information about the filament materials, such as binder composition, powder size or powder loading, are not disclosed by *BASF*. However, it is reasonable to assume that the binder composition might resemble the composition mentioned in Section 2.1.4, as the debinding strategy recommended by *BASF* aligns with these binder compositions. Regardless of that, some other information about the filament is shared with the consumer. This information is shown in Appendix A: *Ultrafuse* 17-4 PH Technical Datasheet.

3.2. PRINTING

The slicer software utilized for the development of this work was the *Ultimaker Cura* software, which is meant to be used along with any *Ultimaker* 3D printer. Firstly, samples were designed and scaled considering the OFS's presented in Table 3.4 and uploaded to the slicing software through a Stereolithography (STL) file. Some of these samples would be printed in order to be mechanically tested, some others would be produced for thermal characterization and the rest for corrosion performance testing and shrinkage evaluation after the sintering process. Half the samples belonging to the latter group were printed in an upright position relative to the printer's XY plane and the other half in a flat position

relative to the same plane, in order to investigate the building orientation effect on these aspects. All the other samples were also printed in a 0° position. This is especially important for the mechanical samples, as the aim is to achieve the best possible mechanical properties. The thermal samples would also be subjected to a density measurement. All these three sets of samples had different geometries.

In this investigation, a *Ultimaker* model S5 desktop 3D printer shown in Figure 3.1 was used. This is a Bowden extruder printer, which is appropriate given the hight density, (and weight) stiffness and viscosity of the used filament compared to polymeric filament, due to the metal powder loading. The printer was equipped with a CC red 0.6 *Ultimaker* print core (Figure 3.1). 0.6 corresponds to the nozzle diameter (in mm) and it contains an artificial ruby at the nozzle tip that was specifically developed to print with composite and abrasive filaments.
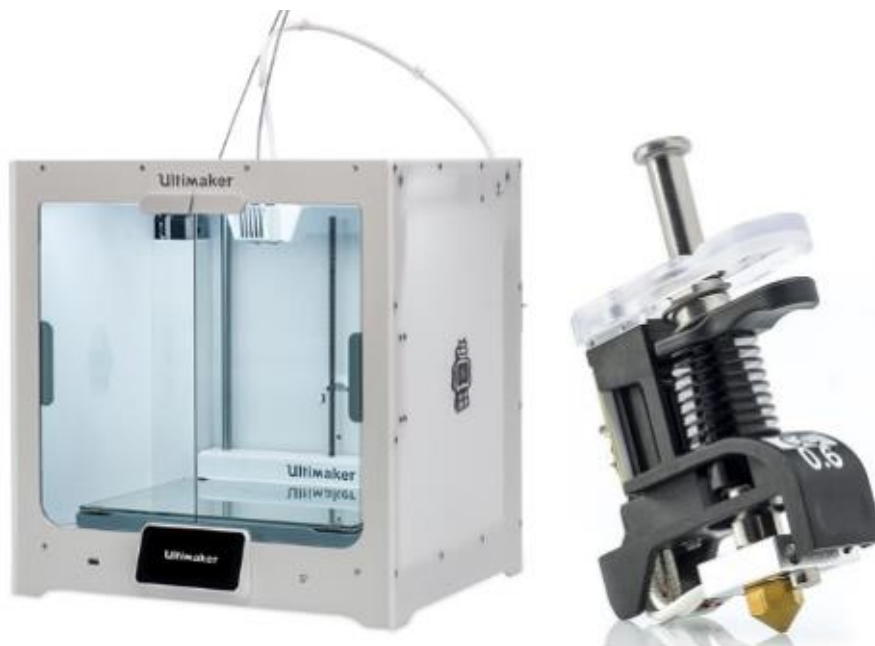
Figure 3.1 - Ultimaker S5 printer (left) and CC red 0.6 print core (right) [52].

Prior to starting the printing process, a calibration of the build plate level was needed. Firstly, a manual calibration was done by adjusting two height changing screws. Then, an automatic calibration was done. The *Ultimaker* S5 ensures accurate build plate calibration by having the print head's capacitive sensor scan the build plate at multiple points and compensates for any Z-axis offset by adjusting the height of the print's first layers.

The initial step in achieving a successful MFFF part is to ensure a flawless first layer during printing. This layer serves as the attachment point between the part and the build surface. A failure in this step can jeopardize the entire print job. Warpage issues often arise when there is inadequate adhesion between the part and build surface, leading to compromised part accuracy or even risking the complete loss of the part during debinding and sintering processes. In order to obtain a better adhesion and prevent separation and warpage, the recommended *Magigoo Pro Metal* adhesive was applied in the build glass before printing.

According to the manufacturer, the printing profile (Table 3.2) was intended to provide quality, flexibility, and reliability for the vast range of products and applications that *Ultrafuse* 17-4PH enables. Therefore, the parameters used were the ones recommended by *BASF*, although parameter calibration for a specific printer should be sought out, considering that variations between individual printers and their maintenance can impact part results. *BASF* configured these printing condition in their Cura slicing software plugin. Although not presented on the table, it is important to mention that the infill partner was arranged in lines and that the raster angle was set to be random on each layer. The objective is to minimize the anisotropy in both directions of the layer plane.

Table 3.2 - Printing parameters used for all the samples in this investigation.

Parameters	Unit	Value
Layer height	mm	0.1
Infill line width	mm	0.6
Wall line count	-	3
Top/Bottom layers	-	1
Infill density	%	105
Printing temperature	°C	240
Wall flow	%	100
Top/Bottom flow	%	105
Infill flow	%	100
Print speed	mm/s	25

Apart from the samples to be printed, a so called "skirt" was also added in the slicer software. A skirt is an extra feature made to prime the nozzle, ensuring proper extrusion and proper build plate calibration before part printing starts [20]. It is shown in Figure 3.2 and it is also visible in Figure 3.3. The printing process was then ready to start.
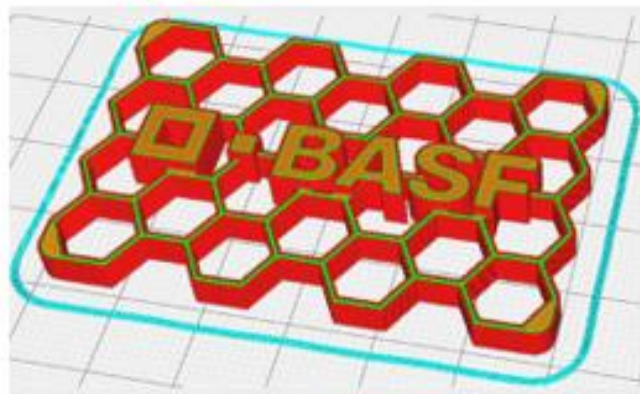
Figure 3.2 - Skirt illustration [20]

At the beginning of the printing, it was important to pay close attention to the first layers to ensure that these were adhering properly and that there was no discontinuity in

the print line or any other problem. Upon observation of a smooth progress, then the machine is left to print for a few hours. This duration depended on the type/size of the samples only, given that all of them were printed under the same parameters. The end of the printing process of the flat corrosion samples is shown in Figure 3.3.
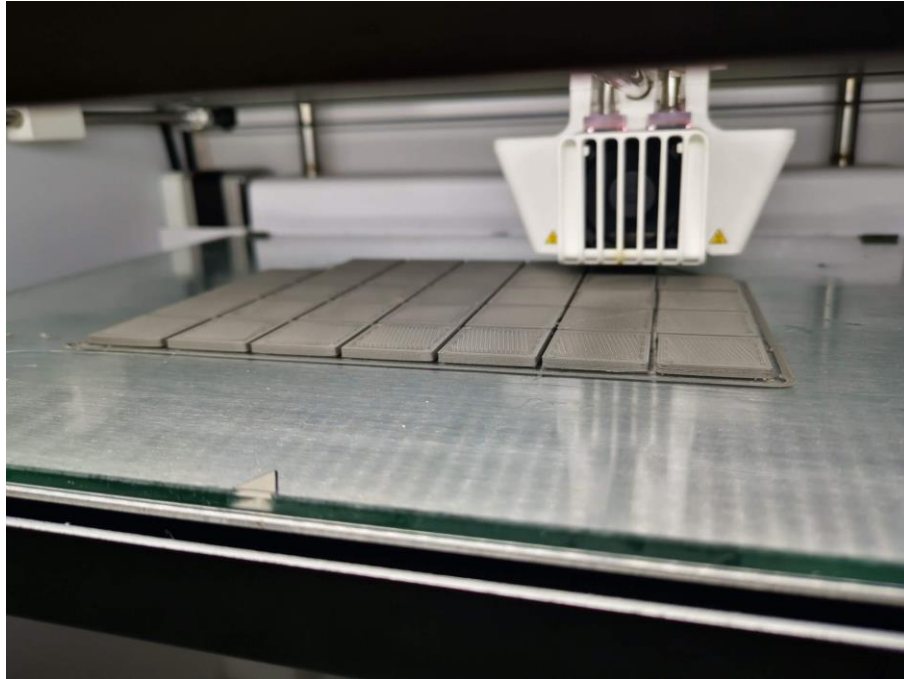
Figure 3.3 - Printing of the flat corrosion samples.

3.3. DEBINDING AND SINTERING

The 3D-printed samples were outsourced to a debinding and sintering service for postprocessing as recommend by *BASF*. The company recommends catalytic debinding to be performed at 120°C with nitric acid with a concentration greater than 98%. Based on a 50-liter debinding furnace a nitric acid feed of 30 ml/h and nitrogen as an exhausting with a throughput of 500 l/h are suggested as it is proven that these parameters lead to safe processing. At this gas throughput, the acid feed may not be increased to more than 38 ml/h. The debinding process is finished when a minimal debinding loss of 10.5 wt.% is reached. It' is important to refer to the oven manufacturer's instructions to avoid leakage and therefore hazardous conditions for both personnel and oven parts [53].

It is also advocated that sintering should be done in an atmosphere with 100% clean and dry hydrogen or argon. Alumina sintering supports of 99.6% purity are recommended. The sintering cycle should consist of a ramp from:

1. Room temperature to 600°C at 5K/min and hold 1h.
2. 600°C to 1300°C at 5K/min and hold 3h.
3. Furnace cooling.

In the early stages of the sintering process, backbone constituents are still being burnt off and the pyrolysis products should be removed by a suction fan [53].

After the whole SDS process, the specimens had the following appearance (Figure 3.4):
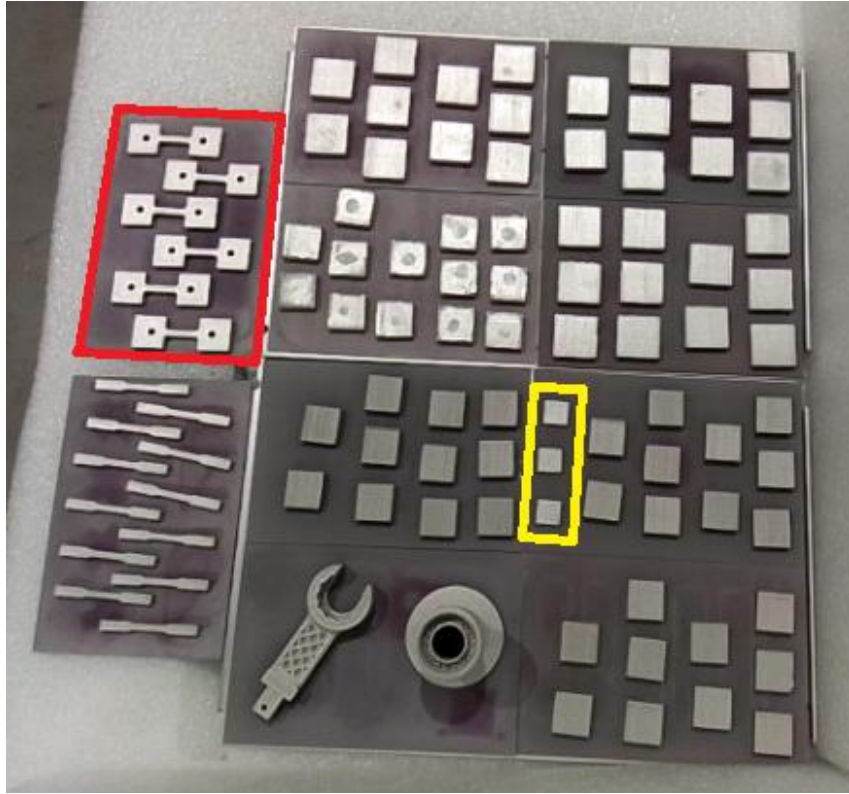
Figure 3.4 - Specimens after the SDS process. The mechanical ones are highlighted in red and the thermal ones in yellow. The corrosion specimens are any ten among the other squared ones.

3.4. MECHANICAL TESTING

In this chapter, the experimental procedure for conducting tensile tests on four samples will be outlined. The tests were performed for the purpose of characterizing the tensile behaviour of the considered MFFF printed material and to analyse the morphology of the fracture zone of tested specimens through SEM.

The tests were carried out using an *Instron 8872* Servo-Hydraulic Testing Machine, and the samples were subjected to two different strain rates to investigate their mechanical behaviour under varying loading conditions. Four samples were prepared for the tensile tests, identified as D01-01, D01-02, D10-01 and D10-02. The samples' nominal dimensions are presented in Figure 3.5. Additionally, one of the samples is shown below (Figure 3.6), along with the samples' most important measured dimensions after sintering (Table 3.3).
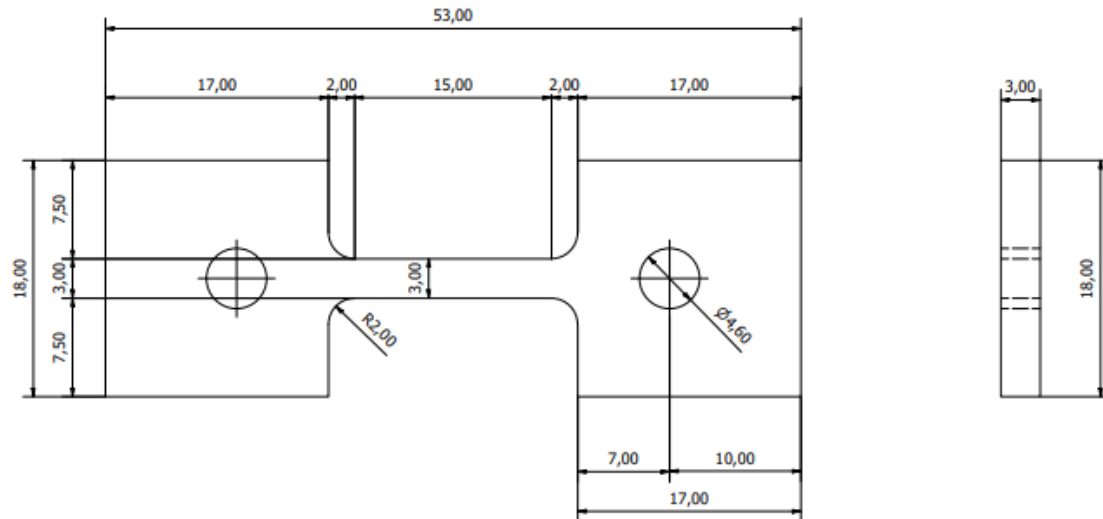
Figure 3.5 - Mechanical samples' dimensions.
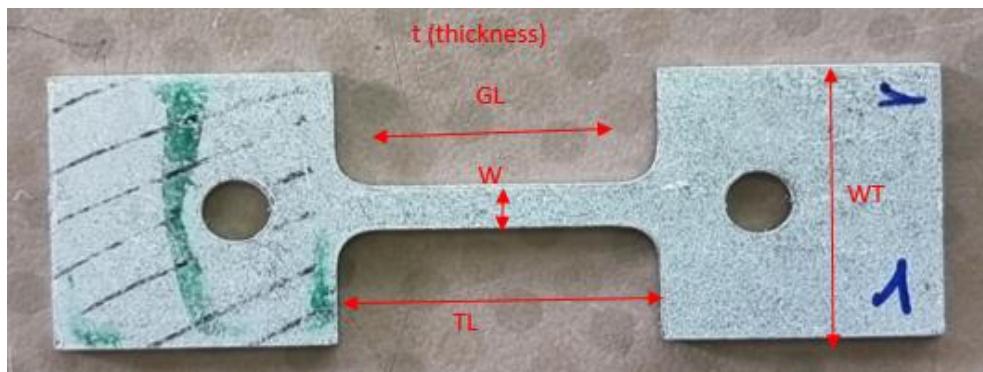
Figure 3.6 - Example of a mechanical sample and notation for some of its dimensions.

Table 3.3 - Dimensions of each mechanical sample.

Sample ID	Thickness/t (mm)	Gauge Width/W (mm)	Gauge Length/GL (mm)	Total Length/Ltot (mm)	TL1 (mm)	TL2 (mm)
D01-01	3.13	3.41	15.00	54.08	18.74	19.60
D01-02	3.14	3.46	15.00	54.03	19,29	19.03
D10-01	3.13	3.41	15.00	54.11	18.94	19.45
D10-02	3.13	3.43	15.00	54.04	19,33	19.03

The samples were carefully mounted in the Instron 8872 Servo-Hydraulic Testing Machine, ensuring proper alignment and fixation to minimize any potential errors during testing, as presented in Figure 3.7. The primary objective of the dynamic tensile tests was to evaluate the mechanical response of the samples under different strain rates. Considering the sample dimensions, the machine speed for the tests was set at 15 mm/s for the first two samples (D01 samples) and 150 mm/s for two D10 samples, in order to subject the first two samples to a strain rate of 1 s^{-1} and the latter ones to a higher strain rate of 10 s^{-1}. Strain rate

refers to the rate at which the samples are subjected to deformation during the test. Notably, these are considerably high strain rates. The objective here is twofold: firstly, to assess the mechanical properties of 3D-printed 17-4 PH stainless steel using the MFFF process and secondly, to explore the impact of strain rate on these properties.

Figure 3.7 – Specimen mounting/positioning on the testing machine.

During the dynamic tensile tests, the testing machine continuously recorded various parameters, including load, displacement and time, until the fracture of each specimen occurred. This information was collected in real-time and used to generate stress-strain curves for each sample.

The obtained stress-strain curves from the dynamic tensile tests were analysed to understand the differences in mechanical properties and behaviours between the samples tested at different strain rates.

To analyse the morphology of the samples, a scanning electron microscope *SEM EVO 15* (Zeiss, Cambridge, UK) was used. To gather the information, a piece of material containing the fracture zone was cut from each sample and they were positioned and tightened on a sample stub, as displayed in Figure 3.8. The SEM analysis has been carried out at different magnifications ranging from 50x to 600x. The electron source used was a LaB6 filament.
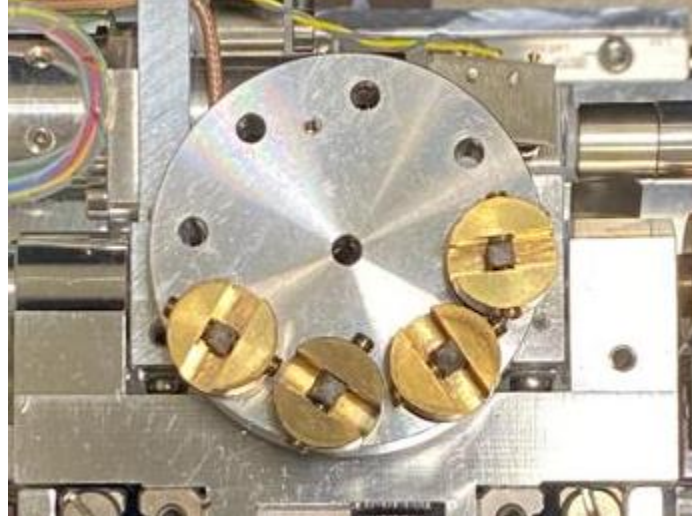
Figure 3.8 - Positioning of the cut pieces of the samples for the SEM analysis.

The tensile test results and some of the images gathered will be presented and discussed in Section 4 to draw meaningful conclusions regarding the mechanical performance of the samples under dynamic loading conditions and their morphology.

3.5. THERMAL CONDUCTIVITY AND DIFFUSIVITY MEASUREMENT

Thermal diffusivity is one of the essential parameters that needs to be determined for alloyed steels used in various applications, including catalytic reactors, heat exchangers, and more. The calculation of thermal conductivity employs the following equation:

$$k = \alpha \cdot \rho \cdot C_p \,, \tag{7}$$

where k is the thermal conductivity (W/mK), α is the thermal diffusivity (m²/s), which represents a material-specific property characterizing the non-stationary heat conduction, C_p is the specific heat (J/kgK), and ρ is the density of the specimen (Kg/m³). By knowing the quantities on the right-hand side of the equation, the values of thermal conductivity can be obtained.

In particular, the values of thermal diffusivity were derived in the laboratory using the *LFA 467 HT HyperFlash* (NETZSCH-Gerätebau GmbH) machine capable of working with square samples measuring 12.7 mm on each side and 2 mm in thickness. The machine can test samples under adiabatic conditions, employing liquid nitrogen cooling systems, while extrapolating the time intervals required to reach predetermined temperature gradients (in our case, set at 25°C). The role of liquid nitrogen is to cool down the machine's electronics due to the high thermal peaks generated by the laser during the test. For refilling the liquid nitrogen, it is necessary to wear personal protective equipment, including cryogenic gloves and protective goggles, as required by regulations. Once the reservoir is filled using a funnel, the furnace is opened, and the three samples are carefully inserted into their slots, which are shown in Figure 3.9, making sure to remove the protective shield, which is not needed during this phase.
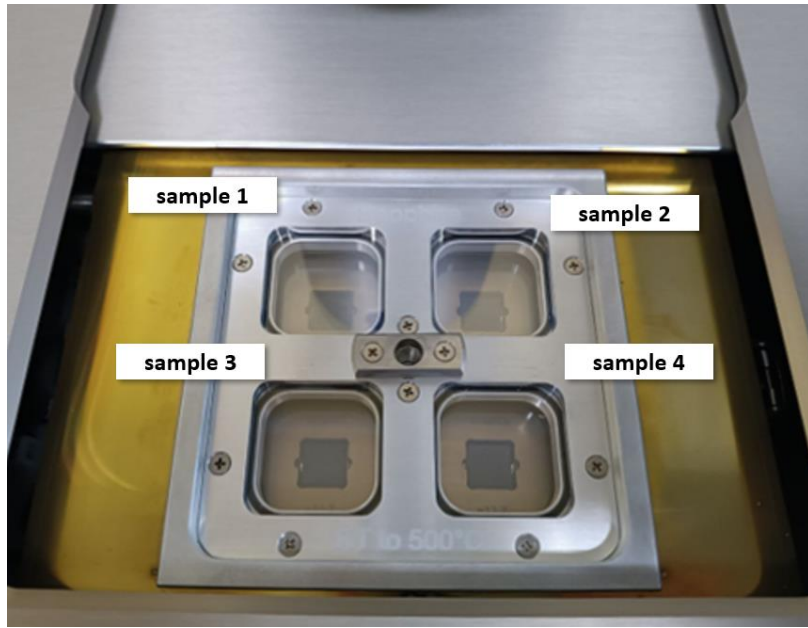
Figure 3.9 - Sample slots in the Hyperflash machine.

The Proteus program processes the obtained data and provides the sought-after values of thermal diffusivity through the formula:

$$\alpha = 0.1388 \frac{s^2}{t_{0.5}},$$ (8)

where s represents the sample thickness, and $t_{0.5}$ is the time required to achieve a temperature increase of 50%. In order to reduce the reflectance values of the samples and enhance the emissivity of the radiation emitted in the visible and near infrared wavelengths, a graphite coating has been applied to the samples to render them opaque.

3.5.1. DENSITY MEASUREMENTS

The determination of part densities at the end of the sintering process is of fundamental importance, not only to evaluate the actual efficiency of the debinding and sintering process, but also to obtain the thermal conductivity values. The measurements were carried out using a precision scale equipped with a platform that allows weighing operations both with the sample immersed in the suspension liquid and in air (Figure 3.10). The actual density value is obtained through the application of Archimedes' principle, which involves first weighing the sample in air and then weighing it again while fully immersed in the suspension liquid, which, in our case, is distilled water.
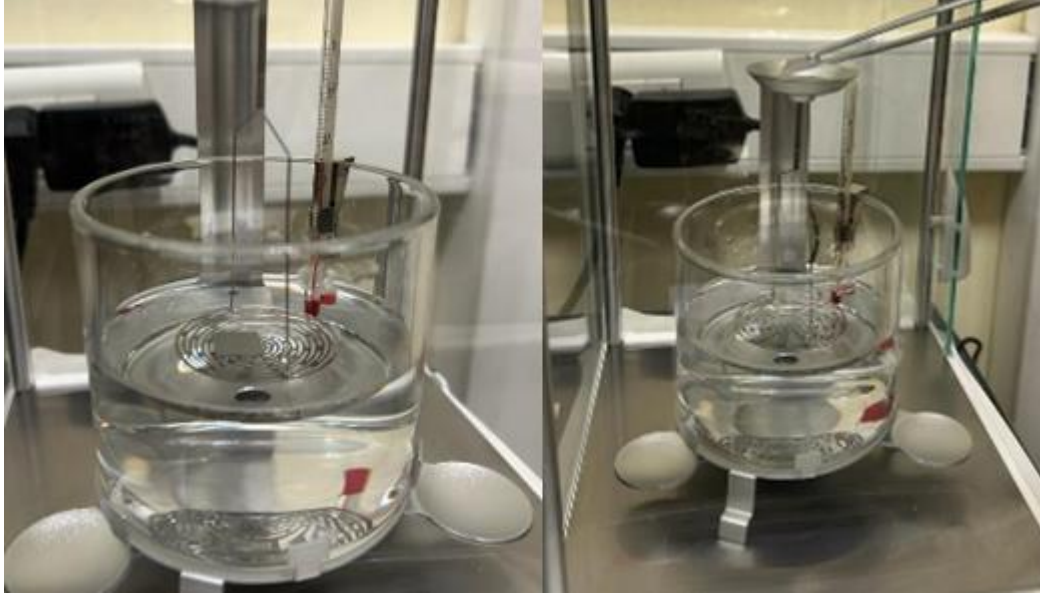
Figure 3.10 - Sample weight measurement immersed in water (left) and in air (right).

The precision scale is equipped with a mercury thermometer to also measure the temperature at which the measurement is conducted since, as known, density is influenced by temperature. Once the two density values are known, it is possible to calculate the density value using the following equation:

$$\rho = \frac{w_{air}}{w_{air} - w_{liq}}(\rho_l - \rho_a) + \rho_a \,, \tag{9}$$

where ρ is the density of the sample (g/cm^3), w_{air} is the weight of the sample in air (g), w_{liq} is the weight of the sample in the liquid (g), ρ_l is the density of water at room temperature (g/cm^3), and ρ_a is the density of air at atmospheric pressure (g/cm^3).

Once the values of density, specific heat, and thermal diffusivity are known, it is possible to calculate the values of thermal conductivity for the examined 17-4 PH stainless steel samples. In Chapter 4, the experimentally calculated values of both thermal diffusivity and thermal conductivity at monotonically increasing temperature values from 25°C to 200°C in 25°C intervals are displayed.

3.6. SHRINKAGE EVALUATION

The 3D printed parts need to be overdesigned considering the dimensional variations through the entire process. For that reason, comparing the part's dimensions before and after sintering is important to understand the influence of several parameters on the shrinkage and, ultimately, to acquire insights on appropriate part design.

Accordingly, a shrinkage evaluation was performed on two sets of squared specimens. For this effect, as well as for the corrosion performance testing, two sets of samples were produced. The first set was printed in a flat position (A samples, Figure 3.11) and the second group in an upright position (B samples, Figure 3.12), relative to the printer's axes (see Section 2.1.2). It is important to mention that, despite the samples building

orientation, they were all sintered in a flat position, which will influence their shrinkage in different directions. Therefore, in subsequent sections, two sets of X, Y and Z (Z being always the height) axes can be considered: one relative to the printing process and the other to the sintering process.
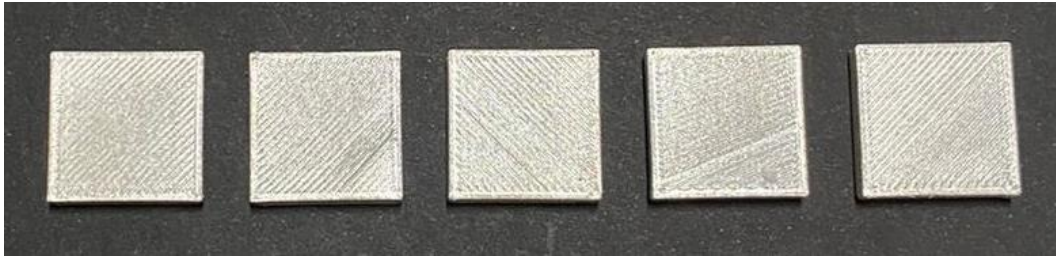
Figure 3.11 - Flat samples (A group).
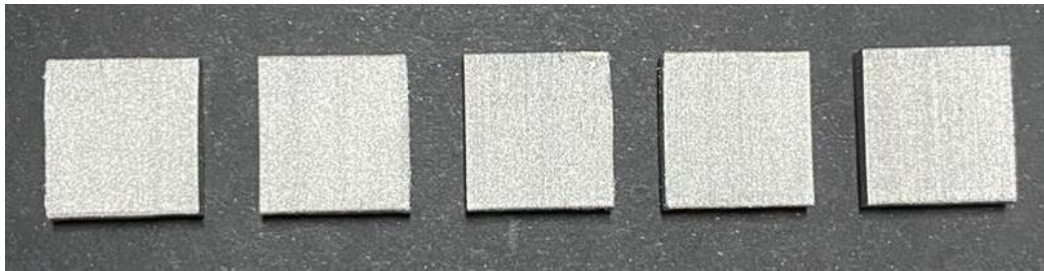
Figure 3.12 - Upright Samples (B group).

The nominal dimensions of the flat specimens, regarding printing axes, were:

- X and Y = 24 mm
- Z = 4 mm

And regarding the upright specimens we have:

- X and Z = 20 mm
- Y = 5 mm

In this case, *BASF* provides the shrinkage and OFS values for metal filaments printed using their recommended parameters, relative to sintering axes, which are presented in Table 3.4.

Table 3.4 - Shrinkage and scaling [20].

Sintering Axis	Average Shrinkage	Oversizing Factor
X / Y	16%	119%
Z	20%	122%

Essentially, the Z sintering dimension corresponds to the thickness of both types of samples. Thus, by using the recommended OFS and resorting to Eq. (3), the flat specimens were designed with the following green part printing dimensions:

- X and Y = 28.6 mm
- Z = 4.9 mm

While the upright specimens had the following sizes:

- X and Z = 23.8 mm
- Y = 6.1 mm

The samples were then carefully measured using a digital calliper. In Section 4, firstly, we will discuss any eventual deviations of the samples' proportions compared to their intended nominal sizes and, afterwards, the degree of shrinkage from the green parts to the sintered ones will be assessed.

3.7. CORROSION RESISTANCE TESTING

For complex design and lifetime assessment of each application, it is inevitable to consider not only the mechanical characteristics of the bulk material but also the resistance of its surface to the degradation effects of its environment. With this in mind, corrosion testing was proposed and the procedure used in this study is going to be explained.

Firstly, the specimens to be tested were sent to the University of Modena e Reggio Emilia, where the corrosion testing took place. Afterwards, the corrosion resistance in terms of *Ecorr* and *Icorr* was assessed through an electrochemical polarization process, called potentiodynamic polarization test, in which an electric potential is applied to a sample, which is going to function as the working electrode, (WE) and is then compared to a reference electrode (RE) and the current between the sample and an inert counter electrode (CE) is measured. For this purpose, an Ametek Princeton Applied Research Flat Cell (Figure 3.13) with a volume capacity of 300 mL, serving as a three-electrode glass cell, was utilized in conjunction with a potentiostat (Versastat, Ametek Princeton Applied Research). An Ag/AgCl/KCl(sat.) reference electrode and a platinum grid counter electrode were employed. Two flat printed samples and two upright printed samples were connected one at a time as the working electrode, with an exposed surface area of 1 cm². The tests were conducted in a 3.5 wt.% aqueous NaCl solution at room temperature. This specific NaCl concentration is fairly standard and widely used for corrosion resistance testing as it is meant to mimic a marine environment, given that the average salt concentration in the ocean is very close to this value [54]. This type of environment is considered electrochemically aggressive because the main reactive pitting mechanisms exist when anionic species such as chloride ions are involved. The aggressiveness of pitting varies with the logarithm of the bulk chloride concentration. The chloride ion, anion of strong acid, tends to pose high level of solubility to metallic cations, which interferes with passivation of the metallic surface [55].
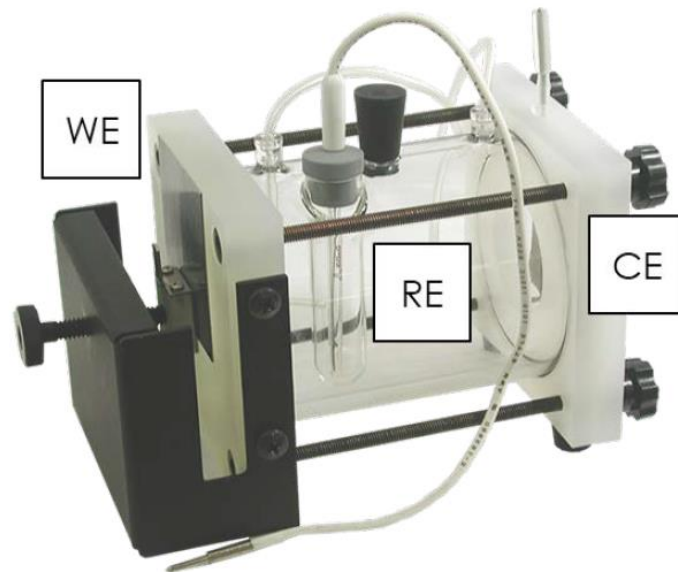
Figure 3.13 - Flat Cell, Ametek Princeton Applied Research. WE: corresponds to the test sample, RE: Ag/AgCl/KClsat, CE: Pt.

To allow the system to stabilize partial corrosion processes and reach its OCP, the samples were left in contact with the solution for 1 hour, without imposed overpotentials. Subsequently, the test was divided into two phases: an initial phase where an overpotential range from 0 V to -0.4 V (relative to OCP) was scanned at a scan rate of 0.5 mV/s, and a second phase where overpotentials from -0.4 V to +1.6 V (relative to OCP) were imposed, also at a scan rate of 0.5 mV/s.

Polarization curves (current density vs. potential) were then obtained and plotted within the specific range of interest, from -0.4 V to +1.6 V (relative to OCP). The corrosion current density and corrosion potential were determined using the Tafel linear approximation in the cathodic and anodic regions of the curves. The primary objective of this testing protocol extends beyond the mere assessment of corrosion resistance in MFFF manufactured components. It seeks to probe into the relationship between building orientation and corrosion resistance, facilitating a comprehensive analysis of how different building orientations impact corrosion resistance and allowing for a meticulous comparison between these orientations in this context. Results will be presented and analysed in Chapter 4.

4. RESULTS AND DISCUSSION

Within this section, the results acquired in all different tests and evaluation procedures and their respective analysis are presented.

4.1. DENSITY RESULTS

This chapter begins by presenting the density results, because understanding the density of the specimens is not only essential for calculating thermal conductivity, but it also plays a pivotal role in the subsequent interpretation of the tensile and corrosion properties of the printed parts. Density is a significant factor influencing these properties, as will be discussed later in this chapter. While we focused on assessing the density of thermal samples, it is important to note that all samples in this study were printed using identical parameters. Therefore, it is reasonable to assume that they share a similar level of density and porosity.

Following the methodology outlined previously, the weights of the three samples in both air and water were measured, facilitating the subsequent calculation of their density. For reference, the established conventional density value for 17-4 PH is usually pinpointed as 7.8 g/cm^3, a value commonly reported in the literature [56, 57]. The calculated density of each sample and their average are displayed in Table 4.1, as well as the relative density.

Table 4.1 - Density values of the thermal samples.

W_{air} (g)	W_{liq} (g)	T (C°)	ρ_{water} (g/cm³)	ρ_{sample} (g/cm³)	Average ρ_{sample} (g/cm³)	ρ_{sample} (%)	ρ_{air} (g/cm³)	$\rho_{literature}$ (g/cm³)
2.491	2.157	25	0.997	7.428	**7.474**	**95.24**	0.001	7.800
2.523	2.190	27	0.997	7.542				
2.492	2.159	27	0.997	7.450				

As depicted in the table, the bulk density of the thermal specimens reached approximately 7.474 g/cm^3, resulting in a relative density of 95.24%. This corresponds to a porosity level of nearly 5%. This value is considered satisfactory, as it closely aligns with many density values reported in numerous studies documented in the literature [1, 57]. However, there are also studies reporting higher densities obtained with this technology [10, 35], which implies that the present processing strategy may not have been optimal.

4.2. TENSILE PROPERTIES

All the tension specimens were monotonically loaded until failure. The resulting engineering stress strain curves for the specimens can be seen in Figure 4.1 and the fractured specimens can be observed in Figure 4.4. The data refers to the stress calculated as load divided by the specimens' initial gauge cross section, that is, gauge width multiplied

by the thickness. The deformation was calculated by dividing the change in length by the original length of the gauge section.
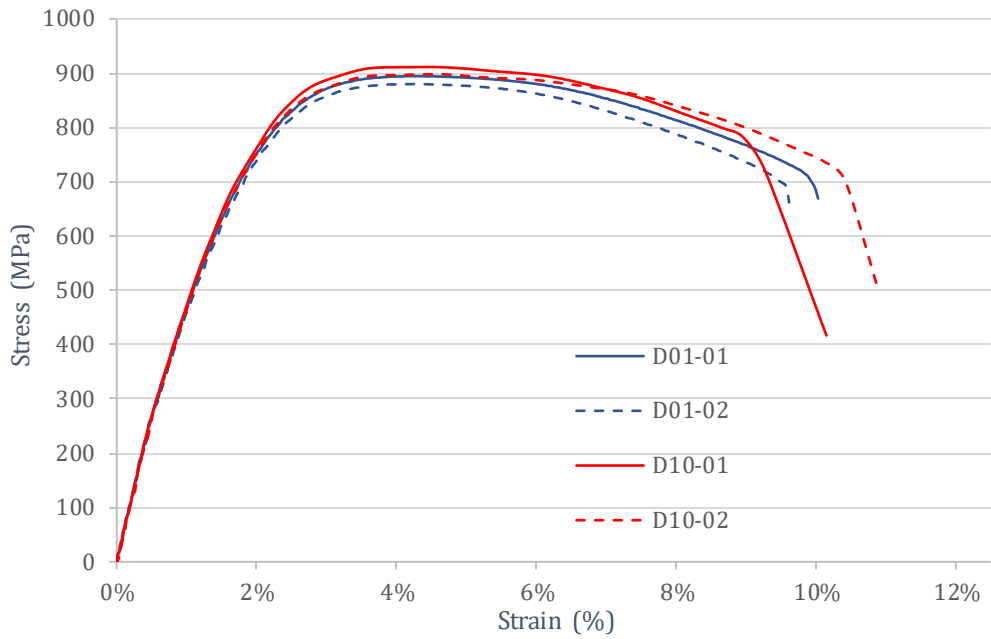
Figure 4.1 - Stress vs. Strain curves for all mechanically tested specimens. The curves in blue correspond to the samples tested at 1s⁻¹ strain rate, while the curves in red correspond to the samples tested at a strain rate of 10s⁻¹.

After plotting the previous curves, the elastic modulus was estimated through a linear tendency line for each sample's curve. Subsequently, a parallel line, using the elastic modulus as slope, was drawn for each sample with an offset at the 0.2% strain mark. The yield strength of each sample was determined by identifying the point where these lines intersected with their respective stress-strain curves, as exemplified in Figure 4.2. The resulting mechanical properties were also tabulated, as can be seen in Table 4.2.
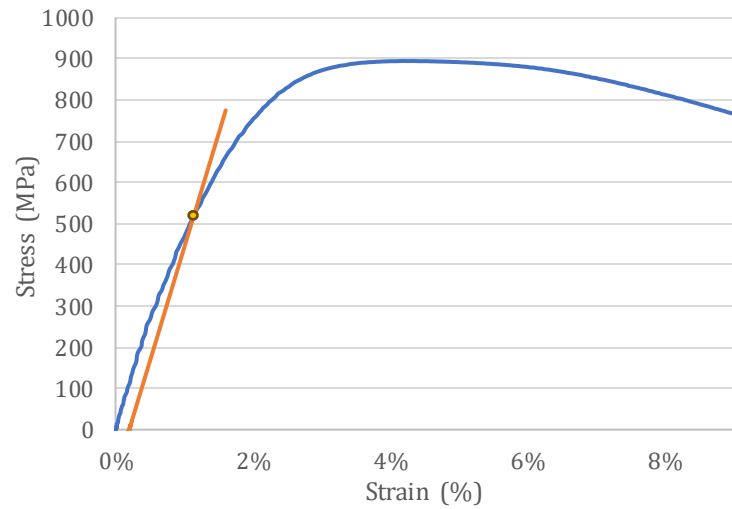
Figure 4.2 - Intersection between a D01 tensile curve and respective 0,2% offset line for tensile strength determination.

Table 4.2 - Tensile properties of the four mechanically tested samples.

Sample	Strain Rate (s^{-1})	Yield Strength (MPa)	Tensile Strength (MPa)	Elastic Modulus (GPa)	Strain at Failure (%)
D01-01	1	512	895	55.0	10.0
D01-02	1	502	880	54.3	9.5
Average D01	**1**	**506**	**888**	**54.7**	**9.8**
D10-01	10	555	911	54.4	9.3
D10-02	10	556	898	53.3	10.4
Average D10	**10**	**556**	**905**	**53.9**	**9.9**

The first notable aspect of the information above is that, although the samples were tested at two different strain rates, every specimen tested had a similar tensile behaviour. Nonetheless, we can still notice a slight increase in yield and tensile strength in the samples tested at a higher strain rate. This effect has been widely observed in several past research [58, 59] concerning many different metals and is one of the fundamental premisses of empirical models, such as the Johnson-Cook (J-C) material model [60].

The impact of temperature and strain rate on material behaviour, both at high and low rates of loading, is integrated into this material model using empirical parameters within the J-C equation. These parameters, when correctly calibrated, can be employed in numerical simulations to yield more precise physical responses for a product subjected to varying loading conditions throughout its research and development phase. However, given the fact that these parameter values differ among distinct material groups, it wasn't possible to delve into this model under the circumstances of this work, because each parameter must be uniquely ascertained for each cluster of similar materials to ensure accurate simulation and prediction of their behaviour. For determining these parameters, a wider variety of strain rates, encompassing low, intermediate and high loading speeds, must be employed [61].

There are many other ways of assessing strain rate dependence. Since the tensile tests under the scope of this work were only performed using two different strain rates, one can calculate the strain rate sensitivity. This refers to the degree to which a material's mechanical properties change in response to variations in this rate. The strain rate sensitivity parameter, *m*, can be obtained using the following equation [59]:

$$m = \frac{\log\,[\sigma_1/\sigma_2]}{\log\,[\dot{\varepsilon}_1/\dot{\varepsilon}_2]} \tag{10}$$

The ultimate tensile strength measured during an individual test is denoted as σ when assessing *m*. Subscripts 1 and 2 are used in reference to a set of tests for comparison, where σ_1 and σ_2 represent the tensile strength mean values corresponding to the respective strain rates of ε_1 and ε_2. In the equation above, assigning specific subscripts to particular strain rates ($1s^{-1}$ and $10s^{-1}$) is irrelevant, as the properties of logarithms yield the same result regardless. The calculated value comes at 0.0082. There's not much research on this strain rate dependence for MFFF parts, but there is for SLM. The value obtained in the present study is lower than other strain sensitivity values reported in the literature for as-built SLM 17-4 PH [62], indicating that the tested samples' properties were not considerably sensitive

to strain rate modification. In fact, this value is comparable to values obtained for heat treated 17-4 PH, which is considered to be less sensitive to strain rate variation [59].

In comparison to the values reported in the literature, our study reveals some notable distinctions, particularly regarding yield strength and tensile strength. It is evident that our findings generally fall below the established standards documented in previous MFFF research, presented in Table 2.4. Specifically, our yield strength measurements rank among the lowest when compared to the values reported in the literature, even when considering the results from the tested upright printed specimens. Furthermore, our obtained tensile strength is generally lower than that reported in most studies, though it does exceed that of some. For convenience, a bar chart displaying some of the most notable figures of yield and tensile strength from Table 2.4 is displayed in Figure 4.3. For a fairer comparison, the values obtained with the lower strain rate tested are shown.
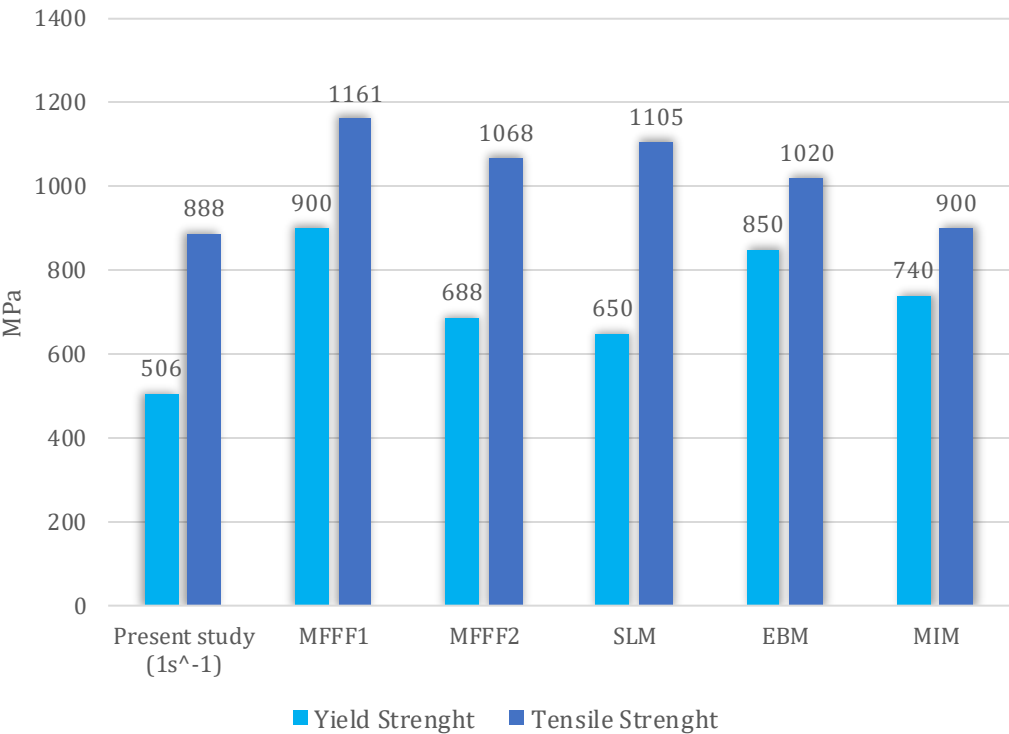
Figure 4.3 - Notable tensile properties from several manufacturing technologies in the literature for 17-4 PH.

One exceptional set of material properties found in the literature stands out, serving as a benchmark for our work. This study achieved exceptionally high values for both yield and tensile strength [10], primarily attributed to an outstanding relative density of over 99%. Attaining such a level of density is indeed challenging but holds significant promise. In this context, this study becomes a crucial reference for our research. The primary differences between our printing process and this exemplary study revolve around key printing parameters. Notably, the layer thickness employed in said work was double that of our study, measuring 0.2 mm. Additionally, they utilized a considerably lower extrusion temperature of 210°C. Although we lack precise information about the powder loading of the filament used in our research, it is worth mentioning that the filament in the study in

question contained 64 vol.% of metal particle loading, which is notably higher than most used filaments found in the literature. In [33], another study achieving remarkably high tensile strength, an infill pattern consisting of parallel lines interleaved at 45°/-45° on each consecutive layer was employed. In [35], the same raster angle approach was adopted, along with a higher layer thickness that led to a relative density of 98.6%, further reinforcing the importance of adjusting the printing parameters for better mechanical performance.

Furthermore, when compared to the as-sintered properties of 17-4 PH specimens as indicated by *BASF* in their datasheet displayed in the Appendix [51], our results showcase intriguing differences. Specifically, we achieved a lower yield strength and a higher ultimate tensile strength. It is noteworthy to mention that the material and recommended printing parameters were supplied by *BASF*. Additionally, the catalytic debinding and sintering processes were also performed by *BASF*.

It is also pertinent to acknowledge that the elastic modulus values obtained in our study were considerably lower than those typically reported in the literature for MFFF parts. These values even deviate significantly from the expectations for a precipitation hardening stainless steel, suggesting a more elastic and ductile behaviour in our printed specimens.

In contrast to other AM processes, such as PBF techniques, our MFFF specimens exhibit differences in material properties, particularly in terms of yield and tensile strength. Notably, their properties surpass the values obtained in the present study. These disparities can be primarily attributed to the inherent characteristics of these processes. In processes like EBM and SLM, we observe a complete localized melting of powder particles, as opposed to the sintering process employed in MFFF. This results in parts with considerably higher density, often achieving full relative density [46]. Conversely, in the case of DMLS, while it does involve sintering, it doesn't entail the removal of binder material. Consequently, the powder to be sintered in DMLS exists in much higher density, reducing porosity in the final part. Nonetheless, the MFFF studies previously mentioned managed to obtain higher densities than these methods, further emphasizing the importance of originating fully dense parts.

Comparing results from MFFF and MIM specimens is particularly interesting. This comparison is compelling due to similarities in the feedstock composition and debinding methods. Existing literature data for MIM parts reveal that our MFFF specimens exhibit comparable strength outcomes, albeit with a more ductile behaviour and still lower yield strengths. This stands in contrast to the findings of other MFFF studies documented in the literature review.

It is important to keep in mind that most of the numbers seen in the literature for tensile properties are respective to quasi-static tensile testing, whereas the present values were taken from dynamic tensile testing, given the relative high strain rates. Hence, the current figures are inflated, indicating that the actual properties being compared may be even more significantly lower than those reported in the literature.

The variation in physical properties across specimens manufactured by distinct technology sections can be elucidated through an examination of the microstructures developed during the manufacturing processes. Microstructure encompasses a wide range of characteristics, including porosity, pore shape, crack density, dislocation density, grain size, and more. Given the significant diversity in microstructures among these specimens, particularly in terms of porosity and the types of internal structural defects, it becomes evident why substantial differences in strength are observed.

4.2.1. SEM OBSERVATIONS

As previously noted, following the tensile testing, we examined the fracture zones of some of the fractured samples, namely, of the samples tested under strain rates of $1s^{-1}$ (marked as 01 and 02) and $10s^{-1}$ (marked as 03 and 04). Pictures of these sets of samples were taken (Figure 4.4) prior to cutting them for SEM imaging.
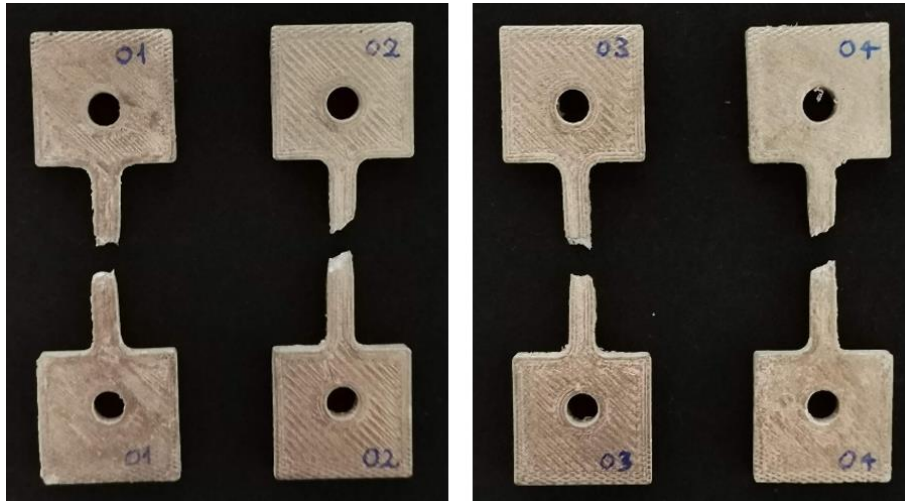
Figure 4.4 – Samples' appearance after tensile failure, showing necking of the gauge section.

Upon initial examination, a subtle necking phenomenon is evident in the gauge section of the specimens, indicating that ductile fractures occurred, aligning with the anticipated behaviour for stainless steel. Moreover, all specimens exhibited fractures close to the midpoint of their gauge length rather than at the sample shoulders. This observation strongly implies the absence of significant defects in this zone stemming from the printing process. Notably, the likelihood of such defects increases when specimens are printed in an upright orientation due to the susceptibility to interlayer failures, which typically result in brittle fractures characterized by minimal plastic deformation [33]. This analysis underscores the importance of the printing process in preserving the structural integrity of the specimens, particularly in terms of interlayer adhesion.

There are no discernible differences in the visual appearance of the fractured specimens, regardless of the strain rate. This similarity is also observed in the SEM images that have been captured. Below, some of the fracture images that were taken are displayed.
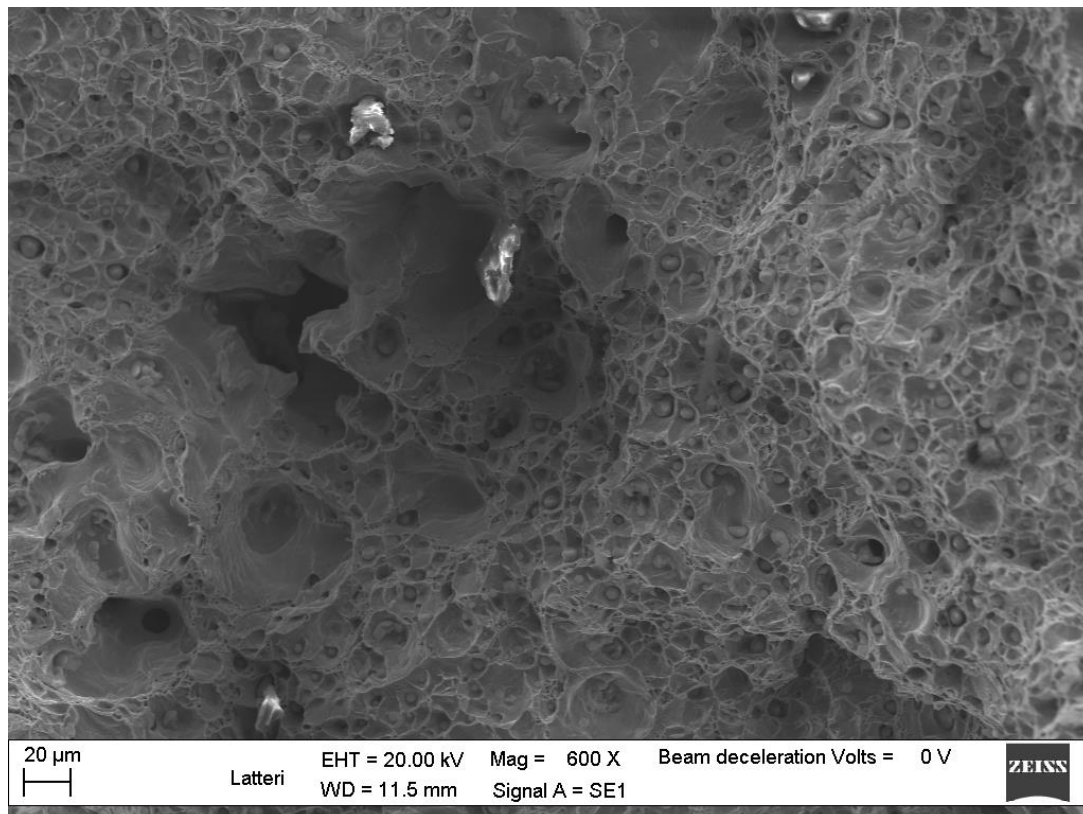
Figure 4.5 - SEM image of a 1s⁻¹strain rate tested sample's fracture zone (magnified 600×), showing relatively big pores and small inclusions.
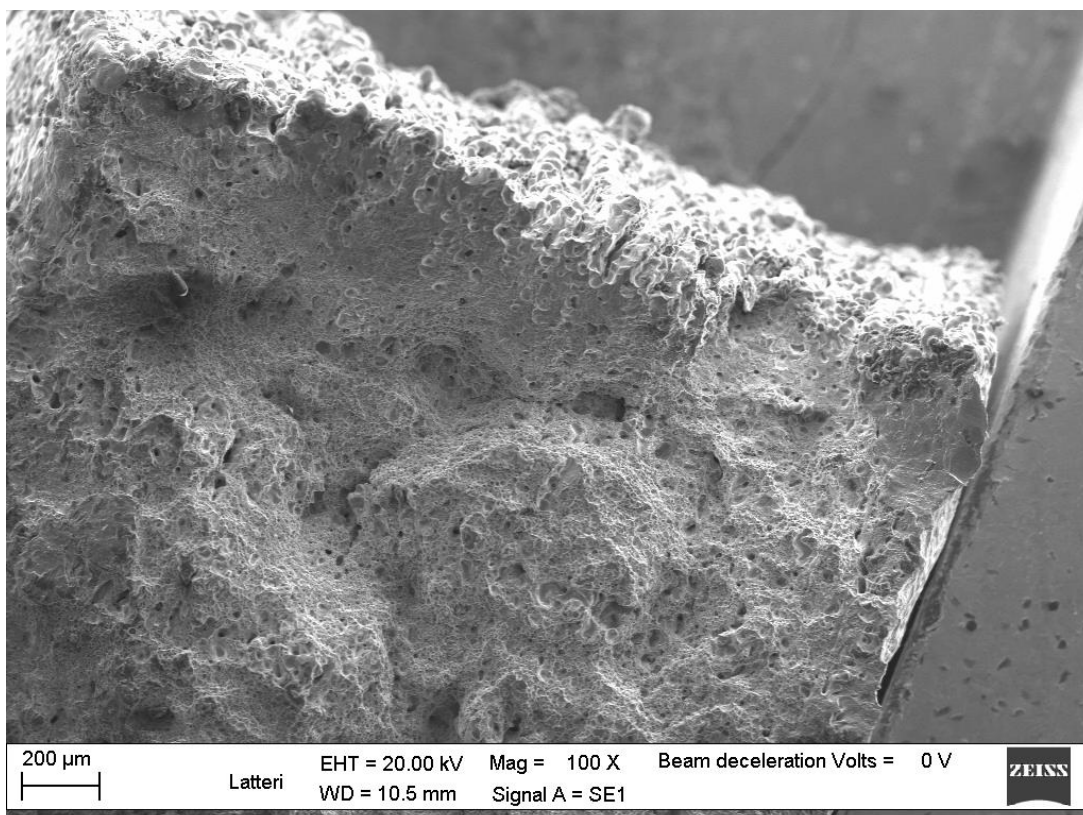
Figure 4.6 - SEM image of a 1s⁻¹strain rate tested sample's fracture zone (magnified 100×) showing flatter fracture regions.
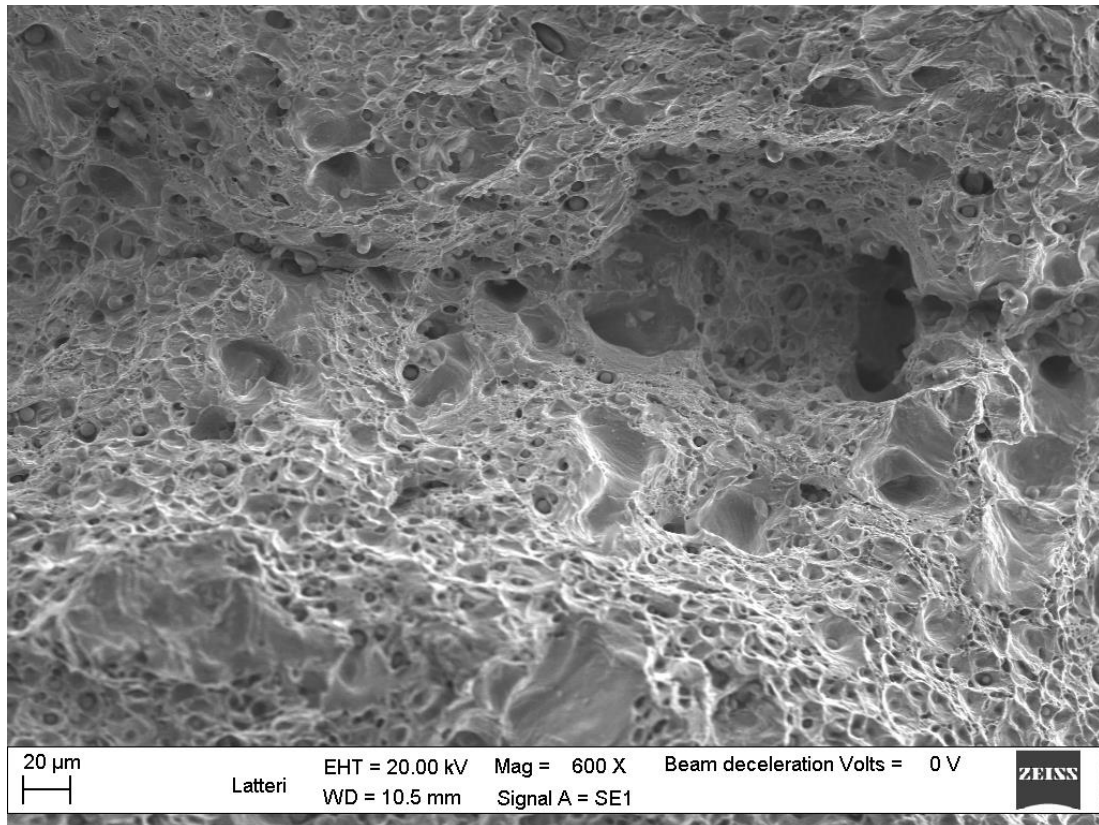
Figure 4.7 - SEM image of a $1s^{-1}$ strain rate tested sample's fracture zone (magnified 600×) showing small crack originating in a void.
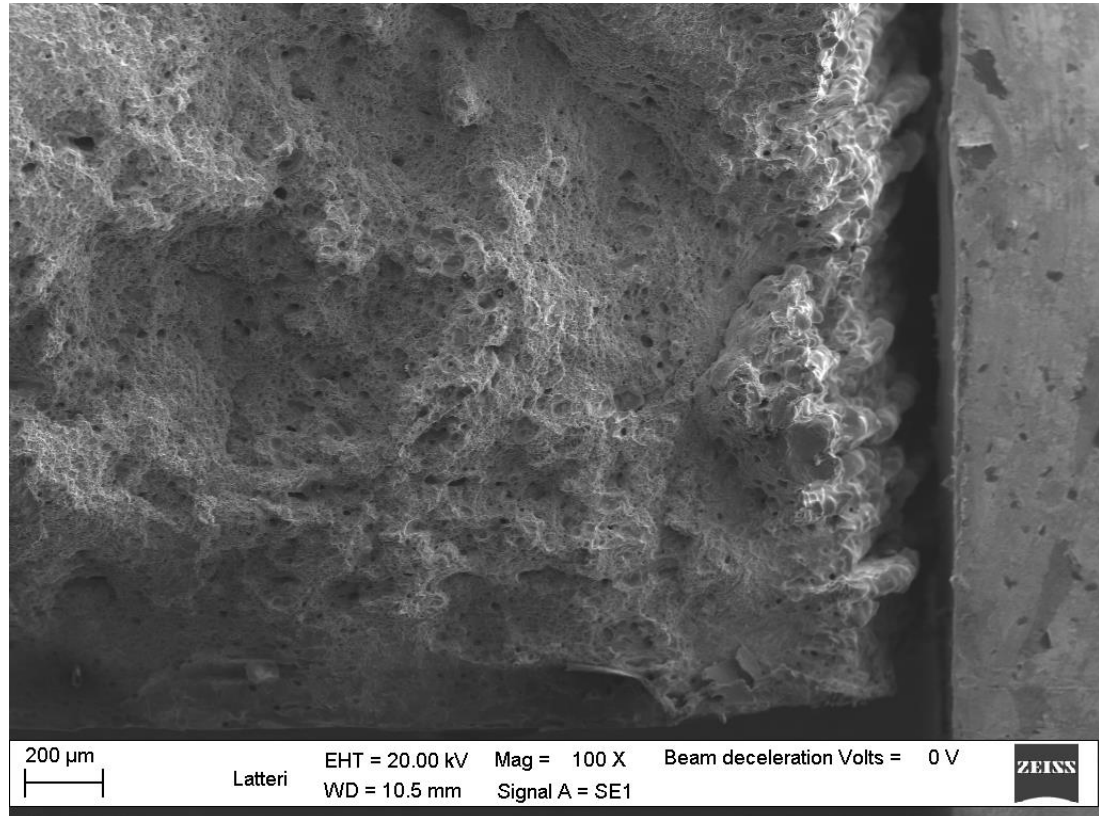
Figure 4.8 - SEM image of a $10s^{-1}$ strain rate tested sample's fracture zone (magnified 100×) showing crack propagating from the wall's raster.
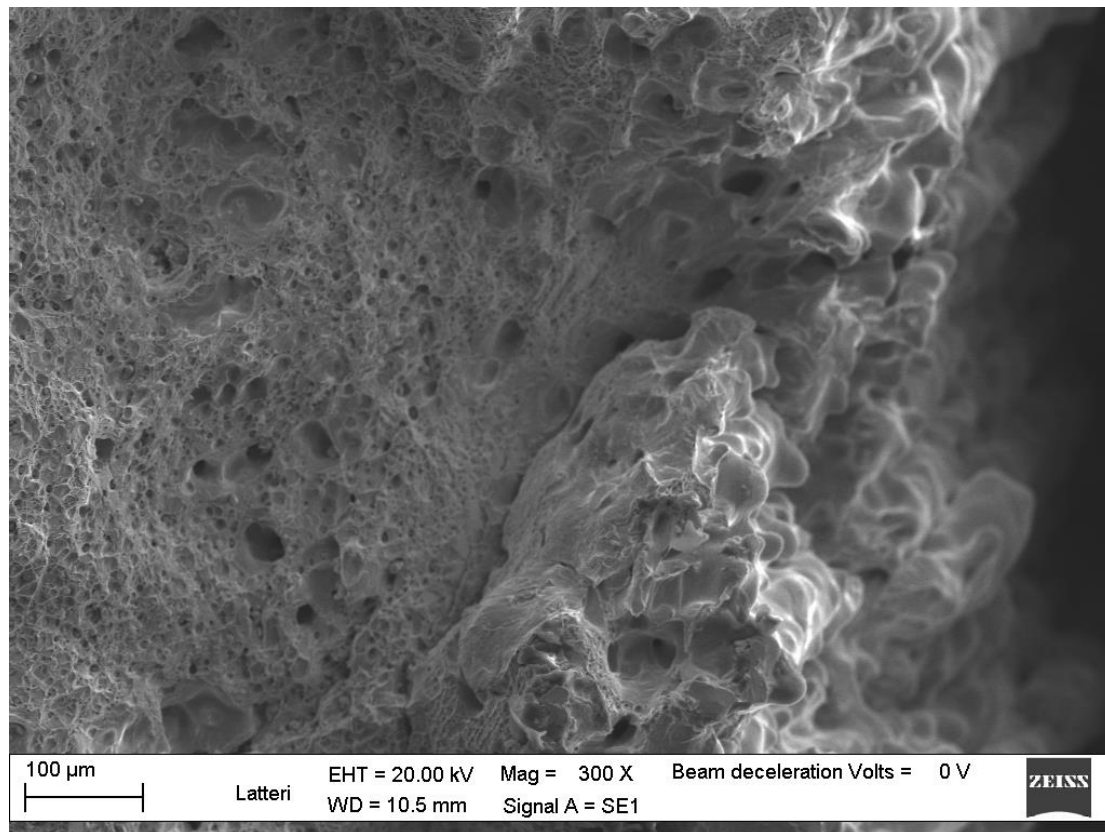
Figure 4.9 - SEM image of a 10s^{-1} strain rate tested sample's fracture zone (magnified 300×) showing crack propagating from the wall's raster.

The precedent images depict the tensile fracture surfaces of the tested samples under 1s^{-1} and 10s^{-1} strain rates. These fracture surfaces exhibit a combination of features, offering valuable insights into the fracture behaviour. Primarily, the fracture morphology showcases numerous dimples, underscoring the prevalence of ductile fracture mechanisms. These dimples are indicative of localized plastic deformation and serve as clear markers of the material's ability to absorb energy through plastic processes during failure. However, a closer look reveals more nuances in the fracture surfaces. In Figure 4.6, there are instances of smoother regions amidst dimple rich regions, hinting at variations in the local fracture behaviour, namely, indicating localized brittle behaviour despite the overall ductile fracture mode. There should be a discernible disparity in the fracture zone morphology achieved at varying strain rates; however, this is not evident in this case. Specifically, the dimples should exhibit a smoother appearance and should be fewer at lower strain rates [62]. It is likely that the difference in strain rates in the present work was insufficient to render this effect observable.

Notably, unlike other studies [32, 35], there's no visible regular porosity patterns and/or layer patterns in the mesostructure. This stems from the printing strategy used regarding the raster angle, which was set at random in each layer.

These observations also revealed the presence of two distinct types of defects: pores and inclusions. These defects were observed both within the raster structure and on its surface. The excessive porosity appears to be a consequence of incomplete fusion during the green state of the printing process, whereas the particle inclusions correspond most likely

to leftover polymeric binder. The incomplete fusion might be attributed to suboptimal processing conditions or insufficient bonding between the deposited layers.

In Figure 4.7, we can see a fracture path on the specimen's surface, becoming apparent that it originates at a larger pore and propagates towards the corner of a smaller neighbouring pore. We can also observe a crack starting in the valley of the outer wall raster and propagating inward towards the mesostructure in Figure 4.8 and Figure 4.9. There is also a significant concentration of the inclusions within the centre of many dimples. This spatial arrangement suggests that the material has been pulled and stretched around these inclusions during deformation, originating multiple micro stress concentrations in these regions and in some instances, resulting in smaller voids.

The presence of such defects is likely responsible for the slightly reduced mechanical properties observed in our samples when compared to the values reported in the technical data sheet provided by *BASF*. These defects, acting as stress concentration sites and can lead to decreased mechanical strength and overall performance of the printed parts. Further investigations into optimizing the printing parameters, such as adjusting the printing temperature, layer thickness or raster pattern, may help mitigate these defects and enhance the mechanical properties of the 3D-printed 17-4 PH samples. Additionally, evaluating the influence of post-processing treatments, like heat treatment or surface finishing, could offer potential solutions to improve the material's integrity and performance. Understanding and addressing these defects are crucial steps toward achieving high-quality and reliable 3D-printed components for industrial applications.

4.3. THERMAL CONDUCTIVITY AND DIFFUSIVITY

Once the values of density, specific heat, and thermal diffusivity are known, it is possible to calculate the values of thermal conductivity for the examined 17-4 PH stainless steel samples. Below are the experimentally calculated values of both thermal diffusivity and thermal conductivity at monotonically increasing temperature values from 25 °C to 200 °C in 25 °C intervals.
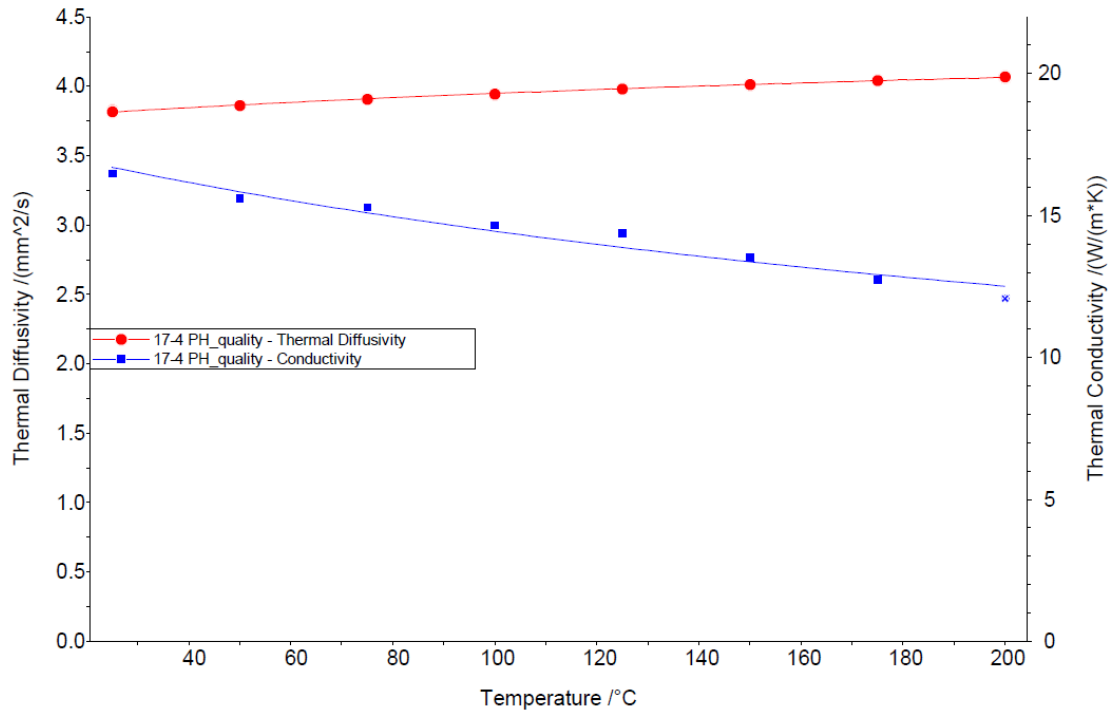
Figure 4.10 - Measured thermal conductivity and diffusivity. Each point in the graph corresponds to the average value of the measurements regarding the three thermal samples,

From the figure, a decrease in thermal conductivity with increasing temperature is immediately evident. The average thermal conductivity value obtained for 17-4PH steel is 14.9 W/mK, which is slightly lower than the average value reported in the literature for the same steel obtained through conventional processes, which is 18.1 W/mK, showing a percentage decrease of 18% [63, 64]. The decrease in thermal conductivity of the sintered and MFFF printed metallic samples with increasing temperature can be attributed to a combination of various factors. One of the main factors is the scattering of phonons, which are the primary heat carriers in metals. Phonon scattering occurs due to various mechanisms, such as lattice defects, grain boundaries, impurities, and phonon-phonon interactions. With increasing temperature, these scattering mechanisms become more evident, leading to a decrease in thermal conductivity.

In the case of sintered and MFFF printed metallic samples, the presence of porosity and voids can also contribute to the decrease in thermal conductivity with increasing temperature. These voids act as additional scattering sites for phonons, further hindering the heat transfer through the material. The presence of porosity is confirmed by lower density values compared to wrought steels (7.47 g/cm^3 compared to 7.80 g/cm^3 for 17-4PH) and by SEM micrographs obtained and analysed previously.

Furthermore, as the temperature increases, the atomic vibration amplitudes within the metal structure also increase. This increased atomic motion hinders the propagation of phonons and reduces their mean free path, leading to a decrease in thermal conductivity.

4.4. SHRINKAGE MEASUREMENTS

In the context of the flat samples, it is pertinent to acknowledge that establishing a differentiation between the X and Y dimensions would be redundant. This arises from the fact that both these dimensions of the squared samples are subjected to the same shrinkage phenomena, because both these axes are parallel to the planes that contain the printing layers. Furthermore, concerning this batch of samples, it is noteworthy that the printing and sintering axes coincide, as both the printing and sintering processes were carried out in the same position. The subsequent table presents the sample measurements in mm, along with the calculated shrinkage and OFS values for each respective direction:

Table 4.3 - Dimensions and shrinkage percentages of the flat set of samples.

Flat Samples (A)		
Printing Direction	X/Y	Z
Sintering Direction	X/Y	Z
Length	24.07 / 23.98	3.97
	24.01 / 24.13	4.11
	24.13 / 24.07	4.08
	23.99 / 24.02	3.98
	24.41 / 24.20	4.03
Avg. Length	24.10	4.03
Avg. Shrinkage	**15.61%**	**17.34%**
Avg. OFS	1.19	1.21

One of the primary discernible observations is the presence of a notable level of uncertainty concerning the dimensional precision and accuracy of the components along the dimensions parallel to the layer plane, namely, the X and Y axes. While some values exhibit proximity, others show dispersion, leading to an overall average length exceeding the intended nominal value (24 mm). In contrast, the thickness values for the samples, despite their variation, display significantly less dispersion, and their average is comparatively closer to the intended nominal value (4mm), albeit slightly higher.

This scenario signifies that the average shrinkage value for both dimensions is lower than the value indicated by *BASF*. This could be advantageous, as it may suggest that the green printed parts achieved satisfactory density, not having many gaps between raster lines. Additionally, this characteristic also enables the part to eventually undergo finishing procedures, effectively reducing its surface roughness and correcting its dimensions.

For the upright printed samples, where one of the 20 mm sides corresponds to the Z direction during printing, the scenario is different from the flat samples. For this set of samples, it became essential to discern between the X and Y sintering dimensions due to

distinct shrinkage patterns obtained. In this context, the side experiencing a relatively lower degree of shrinkage was designated as the X dimension, while the opposite edge, undergoing more pronounced shrinkage, was attributed the Y dimension. This distinction holds no significance in terms of the fundamental nature of the dimensions. Its purpose primarily revolves around facilitating practical reference.

The dimensions (measured in mm) of the upright printed samples are presented in Table 4.4. As previously noted, this group of samples underwent sintering while positioned flat, causing their thickness to correspond to their height during this process, such as the prior batch of samples. Consequently, the conversion of printing axes to sintering axes is also provided alongside the measurements. This shift in orientation means that the horizontal plane of the printing layers has transitioned to a vertical arrangement. This arrangement leads to variations in how the layers interact during the sintering process and, consequently, to anisotropy in the shrinkage of the different dimensions.

Table 4.4 - Dimensions and shrinkage percentages of the upright set of samples.

Upright Samples (B)			
Printing Direction	X	Z	Y
Sintering Direction	X	Y	Z
	20.80	19.14	4.57
	20.58	19.16	4.64
Length	20.47	19.11	4.59
	20.56	19.17	4.60
	20.39	19.06	4.54
Avg. Length	20.56	19.13	4.59
Avg. Shrinkage	**13.61%**	**19.63%**	**24.79%**
Avg. OFS	1.16	1.24	1.33

Upon analysing the preceding table, it becomes evident that the precision of values along the X direction is not optimal, considering the substantial amplitude exceeding 0.40 mm between the highest and lowest measurements. Interestingly, the shrinkage in this direction was notably lower than the expected 16%, resulting in larger dimensions for each sample's X edges compared to the Y ones.

In contrast, and diverging from the shrinkage trends observed in the first sample set, the average shrinkage along the Y direction was considerably high, causing all respective sample edges to be nearly 1 mm shorter than the intended 20 mm. Similar occurrences have previously been reported in the literature [32, 30]. This discrepancy suggests that there was a relatively higher compaction between layers and their adjacent counterparts during the sintering cycle, implying worse bonding between each layer during the printing phase compared to the flat printed samples and, consequently, implying formation of voids and less powder particles homogeneity, which in turn suggest that full density in the green specimens wasn't achieved. This mechanism in schematically shown in Figure 4.11.
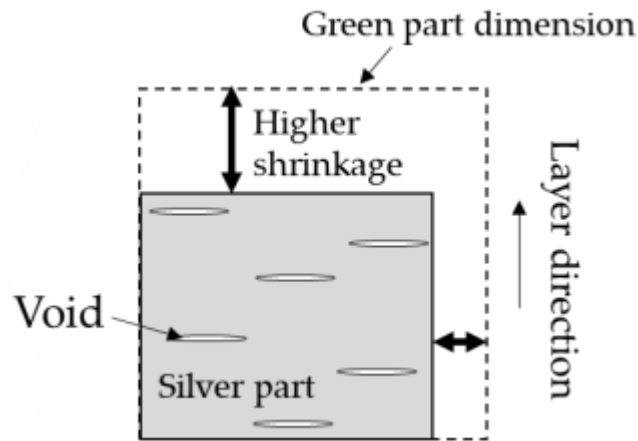
Figure 4.11 - Anisotropic shrinkage mechanism [30].

Although also valid for the flat samples, at first glance, this effect may not be noticeable due to the effect of gravity being a major contributor for the shrinkage in their thickness.

It is also of extreme importance to highlight that the cross section parallel to the layer plane of the upright samples is mostly comprised of wall lines, given that the wall line count is 3 and the wall raster thickness is also 0.6 mm, as represented in Figure 4.12.
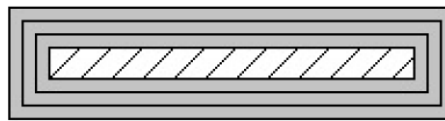
Figure 4.12 - Representation of upright sample's cross section with real wall proportions compared to the parts dimensions.

As seen in the previous image, the infill lines are not as prominent as the wall lines in this building configuration. Therefore, it is fair to assume that, in this case, the shrinkage is governed by the wall lines instead of the infill material, contrary to what happens in the previous set of samples.

These samples' thickness (Z sintering dimension) endured the most pronounced shrinkage among all the measured ones, at almost 25 %, which was higher than the one measured regarding the flat samples, even without suffering compaction between layers. Notably, the wall makes up 3.6 mm out of the 5 mm thickness and only occupies 3.6 mm of the 20 mm X length. Therefore, we can deduct that the random orientated infill lines convey better conditions for raster bonding, originating lower shrinkage and lower anisotropy, as we can see by the comparatively low shrinkage values obtained for the flat samples, that benefit of having a much higher infill printing in their cross-sectional area. In essence, the mechanism depicted in Figure 4.11 is also valid for wall lines interactions in the Z direction, except in this case the raster width is in a vertical position instead of the layer height. The fact that this type of infill is more proper for raster bonding is also confirmed by the fact that shrinkage in Y dimension of the upright samples was higher than the one in Z dimension of the flat samples.

Finally, in Z, as well as in Y, the measured length values were considerably closer to each other. While they were not accurate relatively to the intended nominal lenghts, the dimensional precision achieved was a favourable attribute.

4.5. CORROSION PERFORMANCE

Electrochemical evaluations, such as potentiodynamic polarization curves, are commonly utilized to evaluate the passivation potential and localized corrosion, particularly breakdown potential, of metals like stainless steels. However, interpreting polarization curve data can be challenging due to factors like the presence of oxides, defects, and porosities. These elements can cause the curves to deviate from the standard shape previously discussed. During the polarization process, current density and potential values were continuously monitored, forming the basis for constructing semilogarithmic polarization curves. The resulting curves for both A and B samples from this experimental study are presented in Figure 4.13 and Figure 4.14, respectively. Notably, unlike the previous graphs, in this instance, the potential is represented on the horizontal axis, while the logarithmic current is depicted on the vertical axis. Although the curve's appearance has shifted, the conveyed information remains the same. Our focus will primarily be on the anodic branch of the curve, as this is the more crucial segment for assessing corrosion performance. This is because electrochemically active metals experience corrosion during the oxidation process.
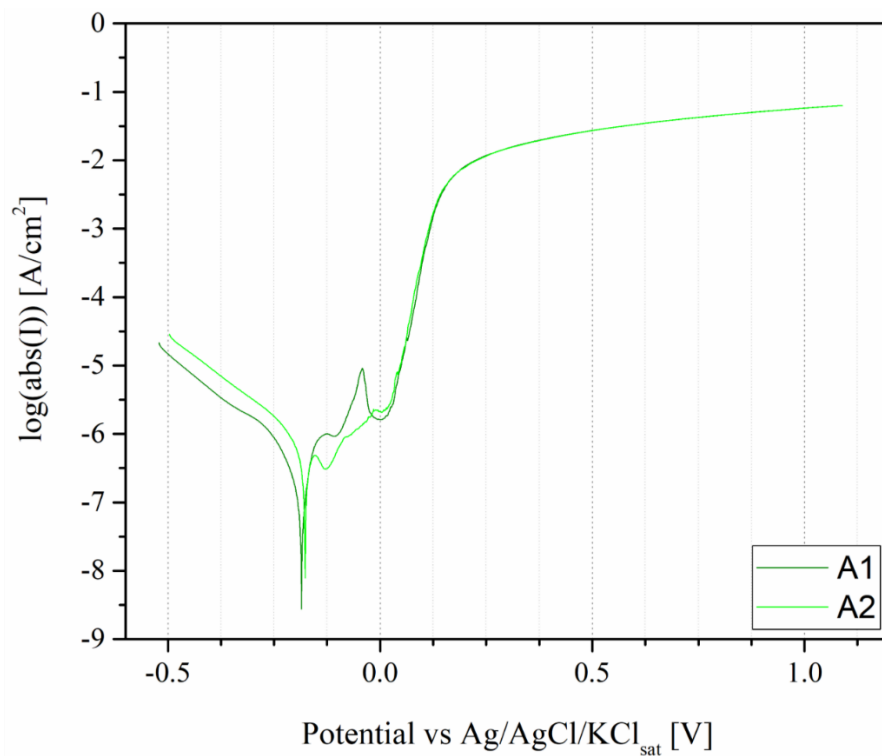
Figure 4.13 - Potentiodynamic polarization curves for two of the A samples.
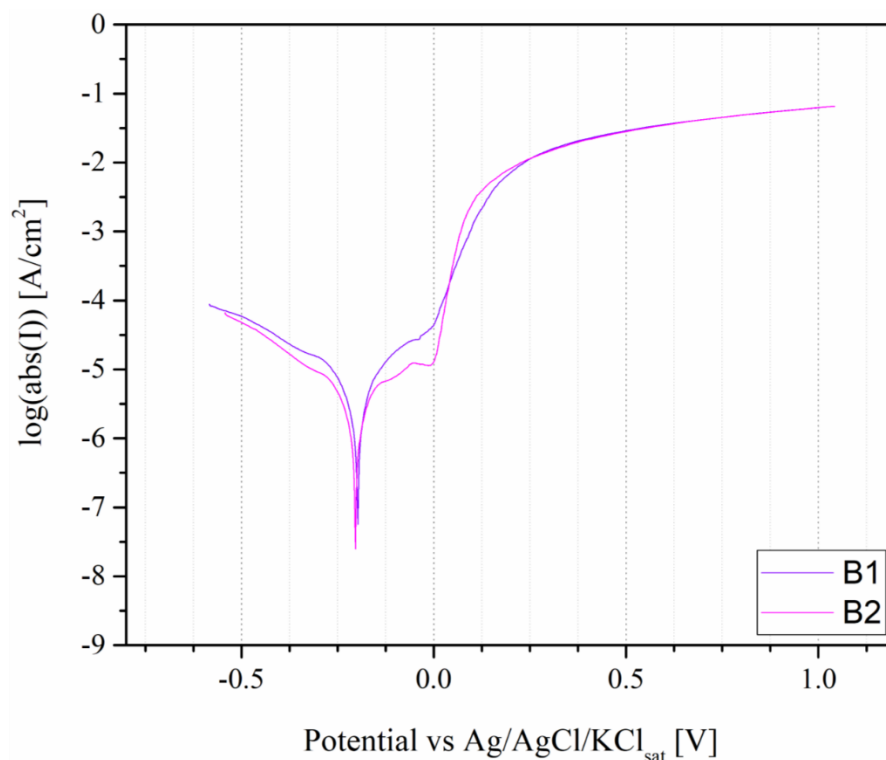
Figure 4.14 - Potentiodynamic polarization curves for two of the B samples.

By analysing the curves, the passive region within the anodic branch becomes discernible. This region lies between the active and transpassive regions, which correspond to sections where the curves exhibit steeper slopes (in terms of dec/mV in this case). As the applied potential is elevated, although there isn't a significant decline in current density after *Icrit*, there is a noticeable decrease in the rate at which it increases. This decrease is evident from the localized slopes on the curve. Within the passive region, there's a lack of observable meta-stable pitting, implying that, aside from one of the flat samples, the oxide films were adequately stable in the tested solution. The observed pit in sample A might have resulted from a defect in a specific location or locations on its surface. This initial disruption of the passive film led to pit formation. However, the potential wasn't sufficiently high to perpetuate pit growth and the corrosion process, allowing the film to self-repair. Further elevating the potential, all curves reach the breakdown potential, resulting in localized corrosion marked by the inflection point with a rapid rise in current density. It is around this juncture that pitting corrosion commences.

These curves yielded the extraction of corrosion potential (*Ecorr*), also referred to as the OCP, and the corresponding current density (*Icorr*). The latter was extrapolated through Tafel plotting, involving the utilization of linear portions from both the anodic and cathodic branches within the active region. The mean values of both sets of samples can be found in Table 4.5.

Table 4.5 - Corrosion potential and corrosion current density extrapolated by Tafel plotting. Inside the parenthesis, the half difference between the values of each type of samples is given.

Samples	Ecorr (mV)	Icorr (μA/cm^2)
A	-168 (51)	0,56 (0,036)
B	-223 (6)	5,90(2,7)

The breakdown potential, often referred to as the pitting potential, can also be estimated using the inflection point method [65]. This potential is characterized by the destabilization or formation of the passive layer and the subsequent spontaneous growth of corrosion pits. Below the pitting potential, the exposed surface primarily undergoes general corrosion with a comparatively lower and ideally predictable corrosion rate. However, when the electrochemical potential surpasses the pitting potential, localized pitting corrosion occurs with an unpredictable corrosion rate, resulting in rapid surface degradation. Upon analysing the polarization curves, it becomes evident that this potential is situated around the 0V mark for all samples, albeit slightly lower for the B samples. Both *Ecorr* and *Icorr* values indicate superior corrosion resistance for the flat samples, although the difference is not substantial. Similar findings were also documented in the previously mentioned BMD investigation [48]. Additionally, the current density along the curves of the flat samples is lower than that recorded for the upright samples. This accounts for the lower positioning of the flat samples' curves on the graph. With a corrosion current density value in hand, one can calculate the material's Corrosion Rate (cm/s) using Faraday's law of electrolysis, which articulates:

$$CR = \frac{I_{corr} \cdot M}{n \cdot F \cdot \rho}, \tag{11}$$

where *M* is the molar mass of the corroded elements (g/mol), *n* is the number of electrons of the corrosion reaction, *F* the Faraday's constant (C/mol) and ρ (g/cm^3) the density of the corroded elements. Usually, the surface area of the specimen would be included in the denominator and the *Icorr* would be presented in A and not A/cm^2, but since the submerged area was 1cm^2, the equation is already simplified. It is worth mentioning that 1A = 1C/s. The corrosion rate calculation was performed under the assumption that both *Fe* and *Ni* are responsible for the electrochemical reactions in place [65]. *M* and ρ were calculated, taking into account both species' relative weight in the metal's composition and the relative density of the samples. The weighted average molar mass obtained, *M*, was 55.98 g/mol and the density was 7.92 g/cm^3. Two electrons were exchanged ($Fe^0 \rightarrow Fe^{2+}, Ni^0 \rightarrow Ni^{2+}$) and *F* is equal to 96485 C/mol. After converting the computed values of corrosion rates from cm/s to μm/year, we obtained 6.47μm/year for the flat samples and 68.13 μm/year for the upright samples. The first figure shows that the first set of samples' surfaces are naturally passive, as expected, and could be used as reference for lifetime estimation of any part produced under the same conditions. The second figure, being more than ten times higher, implies that an upright building orientation isn't ideal for parts that need protection against corrosion.

The corrosion performance of a specific component is contingent on a multitude of factors, encompassing parameters like porosity, inclusions, surface roughness, grain size and shape, among others. Notably, surface pores are particularly susceptible to corrosion attacks, particularly pitting corrosion. Beyond significantly reducing the part's density, these pores can substantially contribute to both the initiation and propagation of corrosion pits. A relatively elevated surface roughness is inherent in most AM metal processes, hastening

the electrochemical interactions between the metal's surface and its surrounding environment. Given that both samples share identical printing parameters and are crafted from the same material, the disparity in corrosion resistance between the two can be attributed to the layer configuration of the upright samples. This aspect potentially leads to a rougher surface and a higher occurrence of surface defects, including pores, rendering them more prone to corrosion. Despite both specimen types sharing the same immersed surface area during testing, the overall corrosion rate, spanning both the active and passive regions, is higher in the upright samples. This could be due to the real surface area, which is greater, in microscopic terms, than the one from the flat samples, rendering the surface electrochemically more active and leading to a greater current flow per square centimetre of "macroscopic" surface. Additionally, the uneven nature of the surface on the upright printed samples yields a less uniform passive oxide layer, resulting in regions of reduced thickness. This vulnerability facilitates the breakdown of the passive layer by chloride ions and other electrochemically active species when the potential becomes considerably elevated. For applications where corrosion is a critical consideration, it is recommended to fabricate parts as close to a flat position as practically feasible.

Given that this study exclusively examines MFFF samples, a direct comparative analysis is absent. Nevertheless, a comparison can still be established by juxtaposing these outcomes with data found in existing literature, particularly those outlined in Table 2.5. Notably, a relevant basis for comparison exists with corrosion evaluation metrics associated with Laser Powder Bed Fusion (LPBF) and traditionally wrought specimens that underwent 1 hour of OCP stabilization [49]. These specimens offer suitable comparability due to the akin testing conditions, such as the identical salt concentration (0.6 M NaCl = 3.5 wt.% NaCl) in the immersion solution and the equivalent OCP stabilization duration. It is pertinent to acknowledge that certain other parameters, including temperature, solution pH, and the method employed for sample cleaning, may not align across these studies.

Upon scrutinizing the aforementioned values, a noticeable discrepancy surfaces: the MFFF samples exhibit inferior resistance to electrochemical corrosion in contrast to both wrought specimens and notably, those generated through LPBF. The substantially lower corrosion potential (*Ecorr*) implies a heightened susceptibility to spontaneous corrosion, while the elevated corrosion current density (*Icorr*) signifies an accelerated corrosion rate. This underscores that materials produced using the MFFF technique yield components with a relatively less robust passive layer, rendering them susceptible to localized corrosion. This susceptibility can be attributed once again to the inherent characteristics of the MFFF process and its discernible impact on the surface characteristics of the resultant parts.

5. CONCLUSIONS AND FUTURE RESEARCH DIRECTIONS

Within the scope of this thesis, MFFF 17-4 PH specimens were produced. Firstly, by printing metal/polymer composite green parts and then applying debinding and sintering processes to originate fully metallic silver parts. These samples were then subjected to mechanical and corrosion testing, as well as to shrinkage and thermal measurements.

All the specimens were fabricated using optimized printing parameters provided by *BASF*. One noteworthy aspect of these parameters was the inclusion of random raster angles for each printed layer. The samples designated for tensile testing in this study exhibited lower yield and tensile strength compared to parts produced by other AM methods but demonstrated similar tensile strength to those created through MIM. The primary contributing factor to this outcome is the porosity introduced during the sintering process, an integral shared characteristic of the MFFF and MIM processes. Most of the other AM technologies considered for comparison fall under the category of PBF processes, involving the melting of metal powders, which makes it possible to yield fully dense parts. Furthermore, the specimens in this study exhibited markedly low elasticity modulus and higher strain at failure when compared with other MFFF manufactured parts, indicative of heightened elasticity and ductility. SEM images predominantly revealed ductile behaviour, with cracks propagating from the visible pores and the wall raster. The tensile properties of our samples displayed a slight variance with an increase in strain rate during testing. Notably, the calculated strain rate sensitivity was relatively low. However, it is crucial to consider that this study employed only two strain rates, with a modest one-order-of-magnitude difference between them.

The flat-printed specimens designated for shrinkage and corrosion evaluation exhibited isotropic shrinkage within the XY plane, which was notably lower than the shrinkage observed in the layer direction (Z dimension). This outcome was in line with expectations and can be attributed to the influence of gravity during the sintering process. However, it is worth noting that both these values fell short of the initially predicted shrinkage levels. In contrast, the upright samples displayed highly anisotropic shrinkage, manifesting in all directions. Specifically, the Y sintering direction experienced a significantly greater degree of shrinkage compared to the X sintering direction. This marked difference can be primarily attributed to the varying nature of interlayer interactions versus intralayer interactions, as well as the specific orientation of the layer plane during the sintering process, which is vertical in this instance. Additionally, there is an influence stemming from the thickness of the walls.

The density achieved for the thermal samples was 95.24%. While only the thermal samples underwent density measurement, it is reasonable to assume that the density of all other samples, despite their varying geometries, should be comparable. Subsequently, the calculation of thermal conductivity utilized the recorded density values in conjunction with the measured thermal diffusivity values. The results indicated that the thermal conductivity fell below the reference value for 17-4 PH. This deviation was attributed to the presence of voids within the samples, confirmed by their incomplete density. These voids served as scattering sites for phonons, thereby influencing the overall thermal conductivity.

The evaluation of corrosion resistance was conducted on both flat and upright samples, revealing noteworthy differences. Notably, the flat oriented specimens exhibited superior corrosion resistance compared to their upright counterparts. Analysis of the

results revealed that the flat samples possessed more noble corrosion potential, indicating a higher potential for corrosion resistance. Furthermore, they exhibited lower corrosion current density. These variations in electrochemical behaviour were attributed to differences in surface morphology arising from the distinct building orientations of the samples. When compared to specimens manufactured using traditional methods and LPBF under similar test conditions, our samples displayed relatively lower corrosion resistance. This difference in performance between flat and upright samples can be attributed to the unique surface characteristics imparted by the MFFF process, characterized by high surface roughness and porosity, which significantly influences the corrosion dynamics.

In general, the specimens examined in this thesis did not meet the performance levels of other AM technologies, including previous MFFF studies. The optimization of our printing parameters, especially the layer height, holds the key to achieving denser parts, a critical factor for improved mechanical, thermal, and corrosion properties, as well as reduced shrinkage. It is noteworthy that settings such as the raster angle also significantly influence the tensile properties. Filament solid loading also is also an important factor that affects final part density. It is crucial to recognize that a balance between properties can be struck by fine-tuning the printing parameters. For example, parameters optimized for enhanced mechanical performance may result in a rougher surface, impacting corrosion resistance. Conversely, prioritizing surface quality often entails sacrificing some mechanical properties due to the choice of specific printing parameters.

5.1. FUTURE RESEARCH DIRECTIONS

As previously noted, a logical progression for this research involves conducting tensile tests at various strain rates to derive the parameters for the J-C model. This step is essential to assess the model's effectiveness in accurately predicting stress curves for MFFF 17-4 PH under different strain rates, including quasi-static testing for improved comparative reference against other studies. Furthermore, it is imperative to investigate the influence of different raster angle configurations on tensile behaviour. This will shed light on how these configurations impact the material's response and help identify the most favourable configuration for optimal results.

Exploring the correlation between sintering cycle parameters and corrosion resistance presents an intriguing avenue for further investigation. Given that the grain size of the final part is significantly influenced by sintering parameters like temperature and sintering time, a study examining the interplay between these factors, resulting density, and corrosion behaviour could yield valuable insights. Additionally, leveraging SEM as a tool for analysing corrosion, specifically to scrutinize pitting morphology and its evolution on corroded components, would have been highly advantageous in the current study.

MFFF demonstrates its promise as an affordable technology in the realm of additive manufacturing. Existing literature indicates the feasibility of producing parts with commendable tensile properties, on par with those achieved through well-established metal AM processes. However, comprehensive investigations encompassing the entire production cycle, spanning from filament manufacturing to post-printing processes, remain imperative. This is important for establishing a more efficient and quality focused approach to manufacturing parts tailored for specific load bearing applications.

Regarding corrosion performance, future studies should delve into the impact of porosity, inclusions and grain size. These explorations will provide deeper insights into how the MFFF process influences the corrosion behaviour of 17-4 PH, to better understand its potential for applications demanding robust corrosion resistance.

The findings from this research could serve as a base reference for future investigations, specially in the realm of corrosion and thermal properties, due to the lack of information found in the literature regarding these subjects.

6. REFERENCES

[1]   Thompson, Y., Gonzalez-Gutierrez, J., Kukla, C., & Felfer, P. (2019). Fused filament fabrication, debinding and sintering as a low cost additive manufacturing method of 316L stainless steel. *Additive Manufacturing, 30*, 100861.

[2]   Vyavahare, S., Teraiya, S., Panghal, D., & Kumar, S. (2020). Fused deposition modelling: a review. *Rapid Prototyping Journal*, *26(1)*, 176-201.

[3]   Wagner, M. A., Hadian, A., Sebastian, T., Clemens, F., Schweizer, T., Rodriguez-Arbaizar, M., Carreño-Morelli, E., & Spolenak, R. (2022). Fused filament fabrication of stainless steel structures-from binder development to sintered properties. *Additive Manufacturing, 49*, 102472.

[4]   Singh, G., Missiaen, J. M., Bouvard, D., & Chaix, J. M. (2021). Additive manufacturing of 17–4 PH steel using metal injection molding feedstock: Analysis of 3D extrusion printing, debinding and sintering. *Additive Manufacturing*, *47*, 102287.

[5]   Burkhardt, C., Freigassner, P., Weber, O., Imgrund, P., & Hampel, S. (2016). Fused filament fabrication (FFF) of 316L Green Parts for the MIM process. *World PM2016-AM-Deposition Technologies*.

[6]   Elkaseer, A., Schneider, S., & Scholz, S. G. (2020). Experiment-based process modeling and optimization for high-quality and resource-efficient FFF 3D printing. *Applied Sciences*, *10*(8), 2899.

[7]   Ramkumar, P. L., & Rijwani, T. (2022). Additive manufacturing of metals and ceramics using hybrid fused filament fabrication. *Journal of the Brazilian Society of Mechanical Sciences and Engineering*, *44*(10), 455.

[8]   Ramazani, H., & Kami, A. (2022). Metal FDM, a new extrusion-based additive manufacturing technology for manufacturing of metallic parts: a review. *Progress in Additive Manufacturing*, *7*(4), 609-626.

[9]   Lotfizarei, Z., Mostafapour, A., Barari, A., Jalili, A., & Patterson, A. E. (2022). Overview of debinding methods for parts manufactured using powder material extrusion. *Additive Manufacturing*, 103335.

[10]   Zhang, Y., & Roch, A. (2022). Fused filament fabrication and sintering of 17-4PH stainless steel. *Manufacturing Letters*, *33*, 29-32.

[11]   Recreus, "Extrusión directa vs. tipo bowden," [Online]. Available: https://recreus.com/es/noticias/aprende-con-recreus/extrusion-directa-vs-tipo-bowden (accessed on August 2023).

[12]   Dey, A., & Yodo, N. (2019). A systematic survey of FDM process parameter optimization and their influence on part characteristics. *Journal of Manufacturing and Materials Processing*, *3*(3), 64.

[13]   Caminero, M. Á., Romero Gutiérrez, A., Chacón, J. M., García-Plaza, E., & Núñez, P. J. (2022). Effects of fused filament fabrication parameters on the manufacturing of

316L stainless-steel components: geometric and mechanical properties. *Rapid Prototyping Journal*, *28*(10), 2004-2026.

[14] Tosto, C., Tirillò, J., Sarasini, F., Sergi, C., & Cicala, G. (2022). Fused deposition modeling parameter optimization for cost-effective metal Part Printing. *Polymers*, *14*(16), 3264.

[15] Godec, D., Cano, S., Holzer, C., & Gonzalez-Gutierrez, J. (2020). Optimization of the 3D printing parameters for tensile properties of specimens produced by fused filament fabrication of 17-4PH stainless steel. *Materials*, *13*(3), 774.

[16] Caminero, M. Á., Romero, A., Chacón, J. M., Núñez, P. J., García-Plaza, E., & Rodríguez, G. P. (2021). Additive manufacturing of 316L stainless-steel structures using fused filament fabrication technology: Mechanical and geometric properties. *Rapid Prototyping Journal*, *27*(3), 583-591.

[17] Jiang, D., & Ning, F. (2021). Additive manufacturing of 316L stainless steel by a printing-debinding-sintering method: Effects of microstructure on fatigue property. *Journal of Manufacturing Science and Engineering*, *143*(9), 091007.

[18] Liu, B., Wang, Y., Lin, Z., & Zhang, T. (2020). Creating metal parts by fused deposition modeling and sintering. *Materials Letters*, *263*, 127252.

[19] Quarto, M., Carminati, M., & D'Urso, G. (2021). Density and shrinkage evaluation of AISI 316L parts printed via FDM process. *Materials and Manufacturing Processes*, *36*(13), 1535-1543.

[20] BASF, Forward AM, "Ultrafuse Metal Filaments User Guidelines for 3D Printing Metal Parts," [Online]. Available: https://move.forward-am.com/hubfs/AES%20Documentation/Metal%20Filaments/Ultrafuse_metal_User_Guideline.pdf (accessed on July 2023).

[21] Park, D. Y., Lee, G. M., Kwon, Y. S., Oh, Y. J., Lee, S., Jeong, M. S., & Park, S. J. (2017). Investigation of powder size effects on sintering of powder injection moulded 17-4PH stainless steel. *Powder Metallurgy*, *60*(2), 139-148.

[22] Li, Y. M., Liu, X. Q., Luo, F. H., & Yue, J. L. (2007). Effects of surfactant on properties of MIM feedstock. *Transactions of Nonferrous Metals Society of China*, *17*(1), 1-8.

[23] Gonzalez-Gutierrez, J., Godec, D., Kukla, C., Schlauf, T., Burkhardt, C., & Holzer, C. (2017). Shaping, debinding and sintering of steel components via fused filament fabrication. In *16th international scientific conference on production engineering—computer integrated manufacturing and high speed machining. Zadar, Croatia*.

[24] Gonzalez-Gutierez, J., Godec, D., Guráň, R., Spörk, M., Kukla, C., & Holzer, C. (2018). 3D printing conditions determination for feedstock used in fused filament fabrication (FFF) of 17-4PH stainless steel parts. *Metalurgija*, *57*(1-2), 117-120.

[25] Kukla, C., Gonzalez-Gutierrez, J., Duretek, I., Schuschnigg, S., & Holzer, C. (2017, December). Effect of particle size on the properties of highly-filled polymers for fused filament fabrication. In *AIP Conference Proceedings* (Vol. 1914, No. 1). AIP Publishing.

[26] Abel, J., Scheithauer, U., Janics, T., Hampel, S., Cano, S., Müller-Köhn, A., Günther, A., Kukla, C., & Moritz, T. (2019). Fused Filament Fabrication (FFF) of Metal-Ceramic Components. *Journal of Visualized Experiments, 143*.

[27] Kukla, C., Cano, S., Kaylani, D., Schuschnigg, S., Holzer, C., & Gonzalez-Gutierrez, J. (2019). Debinding behaviour of feedstock for material extrusion additive manufacturing of zirconia. *Powder Metallurgy*, *62*(3), 196-204.

[28] Riecker, S., Clouse, J., Studnitzky, T., Andersen, O., & Kieback, B. (2016). Fused deposition modeling–opportunities for cheap metal AM. In *European Congress and Exhibition on Powder Metallurgy. European PM Conference Proceedings* (pp. 1-6). The European Powder Metallurgy Association.

[29] Kukla, C., Gonzalez-Gutierrez, J., Cano, S. C., Hampel, S., Burkhardt, C., Moritz, T., & Holzer, C. (2017, June). Fused filament fabrication (FFF) of PIM feedstocks. In *Congreso Iberoamericano de Pulvimetalurgia* (pp. 1-6). Comité Español de Pulvimetalurgia.

[30] Kurose, T., Abe, Y., Santos, M. V., Kanaya, Y., Ishigami, A., Tanaka, S., & Ito, H. (2020). Influence of the layer directions on the properties of 316l stainless steel parts fabricated through fused deposition of metals. *Materials*, *13*(11), 2493.

[31] Liu, B., Wang, Y., Lin, Z., & Zhang, T. (2020). Creating metal parts by fused deposition modeling and sintering. *Materials Letters*, *263*, 127252.

[32] Tosto, C., Tirillò, J., Sarasini, F., & Cicala, G. (2021). Hybrid metal/polymer filaments for fused filament fabrication (FFF) to print metal parts. *Applied Sciences*, *11*(4), 1444.

[33] Bjørheim, F., & Lopez, I. L. T. (2021, November). Tension testing of additively manufactured specimens of 17-4 PH processed by Bound Metal Deposition. In *IOP Conference Series: Materials Science and Engineering* (Vol. 1201, No. 1, p. 012037). IOP Publishing.

[34] Henry, T. C., Morales, M. A., Cole, D. P., Shumeyko, C. M., & Riddick, J. C. (2021). Mechanical behavior of 17-4 PH stainless steel processed by atomic diffusion additive manufacturing. *The International Journal of Advanced Manufacturing Technology*, *114*, 2103-2114.

[35] Suwanpreecha, C., Seensattayawong, P., Vadhanakovint, V., & Manonukul, A. (2021). Influence of specimen layout on 17-4PH (AISI 630) alloys fabricated by low-cost additive manufacturing. *Metallurgical and Materials Transactions A*, *52*, 1999-2009.

[36] BASF, Forward AM, "Comparison Sheet, Ultrafuse Metal Filaments Comparison," [Online]. Available: https://move.forward-am.com/hubfs/AES%20Documentation/Metal%20Filaments/Ultrafuse_onepager_comparison_metal_v1.0.pdf (accessed on July 2023).

[37] EOS, "EOS StainlessSteel 17-4 PH," 2022. [Online]. Available: https://www.eos.info/03_system-related-assets/material-related-contents/metal-materials-and-examples/metal-material-

datasheet/stainlesssteel/material_datasheet_industryline_17-4ph_m290_en_screen.pdf (accessed on July 2023).

[38] General E. Additive, "17-4 PH," [Online]. Available: https://www.ge.com/additive/sites/default/files/2019-11/17-4%20PH-M2beide.pdf (accessed on August 2023).

[39] Hu, Z., Zhu, H., Zhang, H., & Zeng, X. (2017). Experimental investigation on selective laser melting of 17-4PH stainless steel. *Optics & Laser Technology*, *87*, 17-25.

[40] Aripin, M. A., Sajuri, Z., Jamadon, N. H., Baghdadi, A. H., Syarif, J., Mohamed, I. F., & Aziz, A. M. (2022). Effects of Build Orientations on Microstructure Evolution, Porosity Formation, and Mechanical Performance of Selective Laser Melted 17-4 PH Stainless Steel. *Metals*, *12*(11), 1968.

[41] Luecke, W. E., & Slotwinski, J. A. (2014). Mechanical properties of austenitic stainless steel made by additive manufacturing. *Journal of research of the National Institute of Standards and Technology*, *119*, 398.

[42] Optimim, "MIM-17-4 PH (AS SINTERED)," [Online]. Available: https://www.optimim.com/en/metal-injection-molding-mim/material-options/stainless-steel/mim-17-4-ph-as-sintered (accessed on July 2023).

[43] Heaney, D. F., & Greene, C. D. (2019). Molding of components in metal injection molding (MIM). In *Handbook of Metal Injection Molding* (pp. 105-127). Woodhead Publishing.

[44] FineMIM, "MIM 17-4 PH," [Online]. Available: http://www.finemim.com/mim-17-4-ph (accessed on July 2023).

[45] Gibson, I., Rosen, D. W., Stucker, B., Khorasani, M., Rosen, D., Stucker, B., & Khorasani, M. (2021). *Additive manufacturing technologies* (Vol. 17, pp. 160-186). Cham, Switzerland: Springer.

[46] Gong, H., Snelling, D., Kardel, K., & Carrano, A. (2019). Comparison of stainless steel 316L parts made by FDM-and SLM-based additive manufacturing processes. *Jom*, *71*, 880-885.

[47] Tait, W. S. (2018). Electrochemical corrosion basics. In *Handbook of environmental degradation of materials* (pp. 97-115). William Andrew Publishing.

[48] Forcellese, P., Mancia, T., Simoncini, M., & Bellezze, T. (2022). Investigation on Corrosion Resistance Properties of 17-4 PH Bound Metal Deposition As-Sintered Specimens with Different Build-Up Orientations. *Metals*, *12*(4), 588.

[49] Schaller, R. F., Taylor, J. M., Rodelas, J., & Schindelholz, E. J. (2017). Corrosion properties of powder bed fusion additively manufactured 17-4 PH stainless steel. *Corrosion*, *73*(7), 796-807.

[50] Garcia-Cabezon, C., Castro-Sastre, M. A., Fernandez-Abia, A. I., Rodriguez-Mendez, M. L., & Martin-Pedrosa, F. (2022). Microstructure–hardness–corrosion performance of 17–4 precipitation hardening stainless steels processed by selective laser melting in

comparison with commercial alloy. *Metals and Materials International*, *28*(11), 2652-2667.

[51] BASF, Forward AM, "Technical Data Sheet, Ultrafuse 17-4 PH," [Online]. Available: https://info.sculpteo.com/hubfs/Material%20documentation/Ultrafuse%2017-4%20PH/201019_Ultrafuse_17-4PH_Technical_Data_Sheet_preliminary%20(1).pdf.

[52] Ultimaker, "Ultimaker," [Online]. Available: https://ultimaker.com/ (accessed on July 2023).

[53] BASF, Forward AM, "Ultrafuse 17-4 PH Process Instructions," [Online]. Available: https://forward-am.com/wp-content/uploads/2021/01/Process-Instructions-Ultrafuse-17-4-PH.pdf (accessed on July 2023).

[54] Martínez-Aparicio, B., Martínez-Bastidas, D., Gaona-Tiburcio, C., Martin, U., Cabral-Miramontes, J., & Almeraya-Calderón, F. (2023). Localized corrosion of 15–5 PH and 17–4 PH stainless steel in NaCl solution. *Journal of solid state electrochemistry*, 1-9.

[55] Akpanyung, K. V., & Loto, R. T. (2019, December). Pitting corrosion evaluation: a review. In *Journal of Physics: Conference Series* (Vol. 1378, No. 2, p. 022088). IOP Publishing.

[56] Nurhudan, A. I., Supriadi, S., Whulanza, Y., & Saragih, A. S. (2021). Additive manufacturing of metallic based on extrusion process: A review. *Journal of Manufacturing Processes*, *66*, 228-237.

[57] Gonzalez-Gutierrez, J., Arbeiter, F., Schlauf, T., Kukla, C., & Holzer, C. (2019). Tensile properties of sintered 17-4PH stainless steel fabricated by material extrusion additive manufacturing. *Materials Letters*, *248*, 165-168.

[58] Murugesan, M., & Jung, D. W. (2019). Johnson Cook material and failure model parameters estimation of AISI-1045 medium carbon steel for metal forming applications. *Materials*, *12*(4), 609.

[59] Lebrun, T., Tanigaki, K., Horikawa, K., & Kobayashi, H. (2014). Strain rate sensitivity and mechanical anisotropy of selective laser melted 17-4 PH stainless steel. *Mechanical Engineering Journal*, *1*(5), SMM0049-SMM0049.

[60] Sirigiri, V. K. R., Gudiga, V. Y., Gattu, U. S., Suneesh, G., & Buddaraju, K. M. (2022). A review on Johnson Cook material model. *Materials Today: Proceedings*, *62*, 3450-3456.

[61] Škrlec, A., & Klemenc, J. (2020). Estimating the strain-rate-dependent parameters of the Johnson-Cook material model using optimisation algorithms combined with a response surface. *Mathematics*, *8*(7), 1105.

[62] Wang, X., Liu, Y., Shi, T., & Wang, Y. (2020). Strain rate dependence of mechanical property in a selective laser melted 17–4 PH stainless steel with different states. *Materials Science and Engineering: A*, *792*, 139776.

[63] S. Metals, "DATA SHEET 17-4 PF / 1.4548," [Online]. Available: https://www.sd-metals.com/en/s-d-materials/special-stainless-steel/17-4ph-1-4548/ (accessed on September 2023).

[64] S. M. Steel, "Specification Sheet: Alloy 17-4PH," [Online]. Available: https://www.sandmeyersteel.com/images/17-4PH-Spec-Sheet.pdf (accessed on September 2023).

[65] Jansa, J., Volodarskaja, A., Hlinka, J., Zárybnická, L., Polzer, S., Kraus, M., Hajnyš, J., Schwarz, D., & Pagáč, M. (2023). Corrosion and material properties of 316L stainless steel produced by material extrusion technology. *Journal of Manufacturing Processes, 88*, 232–245.

Technical Data Sheet

Ultrafuse 17-4 PH

General information

Components

Polymer and 17-4 PH stainless steel composite filament

Product Description

Ultrafuse® 17-4 PH is a filament for the production of metal components in 17-4 stainless steel on standard Fused Filament Fabrication (FFF) printers. This stainless steel can be fully heat treated to high levels of strength and hardness. It is therefore ideal for Petrochemistry, Aerospace, the Automotive and the Medical Industry. Parts printed with our metal-polymer composite filament Ultrafuse® 17-4 PH obtain their final properties through a catalytic debinding and sintering process known from traditional Metal Injection Molding.

Typical applications are:
- Tooling
- Jigs and fixtures
- Series production
- Functional parts and prototypes

Delivery form

Ultrafuse 17-4 PH is delivered on 3KG spools. The two products have 1.75 mm and 2.85 mm diameters. The filament is available in both diameters.

Product safety

Recommended industrial hygiene procedures and the relevant industrial safety precautions for the handling of polymers must be followed whenever these products are being handled and processed. For additional information please consult the corresponding material safety data sheets.

For your information

Standards: DIN 1.4542, X 5 CrNiCuNb 17 4, AISI/UNS S17400 ; SAE J 467 (17-4PH)

Notice

The data contained in this publication are based on our current knowledge and experience. In view of the many factors that may affect processing and application of our product, these data do not relieve processors from carrying out their own investigations and tests; neither do these data imply any guarantee of certain properties, nor the suitability of the product for a specific purpose. Any descriptions, drawings, photographs, data, proportions, weights etc. given herein may change without prior information and do not constitute the agreed contractual quality of the product. It is the responsibility of the recipient of our products to ensure that any proprietary rights and existing laws and legislation are observed.

The safety data given in this publication is for information purposes only and does not constitute a legally binding Material Safety Data Sheet (MSDS). The relevant MSDS can be obtained upon request from your supplier or you may contact BASF 3D Printing Solutions GmbH directly at sales@basf-3dps.com.

BASF 3D Printing Solutions GmbH   sales@basf-3dps.com   www.forward-am.com

Recommended 3D-Print processing parameters

Nozzle Temperature	230 – 250 °C
Build Chamber Temperature	-
Bed Temperature	90 – 120 °C
Bed material	Glass + approved glues* / polyimide tape (*Magigoo® or Dimafix® suggested)
Nozzle Diameter	≥ 0.4 mm
Print Speed	15 – 50 mm/s

Filament Properties

Filament Diameter	1.75 mm	2.85 mm
Tolerance	±0.050 mm	±0.075 mm
Roundness	±0.050 mm	±0.075 mm
Bending Radius	5 ± 1 mm	10 ± 3 mm
Length per Spool	250 m	95 m
Weight per Spool	3 kg	3 kg

Drying Recommendations

Under normal conditions no drying is required.

General Properties

		Standard
Sintered Part Density	≥ 7.6 g/cm³ Density values obtained from tensile and fracture samples.	ISO 1183-1

Table listed below shows values
AS SINTERED:

	[1]Specimen shape Form E2x6x20 according to DIN 50125 [2]Undersized impact test specimen according to DIN EN ISO 148-1		
Print direction	Standard	XY	ZX
Orientation		Flat	Upright
Tensile strength	DIN EN ISO 6892-1[1]	760 MPa	730 MPa
Yield Strength, $R_{p\,0.2}$	DIN EN ISO 6892-1[1]	680 MPa	700 MPa
Elongation at Break	DIN EN ISO 6892-1[1]	4 %	3 %
Impact Strength Charpy (notched)	DIN EN ISO 148:2017-05[2] (2mm V-notch)	TBA	TBA
Vickers Hardness	DIN EN ISO 6507-1	257 HV 10	-